



**UNIVERSITÀ
DEGLI STUDI
DI BERGAMO**

UNIVERSITÀ DEGLI STUDI DI BERGAMO
SCHOOL OF ENGINEERING
DEPARTMENT OF ENGINEERING AND APPLIED SCIENCES
DOCTORAL PROGRAMME IN ENGINEERING AND APPLIED SCIENCES

Model Predictive Control Development for a Substation Suited to Fifth Generation District Heating Networks

Doctoral Dissertation of:
Mohammad Hossein Fouladfar

Supervisors:
Prof. Giuseppe Franchini
Dr. Roberto Fedrizzi

In cooperation with:

eurac
research

Abstract (EN):

District heating and cooling networks, forming the backbone of modern district energy systems, centralize the provision of thermal services for urban buildings. The evolution from traditional systems, which have been hampered by high heat loss rates and costs, to the advanced 4th and 5th Generation district heating and cooling networks (5GDHCNs) signifies a leap in efficiency. These 5GDHCNs have the unique ability to cater to both heating and cooling needs concurrently, especially vital for regions with variable climatic demands.

The deployment of 5th Generation systems, however, brings forth intricate challenges due to the combination of varied components, making the requirement for control strategies paramount, particularly as these systems increasingly interplay with non-dispatchable renewable energy sources and link with the larger electrical grid dynamics.

A pivotal component in this landscape is the substation, with a heightened focus on those serving residential buildings. These decentralized substations act as intermediaries: on one side, interfacing with the sophisticated 5GDHCNs, and on the other, tailoring the energy supply to meet the specific demands of residential buildings. Herein lies the significance of Model Predictive Control (MPC). With its innate ability to anticipate future scenarios, MPC equips the system to make informed, efficient decisions based on forecasted data.

In the realm of substations, the Thermal Energy Storage (TES) and Heat Pump (HP) play a vital role. The inclusion of a TES system in this setup elevates the operational flexibility. Armed with a TES, the controller is better poised to handle multifaceted tasks: from sector coupling, balancing the varying thermal needs, to efficiently orchestrating the charging and discharging cycles. Also, given that HPs are powered by electricity, their efficient operation is crucial from an economic perspective.

In this research, MPC is employed to optimize the flexible utilization of decentralized user substations within 5GDHCNs. The best operational strategies under diverse boundary conditions are assessed through MPC, considering factors such as district heating supply temperature variations and fluctuating grid electricity costs. The study showed that MPC outperformed RBC strategies under the operation conditions concerned, reducing electricity costs significantly across different pricing schemes and district heating management strategies, with notable electricity cost savings of up to 24%.

Abstract (IT):

Le reti di teleriscaldamento e teleraffrescamento, che costituiscono la spina dorsale dei moderni sistemi energetici di quartiere, centralizzano la fornitura di servizi termici per gli edifici urbani. L'evoluzione dai sistemi tradizionali, che sono stati ostacolati da alti tassi di perdita di calore e costi elevati, alle avanzate reti di teleriscaldamento e teleraffrescamento di quarta e quinta generazione (5GDHCNs) rappresenta un salto di qualità in termini di efficienza. Queste 5GDHCNs hanno la capacità unica di soddisfare contemporaneamente le esigenze di riscaldamento e raffrescamento, particolarmente vitale per le regioni con esigenze climatiche variabili.

L'implementazione dei sistemi di quinta generazione, tuttavia, porta con sé sfide complesse a causa della carattere distribuito della generazione di calore, fortemente incentrato sull'utilizzo di fonti energetiche non programmabili e sull'interazione con la rete elettrica, che rendono necessarie strategie di controllo. Un componente cruciale in questo contesto è la sottostazione di utenza, con un'attenzione particolare a quelle che servono edifici residenziali. Queste sottostazioni decentralizzate da un lato si interfacciano con le sofisticate 5GDHCNs e, dall'altro, adattano l'offerta energetica per soddisfare le specifiche esigenze degli edifici residenziali. Qui risiede l'importanza dei Controlli Predittivi basati su Modelli (MPC). Con la sua capacità innata di anticipare scenari futuri, l'MPC permette alla sottostazione di prendere decisioni informate ed efficaci, basate su dati previsti.

Nel campo delle sottostazioni, l'Accumulo di Energia Termica (TES) e la Pompa di Calore (HP) giocano un ruolo fondamentale. L'inclusione di un sistema TES in questa configurazione incrementa la flessibilità operativa. Dotato di un TES, il controllo può assolvere a funzioni di sector-coupling attraverso cicli di carica-scarica ottimizzati.

In questa ricerca, l'MPC viene impiegato per ottimizzare l'utilizzo flessibile delle sottostazioni decentralizzate in 5GDHCNs. Strategie di gestione ottimizzate sono valutate in diverse condizioni operative, considerando fattori come le variazioni della temperatura del teleriscaldamento e costi variabili dell'elettricità dalla rete. Lo studio dimostra come, sotto le condizioni considerate l'MPC ha superato le strategie convenzionali basate su regole, riducendo significativamente i costi operativi in diversi schemi tariffari e strategie di gestione del teleriscaldamento, con risparmi sui costi dell'elettricità utilizzata dalla sottostazione fino al 24%.

Acknowledgements

When I started my PhD journey, my niece was just three years old. She asked me, "Hey Uncle Pouya, what kind of doctor will you be?" She meant a medical doctor. I tried to explain in simple terms that I was an engineer and, after studying for another 3-4 years, I would become a doctor—though not an MD, but an engineer with advanced education. Her response, with the innocent yet blunt honesty of a child, was: "How meaningless! Fake doctor!" This sweet moment became a code in my family, symbolizing my hard work and the endearing title of "fake doctor." My mother and I often laughed about this incident.

I had always imagined the day I would defend my PhD, calling my mom to say, "Hey mom, believe it or not, I'm a doctor now!" Tragically, my mother passed away five months ago, and I never had the chance to share that moment with her. My parents were my constant support, and I owe everything to them. After my mother's passing, my father became an incredible pillar of strength, helping me complete my PhD journey.

I am immensely grateful to my brothers, sisters-in-law, and my wonderful uncles who were always there for me. A special thanks goes to my tutors, Dr. Roberto Fedrizzi and Prof. Giuseppe Franchini, for their invaluable guidance, encouragement, and advice. I have learned so much from you all.

Furthermore, I extend my gratitude to the Institute for Renewable Energy of EURAC Research for this opportunity that allowed me to grow during these years. Special thanks go to Dr. Maryam Fakhari and the team of the "Sustainable Heating and Cooling Systems" research group. Much of the experimental and simulation work would not have been completed without your assistance.

Thank you all for being part of this journey.

Table of Contents

1	INTRODUCTION	15
1.1	BACKGROUND.....	15
1.2	SIGNIFICANCE OF RESEARCH	16
1.3	RESEARCH QUESTIONS.....	18
1.4	METHODOLOGICAL APPROACH	20
1.5	ORGANIZATION OF THE THESIS	21
2	LITERATURE REVIEW.....	23
2.1	FROM THE FIRST TO THE FIFTH GENERATION OF DHNS.....	23
2.2	SUBSTATIONS IN 5GDHCNS.....	29
2.3	STATE OF THE ART CONTROL OF STRATEGIES IN DHNS	31
2.3.1	Basic Control Strategies in conventional DH/DC Systems	32
2.3.2	Basic Control Strategies in 4GDH and 5GDHC Systems.....	34
2.3.3	Advanced Control Strategies in DHC Networks	36
2.4	MODEL PREDICTIVE CONTROL	39
2.4.1	MPC in DHNs.....	44
2.5	MODEL IDENTIFICATION	47
3	METHODOLOGY	50
3.1	THERMAL LOAD PREDICTION.....	51
3.1.1	Case study	54
3.1.2	Input variable selection	55
3.1.3	ANN design and configuration	56
3.1.4	Technical barriers	58
3.1.5	Model enhancement	59
3.1.6	Continuous training model.....	60
3.1.7	Length of the dataset for training and validating	63
3.1.8	Learning through weight adjustments.....	64
3.1.9	Resetting state	65
3.1.10	Key performance indicators (KPIs)	66
3.1.11	Method assessment	66
3.1.12	Discussion	76
3.2	THERMAL ENERGY STORAGE MODEL	78
3.2.1	Mathematical model of thermocline TES	80
3.2.2	Methodology validation	91
3.3	HEAT PUMP	101
3.3.1	HP state machine model.....	103
3.4	OPTIMIZATION.....	107
3.4.1	Dynamic programming	109
3.5	INTEGRATION OF SUBSTATION.....	111
4	RESULTS AND DISCUSSION.....	119
4.1	SIMULATION CAMPAIGN FOR PERFORMANCE ANALYSIS OF THE DEVELOPED SUBSTATION.....	119

4.2	RBC vs. MPC.....	132
4.2.1	Concluding remarks	147
5	CONCLUSIONS AND RECOMMENDATION FOR FURTHER WORK	149
	REFERENCES	152
	APPENDIX 1	165
	APPENDIX 2	166

Table of figures

FIGURE 1-1. OVERVIEW OF THE SUBSTATION'S OPERATION WITHIN THE CONTEXT OF 5GDHCNs.	18
FIGURE 2-1. EVOLUTION OF DISTRICT HEATING	26
FIGURE 2-2. FLEXYNETS RESIDENTIAL SUBSTATION	29
FIGURE 2-3. DETAILS OF THE "PROSUMER" SUBSTATIONS ADOPTED IN SOME OF THE SURVEYED 5GDHC SYSTEMS	30
FIGURE 2-4. BASIC CONTROL STRATEGIES IN CONVENTIONAL DISTRICT HEATING (DH) SYSTEMS	32
FIGURE 2-5. (A) PIPING & INSTRUMENTATION DIAGRAM OF THE MIXING STATION INSTALLED AT THE DH SYSTEM OF BRESCIA; (B) SHUNT SYSTEM INSTALLED IN THE DISTRICT HEATING AND COOLING (DHC) SYSTEM OF ALBERTSLUND	35
FIGURE 2-6. MPC STRATEGY. THE VERTICAL BLACK ARROW MARKS THE PRESENT TIME. BLACK LINE PAST COMMANDS. RED LINE FUTURE COMMANDS.....	41
FIGURE 2-7. BASIC DESIGN OF MPC.....	42
FIGURE 3-1. THE LAYOUT OF THE BUILDING IN THE CASE STUDY.....	55
FIGURE 3-2. CORRELATION HEATMAP SHOWING THE RELATIONSHIP BETWEEN INPUTS AND THERMAL LOAD.....	56
FIGURE 3-3. STRUCTURE OF PROPOSED ANN MODEL FOR LOAD PREDICTION.....	58
FIGURE 3-4. IDENTIFIED MODEL FOR LOAD (AND ZONE TEMPERATURE) PREDICTION.....	59
FIGURE 3-5. GRAPHICAL REPRESENTATION OF THE CONSTRUCTION OF THE EXTENDED STATE $\Xi(T)$ CARRIED OUT BY THE VDL BLOCK.....	61
FIGURE 3-6. ILLUSTRATION OF THE VECTOR REPRESENTATION IN THE CASE OF THE DELAY BLOCK.....	61
FIGURE 3-7. GRAPHICAL REPRESENTATION OF A FUNCTIONAL BLOCK (FB) IMPLEMENTED BY THE NEURAL NETWORK.....	63
FIGURE 3-8. THE STRUCTURE OF THE PROPOSED IDEA REGARDING WEIGHTS IN ANN	65
FIGURE 3-9. LIVING ROOM'S TEMPERATURE AND THERMAL LOAD PREDICTION FOR THE FIRST WEEK OF DECEMBER	67
FIGURE 3-10. RMSE (A) AND MBE (B) FOR TEMPERATURE IN THE WINTER.....	68
FIGURE 3-11. RMSE (A) AND MSE (B) OF THERMAL LOAD IN THE WINTER	69
FIGURE 3-12. NMBE FOR THERMAL LOAD	70
FIGURE 3-13. LIVING ROOM'S TEMPERATURE AND THERMAL LOAD PREDICTION FOR THE FIRST WEEK OF JULY	70
FIGURE 3-14. RMSE (A) AND MBE (B) FOR TEMPERATURE IN THE SUMMER	71
FIGURE 3-15. RMSE (A) AND MBE (B) FOR THERMAL LOAD IN THE SUMMER	72
FIGURE 3-16. NMBE FOR THERMAL LOAD	73
FIGURE 3-17. LIVING ROOM TEMPERATURE AND THERMAL LOAD PREDICTION FOR THE FIRST WEEK OF DECEMBER. WEIGHT INITIALIZATION: GLOROT UNIFORM	74
FIGURE 3-18. RMSE OF THERMAL LOAD (A) AND TEMPERATURE (B). WEIGHT INITIALIZATION: GLOROT UNIFORM	75
FIGURE 3-19. SIMPLIFIED DIAGRAM OF TES.....	79
FIGURE 3-20. STRATIFICATION OF THE PROPOSED MODEL.....	81
FIGURE 3-21. DISTRIBUTION TEMPERATURE IN THE TANK.....	81
FIGURE 3-22. STRATIFICATION OF THE PROPOSED MODEL WITH MORE DETAILS	81
FIGURE 3-23. THERMOCLINE FORMATION IN CHARGE MODE	84
FIGURE 3-24. MOVEMENT OF THERMOCLINE IN CHARGING MODE	86
FIGURE 3-25. CONTRACTION STAGE IN CHARGING MODE	88
FIGURE 3-26. THERMOCLINE FORMATION IN DISCHARGE MODE	89
FIGURE 3-27. MOVEMENT OF THERMOCLINE IN DISCHARGE MODE.....	90
FIGURE 3-28. CONTRACTION STAGE IN DISCHARGE MODE.....	90
FIGURE 3-29. TES SETUP WITHIN THE LABORATORY.....	92
FIGURE 3-30. (A) TANK'S CONFIGURATION DERIVED FROM THE MANUFACTURER'S DATASHEET, (B) TANK'S CONFIGURATION UNDER THE ASSUMPTION OF A PERFECT CYLINDER.	93
FIGURE 3-31. STAGES IN OUR PROPOSED MODEL (BASED ON THE RESULT OF "TEST-1")	95
FIGURE 3-32. CHARGE TEST. (A) HEIGHT CHANGES IN EACH LAYER (B) MASS CHANGES IN EACH LAYER IN ENTIRE PROCESS OF CHARGING	95
FIGURE 3-33. CHARGE TEST. (A) TEMPERATURE IN THE TOP AND BOTTOM LAYER, (B) MONITORED AND SIMULATED TEMPERATURE OF WATER ALONG THE TANK	95
FIGURE 3-34. CHARGE TEST. (A) POWER GIVES TO THE TANK, (B) THE ABSOLUTE DIFFERENCE BETWEEN OBSERVED AND MODELED DATA.	96

FIGURE 3-35. CHARGE TEST. (A) SPEED OF THERMOCLINE, (B) WIDTH OF THERMOCLINE, (C) HEIGHT CHANGES AND (D) MASS BALANCE	96
FIGURE 3-36. CHARGE TEST. (A) TEMPERATURE IN THE TOP AND BOTTOM LAYER, (B) MONITORED AND SIMULATED TEMPERATURE OF WATER ALONG THE TANK	97
FIGURE 3-37. CHARGE TEST. (A) POWER GIVEN TO THE TANK, (B) THE ABSOLUTE DIFFERENCE BETWEEN OBSERVED AND MODELED DATA.	97
FIGURE 3-38. DISCHARGE TEST. (A) SPEED OF THERMOCLINE, (B) WIDTH OF THERMOCLINE, (C) HEIGHT CHANGES AND (D) MASS BALANCE	98
FIGURE 3-39. DISCHARGE TEST. (A) TEMPERATURE IN THE TOP AND BOTTOM LAYER, (B) MONITORED AND SIMULATED TEMPERATURE OF WATER ALONG THE TANK	98
FIGURE 3-40. DISCHARGE TEST. (A) POWER GIVEN TO THE TANK, (B) THE ABSOLUTE DIFFERENCE BETWEEN OBSERVED AND MODELED DATA.	99
FIGURE 3-41. DISCHARGE TEST. (A) SPEED OF THERMOCLINE, (B) WIDTH OF THERMOCLINE, (C) HEIGHT CHANGES AND (D) MASS BALANCE	99
FIGURE 3-42. DISCHARGE TEST. (A) TEMPERATURE IN THE TOP AND BOTTOM LAYER, (B) MONITORED AND SIMULATED TEMPERATURE OF WATER ALONG THE TANK	99
FIGURE 3-43. DISCHARGE TEST. (A) POWER GIVEN TO THE TANK, (B) THE ABSOLUTE DIFFERENCE BETWEEN OBSERVED AND MODELED DATA.	100
FIGURE 3-44. STATE MACHINE OF HP	103
FIGURE 3-45. SCHEMATIC DIAGRAM OF SCHEME 1	112
FIGURE 3-46. SCHEMATIC DIAGRAM OF SCHEME 2.....	112
FIGURE 3-47. SCHEMATIC DIAGRAM OF SCHEME 3.....	113
FIGURE 3-48. SCHEMATIC DIAGRAM OF SCHEME 4.....	113
FIGURE 3-49. POSITION OF SENSOR ACTIVATION AND DEACTIVATION WITHIN THE TANK	114
FIGURE 3-50. EXAMPLE OF THE PERFORMANCE OF HYSTERESIS HA.....	114
FIGURE 4-1. TEMPERATURE RANGES FOR TOP OF THE TANK AND USER-SIDE TEMPERATURE STABILITY ACROSS VARIOUS COMBINATIONS OF (SETPOINT, TANK SIZE AND DH TEMPERATURE). OUTLIERS REMOVED.	122
FIGURE 4-2. PERFORMANCE OF HP MINUTELY, OPERATIONAL SCHEMES, ELECTRICITY CONSUMPTION, AND ON/OFF CYCLES FOR ONE WEEK.....	124
FIGURE 4-3. THE “DISTRIBUTION OF HP OPERATION” BY THE HOUR OF THE DAY FOR VARIOUS COMBINATIONS.....	126
FIGURE 4-4. A COMPREHENSIVE ANALYSIS OF THE HP SYSTEM’S PERFORMANCE BY DISPLAYING BOTH THE COP _{sys} AND THE HP _{on} MINUTELY CATEGORIZED BY SCHEME STATE.	128
FIGURE 4-5. CHARGING AND DISCHARGING PROCESSES FOR DIFFERENT TANK SIZES (1 M ³ , 2 M ³ , AND 3 M ³) UNDER VARIOUS SETPOINT AND DH TEMPERATURE CONDITIONS	130
FIGURE 4-6. RESULT OF COMPARISON THE PERFORMANCE OF MPC VS. RBC WITH CONSTANT ELECTRICITY PRICE (TEST 1).....	134
FIGURE 4-7. ACTIVATION TIME OF THE HP IN TEST 1.....	134
FIGURE 4-8. RESULT OF COMPARISON THE PERFORMANCE OF MPC VS. RBC WITH TOU (TEST 2)	134
FIGURE 4-9. ACTIVATION TIME OF THE HP IN TEST 2.....	135
FIGURE 4-10. ELECTRICITY PRICE IN TEST 3	136
FIGURE 4-11. RESULT OF COMPARISON THE PERFORMANCE OF MPC VS. RBC WITH VARIABLE ELECTRICITY PRICE (TEST 3).....	136
FIGURE 4-12. ACTIVATION TIME OF THE HP IN TEST 3	136
FIGURE 4-13. HP OPERATION DISTRIBUTION BY HOUR WITH ELECTRICITY PRICES AND AVERAGE OF THERMAL LOAD (TEST 3)	137
FIGURE 4-14. RESULT OF COMPARISON THE PERFORMANCE OF MPC VS. RBC WITH CONSTANT ELECTRICITY PRICE AND DH TEMPERATURE FOLLOWING LOAD PROFILE (TEST 4)	139
FIGURE 4-15. ACTIVATION TIME OF THE HP IN TEST 4	139
FIGURE 4-16. RESULT OF COMPARISON OF MPC AND RBC WITH CONSTANT ELECTRICITY PRICE AND INVERSE RELATIONSHIP BETWEEN DH TEMPERATURE AND LOAD (TEST 5)	140
FIGURE 4-17. ACTIVATION TIME OF THE HP IN TEST 5	141

FIGURE 4-18. RESULT OF COMPARISON OF MPC AND RBC WITH CONSTANT ELECTRICITY PRICE AND HIGHER DH TEMPERATURE (TEST 6).....	142
FIGURE 4-19. ACTIVATION TIME OF THE HP IN TEST 6	142
FIGURE 4-20. COMPARISON OF MPC AND RBC WITH CONSTANT ELECTRICITY PRICES AND REALISTIC DH TEMPERATURES (TEST 7).....	144
FIGURE 4-21. ACTIVATION TIME OF THE HP IN TEST 7	144
FIGURE 4-22. HP OPERATION DISTRIBUTION BY HOUR WITH ELECTRICITY PRICES, AVERAGE OF THERMAL LOAD AND DH TEMPERATURE (TEST 7).....	145
FIGURE 4-23. EVALUATION OF MPC AND RBC PERFORMANCE WITH REALISTIC ELECTRICITY PRICING AND DH TEMPERATURES (TEST 8).....	146
FIGURE 4-24. ACTIVATION TIME OF THE HP IN TEST 8	146
FIGURE 4-25. HP OPERATION DISTRIBUTION BY HOUR WITH ELECTRICITY PRICES AND AVERAGE OF THERMAL LOAD (TEST 8)	146

List of tables

TABLE 3-1. TIME OF TRAINING FOR WINTER AND SUMMER [MINUTES].....	73
TABLE 3-2. COMPARISON OF TRAINING TIME FOR PROPOSED AND GU INITIALIZATION METHODS FOR WINTER [MINUTES]	76
TABLE 3-3. VERTICAL POSITIONS WITHIN THE TANK UNDER THE ASSUMPTION OF A PERFECT CYLINDER (REFERENCED FROM THE BASE OF THE TANK)	93
TABLE 3-4. CHARACTERISTICS OF THE HOT WATER STORAGE TANK.	94
TABLE 3-5. CONDITIONS FOR HP ACTIVATION AND DEACTIVATION BASED ON HA HYSTERESIS.....	115
TABLE 3-6. CONDITION FOR ACTIVATION AND DEACTIVATION OF HMA	115
TABLE 3-7. CONDITION FOR ACTIVATION AND DEACTIVATION OF HMB	115
TABLE 3-8. CONDITION FOR ACTIVATION AND DEACTIVATION OF HMC	116
TABLE 3-9. CONDITION FOR ACTIVATION AND DEACTIVATION OF HMD	116
TABLE 3-10. CONDITIONS FOR TRANSITION BETWEEN DIFFERENT SCHEMES.....	116
TABLE 3-11. MASS FLOW RATE IN THE SUBSTATION AND DH [M ³ /H].....	117
TABLE 4-1. PARAMETERS AND VALUES CONSIDERED IN THE SIMULATION CAMPAIGN	120
TABLE 4-2. ECONOMIC ASSESSMENT OF TEST 1, 2 AND 3	137
TABLE 4-3. A COMPREHENSIVE OVERVIEW OF VARIOUS PERFORMANCE METRICS FOR TEST 1, 2 AND 3.....	138
TABLE 4-4. ECONOMIC ASSESSMENT OF TEST 4	140
TABLE 4-5. A COMPREHENSIVE OVERVIEW OF VARIOUS PERFORMANCE METRICS FOR TEST 4.....	140
TABLE 4-6. ECONOMIC ASSESSMENT OF TEST 5	141
TABLE 4-7. A COMPREHENSIVE OVERVIEW OF VARIOUS PERFORMANCE METRICS FOR TEST 5.....	141
TABLE 4-8. ECONOMIC ASSESSMENT OF TEST 6	143
TABLE 4-9. A COMPREHENSIVE OVERVIEW OF VARIOUS PERFORMANCE METRICS FOR TEST 6.....	143
TABLE 4-10. ECONOMIC ASSESSMENT OF TEST 7	145
TABLE 4-11. A COMPREHENSIVE OVERVIEW OF VARIOUS PERFORMANCE METRICS FOR TEST 7.....	145
TABLE 4-12. ECONOMIC ASSESSMENT OF TEST 8	147
TABLE 4-13. A COMPREHENSIVE OVERVIEW OF VARIOUS PERFORMANCE METRICS FOR TEST 8.....	147
TABLE 0-1: COMPREHENSIVE LIST OF HYSTERESIS MECHANISM CASES FOR SCHEMES' TRANSITION.....	166

Abbreviations

ANN	Artificial Neural Network
ARX	Autoregressive Exogenous
CHP	Combined Heat and Power
COP	Coefficient of Performance
CS	Control Signal
CSV	Comma-Separated Values
CKPI	Computed Key Performance Indicator
DC	District Cooling
DH	District Heating
DHCNs	District Heating and Cooling Networks
DP	Dynamic Programming
DR	Demand Response
DHW	Domestic Hot Water
4GDHC	4th Generation District Heating and Cooling
5GDHCNs	5th Generation District Heating and Cooling Networks
GA	Genetic Algorithm
GU	Glorot Uniform
HEX	Heat Exchanger
HP	Heat Pump
HVAC	Heating, Ventilating, and Air Conditioning
KPIs	Key Performance Indicators
LP	Linear Programming
LSTM	Long Short-Term Memory
MAS	Multi-Agent System
MBE	Mean Bias Error
MILP	Mixed-Integer Linear Programming
MINLP	Mixed-Integer Non-Linear Program
ML	Machine Learning
MLP	Multilayer Perceptron
MPC	Model Predictive Control
MP	Mean Period
MSE	Mean Square Error
NMBE	Normalized Mean Bias Error
NLTV	Nonlinear and Time-Varying
PID	Proportional-Integral-Derivative
PCC	Pearson's Correlation Coefficient
PSO	Particle Swarm Optimization
PV	Photovoltaic
ReLU	Rectified Linear Unit
RBC	Rule-Based Control
RMSE	Root Mean Square Error
RPM	Revolutions Per Minute
ROM	Reduced-Order Model
RNN	Recurrent Neural Network

Abbreviations

SDH	Solar District Heating
SH/ SC	Space Heating/ Cooling
SOC	State of Charge
STC	Solar Thermal Collectors
SVM	Support Vector Machines
SWOT	Strengths, Weaknesses, Opportunities, and Threats
TES	Thermal Energy Storage
TOU	Time of Use
VDL	Vector Delay Lines
WSHP	Water-Source Heat Pumps
WWHP	Water-to-Water Heat Pump
XGBoost	Extreme Gradient Boosting

Nomenclature

T	Temperature [°C]
t / k	Time step
D	Day
q_x	Number of past samples of the state variables
q_u	Number of past samples of the input variables
\hat{y}	Predicted value
\bar{y}	Average of actual values
\mathbf{y}	Output vector
\mathbf{u}	Input vector
\mathbf{x}	State vector
r	Reference signal vector
n	Vector size of the state
p	Vector size of the output
m	Vector size of the input
w	Width of thermocline [cm]
C_p	Specific heat [J/kg·K]
v	Volume [m^3]
ρ	Density [$\frac{kg}{m^3}$]
h	Height [cm]
H	Total height [cm]
A	Area [m^2]
\dot{m}	Mass flow rate [kg/s]
N	Number of samples/ prediction horizon
C	Cost
Q	Heat energy

Greek symbols

φ	Global horizontal irradiation [kJ/h/m ²]
ξ	Extended state vector
θ	Internal gain [W]
μ	Mean value
σ	Standard deviation
δ	Float number [0, 1]
Δt	Change or difference in time [s]
Δx	Change or difference in distance [cm]
Δh	Change or difference in height [cm]
ϵ	Temperature margin [°C]
ω	Normalized revolutions per minute (%)
τ	Time duration [t]

Subscripts

in/out	Inlet/ Outlet
c/ d	Charge/ Discharge
min/max	Minimum/ Maximum
top/ bot	Top/ Bottom
ex/ m	Expansion/ Movement
ON/ OFF	Turned on/ Turned off
th	thermal
el	Electrical
disc	Discomfort
ret	Return
lw/ up	Lower/ Upper

Chapter 1

1 Introduction

The operation of buildings is linked to approximately 36% of the global energy consumption, 40% of greenhouse gas emissions, and climate change [1]. According to Eurostat's latest data, in 2021, households comprised 27% of total energy consumption in the EU. Most of this energy (64.4%) was used for heating homes, with renewables making up 27% of EU household heating [2]. The European Union is taking steps to reduce its dependence on fossil fuels and protect its energy supply. To achieve this, the EU has set ambitious targets for reducing greenhouse gas emissions. In 2018, the EU strengthened the Emissions Trading System (ETS) to deliver on the 40% emission reduction target by 2030. However, the EU is now considering increasing this target to 50% or 55% by 2030, as part of its efforts to reach climate neutrality by 2050 [3].

The primary approaches to addressing these challenges involve optimizing energy utilization and utilizing local energy resources. These strategies are accompanied by energy conservation policies. However, adopting these methods requires the establishment of sophisticated energy networks, integrating non-programmable renewable sources, and embracing circular economy principles within the energy sector.

The implementation of District Heating and Cooling Networks (DHCNs) has been recognized as a promising approach to decrease both primary energy usage and local emissions, effectively meeting the heating and cooling needs of buildings [4].

1.1 Background

District energy systems, commonly referred to as district heating and cooling networks, are centralized infrastructures that provide heating and cooling to numerous buildings or facilities within a given area or district. These networks operate on the premise that thermal energy may be produced and dispersed from a single point to satisfy the heating and cooling requirements of multiple buildings, including residential, commercial, and industrial ones [5].

Conventional district heating (DH) systems work by heating urban areas with hot water or steam delivered through pipes from centralized power plants. However, high-temperature DH systems

have high heat loss rates and high installation costs, particularly in the summer when many systems are used only to supply domestic hot water, which results in thermal losses of about 30% of the energy supplied owing to water retention. Research is currently concentrated on 4th and 5th Generation district heating and cooling networks (5GDHCNs), which run at low temperatures for greater efficiency, to address these challenges. In 4GDH systems, the same pipes cannot simultaneously offer heating and cooling services to different buildings. This is where the advantage of 5GDHC technology comes in. It holds significant potential, particularly in places with a Mediterranean climate. In such areas, buildings require both heating and cooling, making it possible for a 5GDHC operator to sell both services all year round by utilizing the same thermal network [6].

The advent of 5th Generation DH systems, with their numerous advantages, including the ability to supply water to decentralized Water-Source Heat Pumps (WSHP) within a wide temperature range and harnessing abundant local heat sources, represents a promising development in the field of district heating and cooling. However, the complexity of these advanced systems is significantly heightened, particularly with the integration of diverse components such as heat pumps (HP) and thermal energy storage (TES) within customer-sited substations. As a result, more sophisticated control strategies are required due to the growing complexity of smart district heating and cooling grids, which is fueled by the integration of non-programmable renewable thermal energy sources and coupling with the power grid. To successfully address these difficulties, conventional approaches by themselves are insufficient. Smart control strategies, both at the centralized and decentralized levels, are therefore essential and ought to be used in addition to the fundamental control strategies. With the goal of enhancing system performance and accommodating capacity restrictions within the district heating network, these cutting-edge strategies aim to address problems including weather inconsistencies, user behavior, and customer-sited substation operations.

1.2 Significance of research

In searching for sustainable energy solutions, research on 5GDHCNs is extremely important. 5GDHCNs present a viable way to reduce energy usage in buildings, encourage the adoption of renewable energy sources and lessen greenhouse gas emissions as global energy demands rise and environmental concerns grow. These cutting-edge networks can enhance energy systems, effectively harvesting excess thermal energy for increased overall efficiency, by permitting

optimal sector coupling between thermal and electrical grids. Additionally, 5GDHCNs offer a novel approach to maximize urban space in the context of growing urbanization since they enable centralized thermal energy storage and delivery, avoiding the space restrictions that limit individual ground heat exchanger installations. This development in district heating and cooling systems encourages competitiveness as well.

In 5GDHC networks, substations play a crucial role in the energy distribution process. Their main function is to facilitate the exchange of thermal energy between the central energy source and the individual buildings or consumers within the network. The substations serve as intermediaries that adjust the temperature of the energy coming from the central source to match the specific requirements of each building for space heating or cooling. Decentralized substations, also known as customer-sited energy transfer stations or heat substations, are a specific type of substation located closer to end-users, typically within or nearby individual buildings. Unlike centralized substations that serve larger areas, decentralized substations are smaller and serve specific buildings or groups of buildings in proximity. The implementation of decentralized substations offers several advantages within DHC networks. Firstly, it enables a more efficient and targeted distribution of thermal energy, delivering it directly to the buildings where it is needed, thereby reducing transmission losses. Secondly, it grants greater flexibility and control to individual consumers, as each building can have its own substation that adjusts the thermal energy supply according to its unique requirements, allowing for customized heating and cooling solutions that optimize energy consumption and minimize waste. The utilization of decentralized substations in DHC networks aligns well with the significance of employing advanced controllers to optimize system performance. These controllers, especially Model Predictive Control (MPC), play a crucial role in managing the operation of decentralized substations and ensuring the fulfillment of objectives in 5GDHCNs. With decentralized substations in place, MPC becomes a powerful tool in realizing the advantages. Its predictive capabilities enable real-time optimization of thermal energy distribution, responding to changing demands and supply conditions. By considering factors like weather forecasts, demand, and energy prices, MPC dynamically adjusts the operation of individual substations, precisely delivering the required amount of thermal energy when and where it is needed. This dynamic optimization capability of MPC enhances the overall efficiency and targeted distribution of thermal energy within 5GDHCNs, reducing transmission losses and waste, thus contributing to more sustainable and energy-efficient heating and cooling solutions.

1.3 Research Questions

Figure 1-1 illustrates the core concept of the project, showing the operation of the substation. This study primarily focuses on controlling substations within 5GDHCNs. It explores how a high-level controller, based on MPC, can optimally manage decentralized substations in the 5GDHC network. The emphasis is on effectively utilizing a TES system to flexibly meet building loads.

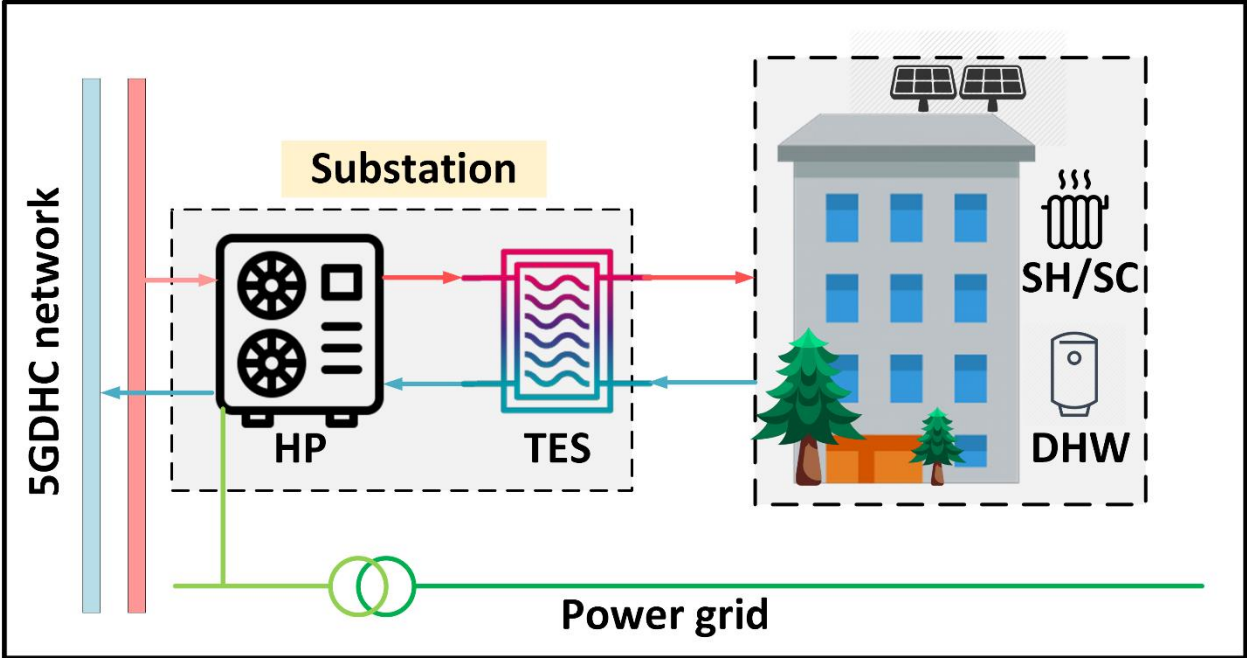


Figure 1-1. Overview of the substation's operation within the context of 5GDHCNs.

As mentioned above, the implementation of MPC for a residential decentralized substation connected to a 5GDHN is the focus of this research. Within this context, the management of the HP and the TES charging will be handled by MPC to optimize the overall operation and performance of the substation. The study will thoroughly analyze the potential benefits and challenges of using MPC as an optimal control strategy for decentralized substations, considering factors such as efficiency, flexibility, and adaptability to varying energy supply conditions.

The integration of MPC necessitates the development of several models. First, a predictive model for the building's thermal requirements is essential, as MPC relies on accurate forecasts future thermal demand and effectively manage the substation. Additionally, MPC must assess the state of charge of the TES and the operational status of the HP, taking into account how the mutual interaction influences the system performance. Consequently, detailed models for both the HP and TES are required to accurately replicate their real behavior. Additionally, an optimization

component is crucial to determine the optimal operation pathway along a specific time horizon in the future.

To address these requirements, this study investigated several sub-questions as follows:

RQ1) How can a flexible reduced-order model (ROM) be created to accurately forecast thermal load in residential buildings? For minimizing energy consumption, boosting energy efficiency, and implementing efficient demand-side management strategies, accurate thermal load forecast in dwellings is essential. Developing a ROM that accurately reflects the fundamental dynamics of thermal load fluctuations while ensuring computational simplicity is one of the primary aims of this research. The model must be powerful and flexible in its application, fitting buildings of all sizes and shapes, while allowing to be trained during operation, with a limited amount of monitoring data available, and be run online, eventually on hardware with limited computational capacity.

RQ2) How can a ROM be developed for TES that is simple enough as to be continuously trained during operation to retain accuracy, not only in terms of energy stored but also in terms of temperature distribution? The accurate modeling of TES is essential for optimizing energy efficiency and ensuring reliable energy supply. This research aims to tackle the complexity of TES modeling by formulating a mathematical model that fulfills three critical objectives: 1) a simplified model that captures the fundamental dynamics of TES behavior while reducing computational complexity, 2) that maintains a consistent energy balance, accounting for all relevant energy inputs and outputs during charging and discharging processes, and 3) that ensures a consistent description of the temperature distribution along the TES height, as this influences the performance and triggers the operation of the connected HP.

RQ3) How can a real-time optimization in a receding horizon fashion be effectively implemented for the integrated operation of a substation including HP and TES that seamlessly considers dynamic interactions with the electricity grid, thermal grid, and buildings? The integration of these components poses unique challenges, requiring a comprehensive approach to ensure optimal and synchronized operation. The research aims to advance control techniques to enable real-time decision-making for the integrated system. The receding horizon approach, also known as MPC, has been explored as a key framework to continuously optimize the system's operation based on real-time data acquired and changing operating conditions.

1.4 Methodological approach

To tackle the mentioned research questions, the following methods have been employed:

- **RQ1)** Historical data plays a crucial role to develop a ROM for accurate thermal load prediction [7]. Therefore, a detailed simulation of a real building was conducted using TRNSYS, a powerful and versatile simulation software for energy systems. Through this simulation process, valuable insight into the building's thermal behavior was gathered, capturing its dynamic response to varying weather conditions and other dynamic boundary conditions. Artificial Neural Network (ANN) is a cutting-edge solution for the development of a ROM that predicts thermal load accurately. The versatility of ANN allowed us to effectively handle the multidimensional relationships between the input parameters and the thermal load and indoor temperature variations. We determined the optimal ANN structure specifically tailored for the ROM. This entails designing the input layer to accommodate relevant boundary conditions, determining the number of hidden layers and neurons to capture complex patterns without overfitting, and configuring the output layer to represent thermal loads and indoor temperature predictions. The model's performance was analyzed based on key indicators, comparing it to simulated data.
- **RQ2)** To address the challenges of modeling a thermocline thermal energy storage system, a simple “piston” model was developed, and upgraded to account for thermoclines born, evolution along the TES height and collapse. Monitoring data from laboratory tests at EURAC’s Energy Exchange Lab was used, which included charging and discharging cycles under a range of operating conditions. The model's results were compared with the monitored data using key performance indicators, assessing uncertainty and consistency across variable operating conditions.
- **RQ3)** A full MPC execution compound has been implemented allowing to simulate a building + heating system and to use this as a basis for the calculation of optimized management pathways over the receding time horizon. Particularly, the two above models elaborated as part of this work have been coupled with a HP model (available already at EURAC) to simulate the DH substation when serving a residential building. An optimization algorithm based on the Dynamic Programming (DP) approach (also already available at EURAC) have been integrated with the simulation model, receiving performance information from the latter and providing optimized set point values for the

charge of the TES, over said receding horizon. The performance of the MPC have been thoroughly analyzed, considering various operation scenarios to assess its capabilities and effectiveness.

1.5 Organization of the thesis

Chapter 1 introduces the foundation of the research, beginning with a background that sets the scene for the research problem at hand. It then allocates the significance of the research, elaborating on the importance and implications of the study in the wider context. The chapter also enumerates the research questions, providing readers with a clear insight into the objectives being pursued. An overview of the methodology gives a snapshot of the research design and approach adopted.

Chapter 2 investigates deep into the literature, tracking the evolution of DHNS from its first to the fifth generation. It then focuses on substations in 5GDHNS and discusses the current state of control strategies in DHNS. A deeper investigation into the basic control strategies in both conventional DH/DC Systems and in 4GDH and 5GDHC Systems is presented. The chapter also elaborates on the advanced control strategies in DHC Networks. It further investigates the realm of MPC, its applications in DHNs, and concludes with a section on model identification.

Chapter 3 outlines the methodology employed in this research. It commences with a detailed examination of thermal load prediction, exploring its details, including feature selection, structure of neural networks, KPIs, and more. The chapter then transitions into TES models, providing a deep dive into the mathematical modeling of thermocline TES and its dynamic stages. It also presents methodology validation with various case studies, results, and discussions. Following this, the chapter delves into the heat pump, exploring the HP state machine model. It includes a detailed exploration of optimization, highlighting dynamic programming and its mathematical framework. The chapter rounds off by integrating a substation with various configurations for connecting DH to HP and TES.

Chapter 4 analyzes the entire system by running the substation under various conditions to establish a rule-based control (RBC) strategy. Subsequently, the performance of the MPC-based controller is evaluated by running MPC under different conditions and comparing its performance against the RBC. The resulting implications and outcomes are presented and discussed in detail.

Chapter 5 concludes the thesis by summarizing key findings and revisiting the initial research questions. It also recommends next steps and highlights the research's impact in the field.

Chapter 2

2 Literature review

This chapter described the evolution of district heating and cooling technology. The historical roots and development trajectory of this technology has been investigated. During this investigation, the critical significance of control tactics in influencing advancements in this essential subject have been disclosed.

2.1 From the first to the fifth generation of DHNs

For many years, buildings were heated by burning different types of fuel, starting with wood, and progressing to charcoal, coal, coke, oil, and natural gas. Initially, most fuel was burned in open fires and stoves. Later, in the 20th century, it became common to burn fuel to heat water or produce steam, which was then circulated through buildings to provide central heating via radiators.

The first generation of district heating, introduced in the late 1870s in the United States, utilized steam as the heat carrier. Until around 1930, these systems were common in both the United States and Europe [5]. Steam pipes in concrete ducts, steam traps, and compensators were all often used components. Nonetheless, due to the limitations of high steam temperatures resulting in significant heat losses and the possible hazards of steam explosions causing accidents and even fatalities, this technique has become outdated. While some cities, such as Salzburg, Hamburg, and Munich, have successfully implemented replacement programs, others, such as New York (Manhattan) and Paris, continue to use steam. The primary reason for establishing these systems was to replace individual apartment boilers to improve safety and comfort. Authorities, on the other hand, experienced difficulties in coordinating rival supply in the same locations [8]. The second generation of district heating emerged in the 1930s and dominated new systems until the 1970s. It used pressurized hot water as the heat carrier, with temperatures typically above 100°C. These systems included water pipes in concrete ducts, large heat exchangers, and heavy valves. Soviet-based district heating systems also used this technology, but they lacked heat demand control and had lower quality. Outside the Union of Soviet Socialist Republics (USSR), the quality was better, and some water-based district heating systems still use this technology. Different countries had

slightly varied motivations, but the focus was on achieving fuel savings and improving comfort through combined heat and power (CHP) utilization. The third generation of systems emerged in the 1970s and expanded significantly in the 1980s and beyond. It uses pressurized water as the heat carrier, with temperatures below 100°C. This generation, known as "Scandinavian district heating technology," features prefabricated pipes buried underground, compact substations with stainless steel heat exchangers, and efficient components. It has been widely adopted in various regions, including Central and Eastern Europe, the former USSR, China, Korea, Europe, the USA, and Canada. The motivation for using this technology includes ensuring a stable supply, energy efficiency through CHP, and replacing oil with more affordable and locally available fuels like coal, biomass, and waste. Some places also use solar and geothermal heat as supplements [9].

The notion of 4th Generation District heating and cooling (4GDHC) was first used by Prof. Sven Werner and afterwards given a formal and enhanced definition in a paper from 2014 [8]. According to the paper, the 4GDH system is a well-defined and comprehensive technological and institutional concept. It revolves around the utilization of smart thermal grids to promote the development of sustainable energy systems. 4GDH systems are specifically designed to provide heat supply to low-energy buildings with minimal grid losses, achieved through the integration of low-temperature heat sources with smart energy systems. This concept involves the establishment of an institutional and organizational framework to facilitate cost-effectiveness and motivation structures that support the implementation and success of 4GDH. The idea behind 4GDH is to create a low-temperature network, supplying heat between 70÷35°C, that can efficiently meet the demand for space heating and domestic hot water. This is achieved primarily through centralized systems for heat production and storage.

The main differences of 4GDH compared to previous generations are lower supply temperatures, the integration of low-temperature excess heat, and the incorporation of large shares of renewable heat sources. The implementation of 4GDH presents both technical and non-technical challenges. On the technical side, these challenges encompass adopting lower supply temperatures, integrating large-scale renewable energy sources, and incorporating storage technologies. Non-technical challenges include addressing consumer acceptance, developing new business models for district heating, and establishing suitable regulatory frameworks. To conduct a comprehensive assessment of the 4GDHs, an analysis of their strengths, weaknesses, opportunities, and threats (SWOT) was performed in [10]. This analysis examines the SWOT associated with the implementation and

operation of these innovative heating systems. The assessment reveals several areas of strength in their favor, according to the SWOT analysis. They can connect to various sectors like electricity or transport, and they are a driving force for future district heating improvements. They can also use a lot of renewable energy sources to reduce carbon emissions. However, there are also some weaknesses. They might not be cost-efficient in the short and medium term, and it can be tricky to adapt them to crowded areas. On the bright side, 4GDHNs offer opportunities to create value in specific countries by using renewable energy sources and being suitable for new buildings with low heat needs. Expanding efficient district heating networks also aligns with energy strategies, leading to more growth prospects. But there are threats too. If heat demand decreases significantly, there could be more heat losses. They also face competition from attractive low-temperature heating options like heat pumps. Existing heat supply contracts might make it hard to reduce temperatures without involving consumers [11].

The increasing adoption of heat pumps (HPs) in heating and cooling systems has been a significant driver in the development and implementation of 5th Generation District Heating and Cooling (5GDHC) Networks. 5GDHC networks are heating and cooling systems that use water or brine as a carrier. These networks operate at temperatures close to the ground and are not used directly for heating. However, this low temperature lets them use excess heat from industries and cities, along with renewable heat sources. The customer substations can reverse their operation, providing both heating and cooling to various buildings using the same pipelines. With hybrid substations, 5GDHC technology connects thermal, electrical, and gas grids in a smart and decentralized energy system [6].

5GDHCNs have several good points, including the ability to recover low-temperature excess heat and use renewable energy sources efficiently. They can provide both heating and cooling services throughout the year and are flexible in adapting to changing conditions. The networks have low heat losses and can use the ground as thermal storage. However, they also have some weaknesses, such as expensive substations and the need for domestic hot water (DHW) tank. The expenses related to heat pumps and their electricity usage may be a matter of concern.

Despite challenges, there are exciting opportunities. 5GDHCNs can create new business models and convert existing networks. They can work well with seasonal storage and help in achieving decarbonization goals. Moreover, they allow energy savings through district-level strategies and better interaction with the electric sector. On the other hand, there are potential threats. The design

approach of conventional district heating systems may need adjustments. The efficiency of HPs could vary depending on the building's heating system and network temperature. Space limitations might become an issue if dependent on seasonal storage.

5GDHC systems are known for their flexibility, and this is achieved by integrating thermal energy storage at both the network level and the user substation level. This allows the shift in time between producing and using thermal energy to be managed effectively [12]. Another important point to note is their compatibility with Seasonal Thermal Energy Storage. Borehole and Aquifer Thermal Energy Storage are well-suited for 5GDHC technology, as they can store heat at low temperatures in the ground and in underground water sources, optimizing their performance [13]. The 5GDHC system is specially designed to connect with the electrical grid and use excess heat from nearby sources [14].

As Figure 2-1 shows, DHNs have seen a significant increase in the share of renewable resources. In the past decades, renewable energy sources like solar and wind have shown significant progress in electricity generation, but renewable thermal energy generation has not experienced the same level of advancement. Even if the technology is mature, only a few countries such as Denmark, Sweden and Lithuania [15] already achieved a good share of renewable thermal energy production in DH/DC systems thanks to their ambitious decarbonization policies.

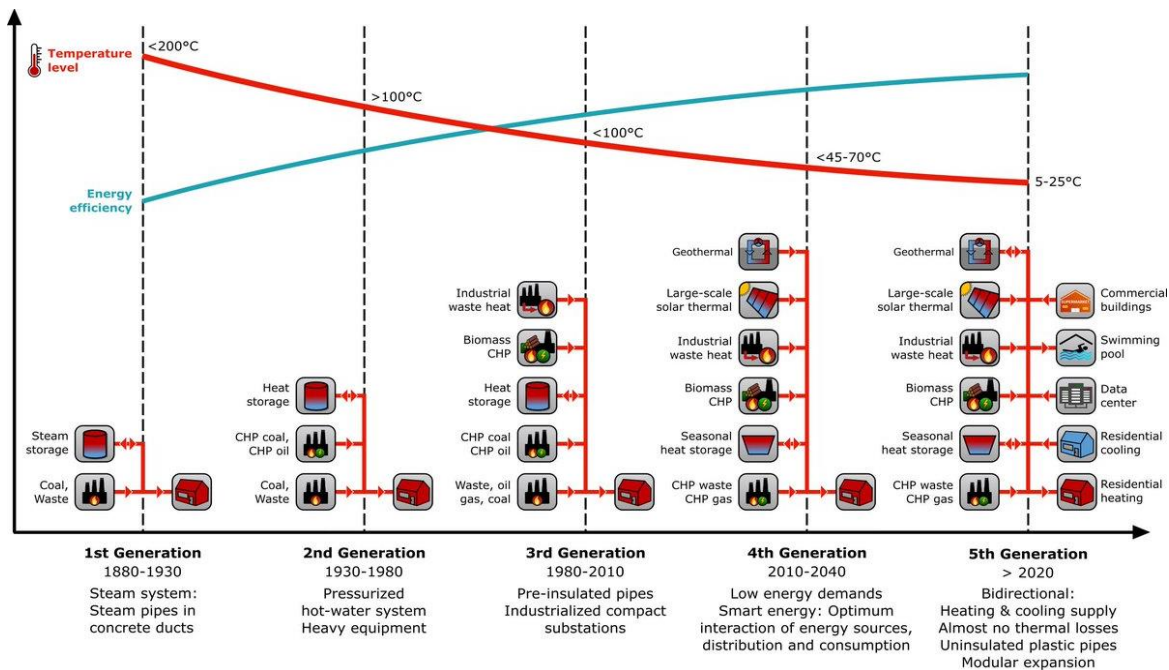


Figure 2-1. Evolution of district heating [8]

DHC plays a crucial role in expanding renewable thermal energy in buildings. It combines two important aspects: using economies of scale and finding solutions to building-level challenges, like limited space and preserving architectural heritage. In Europe, DH cover about 12% of the heating market share [14] and DC only 2% of the cooling market share [15]. Worldwide, district energy systems supply only 6% of the thermal energy demand and it is strongly based on fossil fuels. In fact, in 2018 only 8% of the energy sources employed in DHC were based on renewables with 95% of this consisting of biomass according to [15]. This high share confirms that biomass is the most competitive source for renewable heat supply in DHC systems of several countries. Moreover, it is easy to implement since the management of the heat generation plant remains very similar to a conventional dispatchable fossil-based one. Biomass boilers can be derived from the upgrade of existent coal-fueled plants and, in some cases, are coupled with steam-based or Organic Rankine Cycles (ORC) combined heat and power (CHP) systems [18].

The years between 2020 and 2030 have been defined as the “Geothermal Decade” [19], since a large growth is foreseen for the exploitation of geothermal energy in Europe for both electricity production and direct/indirect use. Even if the location of high enthalpy geothermal reservoirs is geographically constrained, medium enthalpy resources are more diffused. Deep geothermal for direct use in DH can meet the heating demand of about 25% of the European population according to the results of the research project GeoDH [20]. With this regard, Iceland is the leader country in the installed capacity of geothermal DH. The projections for coming years foresee important market growth of geothermal DH, especially in France, Germany, Denmark, the Netherlands and Hungary [19]. Deep geothermal for direct use in DH provide dispatchable baseload capacity, achieving large equivalent full-load hours. Shallow geothermal can be exploited almost everywhere but requires centralized or decentralized heat pumps to lift the supply temperature.

Solar thermal has great potential for DH application, but conversely from geothermal and biomass might introduce more effort for the control of the system that can be supported by forecast tools for both the heat demand and the not-programmable solar heat generation. Denmark is the pioneer country in solar district heating (SDH) and the worldwide leader in large-scale solar thermal fields achieving 1.1 GWth of installed capacity in the first half of 2019 (almost equal to the PV capacity installed in the country) [21]. This was possible thanks to the competitive heat price from solar thermal with respect to gas (affected by high taxes), high penetration and sound experience with DH networks, cheap land prices and willingness of the community-owner DH companies that run

a business that is non-profit by law. From the Danish experience [22], the average efficiency of the solar collector fields is about 40%, and the heat production cost ranges from 20 to 40 EUR/MWh. Concerning the solar fraction over the total thermal energy supply, 20% can be achieved without TES installation, whereas a larger solar fraction can be accomplished with seasonal TES. Among the different technologies, water pit and borehole seasonal TES systems result in the most used in conjunction with SDH. Moreover, the installation of the seasonal TES system paves the way for more heat production flexibility and integration of large-scale heat pumps that improve the performance of the overall SDH system [23]. Further penetration of non-programmable renewable power generation can be also achieved thanks to the DHC systems since excess electricity generated can be used directly or stored in the form of heat or cold in TES systems avoiding the limitation of photovoltaic (PV) and wind production. Furthermore, connecting different sectors through power-to-heat technologies, like electric boilers and HPs, can provide valuable balancing services for the power grid, such as frequency regulation.

The comparison between the 4GDH and the 5GDHC reveals significant differences in their capabilities and applications. While 4GDH is designed primarily for direct heating purposes, it requires the use of two separate distribution networks in urban areas to accommodate both heating and cooling demands. On the other hand, 5GDHC is not suitable for direct heating, but it offers a remarkable advantage by seamlessly meeting both heating and cooling demands for different buildings through the same pipelines. This feature makes 5GDHC a more versatile and efficient system, as it eliminates the need for multiple networks, simplifying the overall infrastructure and providing a more integrated and flexible solution for thermal energy supply. The transition from 4GDH to 5GDHC represents a significant leap in district heating and cooling technology, enabling more comprehensive and sustainable energy systems that cater to diverse heating and cooling requirements with increased efficiency and environmental benefits.

In the context of the evolution of district heating networks, Figure 2-1 illustrates the progression from the first generation to the 5th generation. This figure provides a visual representation of the advancements and changes that have occurred over time in the design and operation of district heating systems.

2.2 Substations in 5GDHCNs

In conventional DHC networks, energy is transformed from a higher to a lower-level temperature in units called substations (like electrical substation). These substations consist of key elements such as heat exchangers, along with mixing and control equipment. Usually, each building connected to the network has its own substation, although alternative solutions may exist, like area substations serving local distribution networks or apartment substations allowing individual regulation and billing for each flat in a building [9]. By reducing the supply temperature and raising the supply-return temperature difference, it is possible to reduce heat losses and increase generating efficiency, but end-user temperature requirements have an impact on constructing substation design, departing from the conventional idea. Furthermore, safety and comfort performance, along with reducing maintenance problems, are typically favored by hydraulic separation, which separates the building circuit from the network. However, in modern DHC networks designed to operate at lower supply temperatures, there is no longer a requirement to convert energy from high to low temperature levels. Instead, these networks need to intelligently incorporate boosting solutions to achieve the necessary temperature increase. The FLEXYNETS project [24] focused on the creation of a 5GDHCNs that operate at "neutral" temperature levels ($30\pm 0^\circ\text{C}$), aiming to decrease energy transportation losses. It is proposed to use HPs for exchanging heat with the DHC network on the demand side, thereby supplying the required heating and cooling to the buildings. The building substation layout obtained from FLEXYNETS simulation analyses is depicted in Figure 2-2.

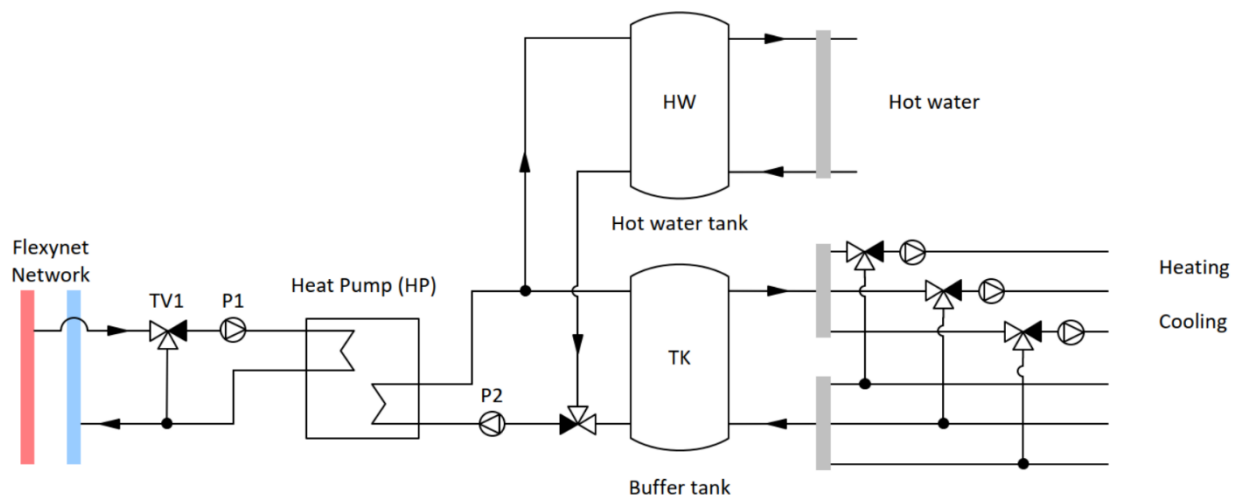


Figure 2-2. FLEXYNETS residential substation [24]

The objective of this design is to utilize a neutral-temperature network as the source for a reversible HP to cover DHW, space heating (SH), and space cooling (SC) needs. The design includes both a storage tank for DHW and a buffer tank for the heating and cooling supply. Nevertheless, this approach presents certain technical constraints in 2-pipe networks, as mentioned in [24]. The most significant characteristics and exemplary instances of "prosumer" substations were collected and assembled in [12]. The term "prosumer" is used for constructing substations in 5GDHC networks, where each customer can function as either a "consumer" or a "producer" of thermal energy when the network is intended to cater to both heating and cooling requirements. The survey reported various versions of these building "prosumer" substations, and Figure 2-3 illustrates three of the most relevant substation configurations.

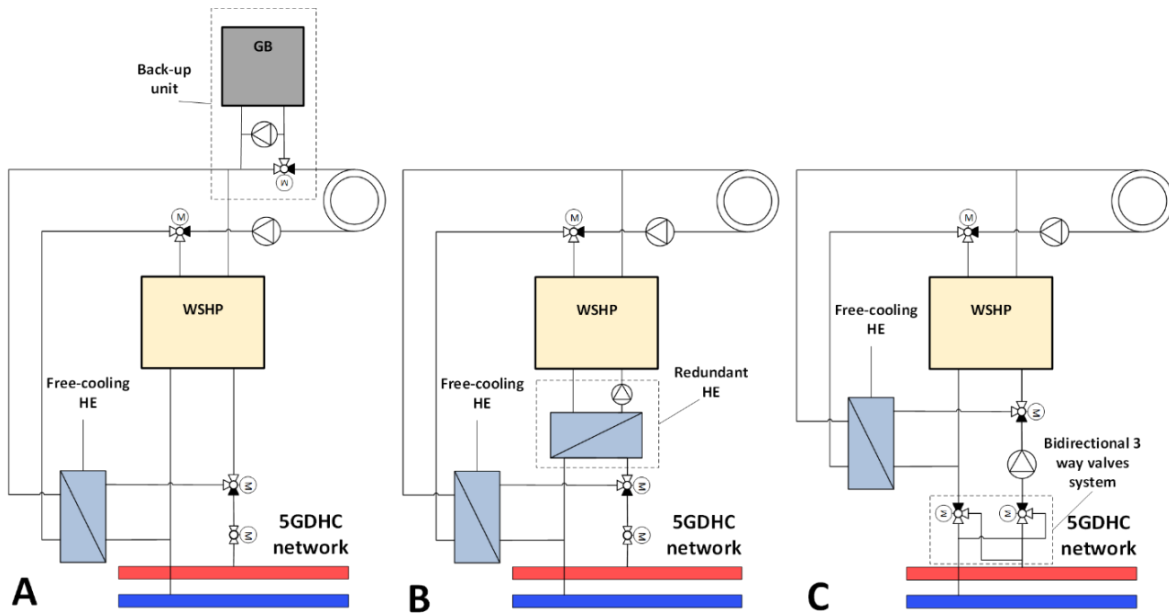


Figure 2-3. Details of the "prosumer" substations adopted in some of the surveyed 5GDHC systems [23]

The simplest solution is "**Substation A**" since it includes a direct connection of the WSHP to the network for active heating/cooling. Additionally, two 3-way diverter valves enable connection to a heat exchanger, which is installed in parallel with the WSHP to facilitate free-cooling operation. When retrofitting existing systems, a backup unit can be retained to operate in bivalent mode. In certain cases, it can be linked in series to raise the supply temperature from the WSHP, particularly for DHW production or when high-temperature water distribution is necessary. This approach

allows the WSHP to function with a lower supply temperature and enhance its own Coefficient of Performance (COP).

Some added complexity arises in "**Substation B**" due to the incorporation of a redundant heat exchanger (HEX) between the WSHP and the network. This inclusion ensures hydraulic separation, safeguarding the WSHP from potential fouling risks. However, this results in increased costs and thermodynamic irreversibility. The HEX necessitates a temperature difference for heat exchange in both heating and cooling modes, causing the intermediary circuit between the WSHP and the redundant HE to operate at temperatures lower and higher than that of the network. As a consequence, the performance of the WSHP is negatively affected. Based on the surveyed cases, the presence of this HE is often obligatory, but in certain instances, it may be optional depending on specific local regulations and/or engineering practices.

The most advanced solution is "**Substation C**." It involves installing two diverter 3-way valves on the primary loop of the WSHP between the hydraulic pump and the network. This arrangement allows for separate rejection of hot water (during active or free-cooling mode) into the warm pipeline and cold water (during heating mode) into the cold pipeline. This separation prevents thermal mixing within the network, preserving the exergy content of the DHC transfer fluid. Consequently, the HPs along the network can operate with the most efficient boundary conditions [23].

2.3 State of the art control of strategies in DHNs

The state of the art in control strategies in DHNs encompasses a spectrum of approaches, ranging from basic to advanced techniques. At the fundamental level, conventional control strategies have focused on maintaining system stability and ensuring consistent heat supply to consumers. These basic strategies typically involve simple ON/OFF control for heat generators, basic temperature regulation, and fixed flow rates. While effective to a certain extent, these conventional methods lack adaptability and optimization, leading to potential inefficiencies in energy usage.

In recent years, significant advancements have been made in DHN control, leading to the adoption of more sophisticated and intelligent techniques. Advanced control strategies now incorporate predictive modeling, data analytics, and machine learning algorithms to optimize system performance and energy efficiency. By considering real-time data, weather forecasts, consumer demand patterns, and heat source characteristics, these approaches can dynamically adjust heat

generation, distribution, and storage, maximizing renewable resource utilization and minimizing energy waste.

2.3.1 Basic Control Strategies in conventional DH/DC Systems

Six independent basic control strategies operate simultaneously in a conventional DH network, as depicted in Figure 2-4 and listed in the following. These are usually implemented in the form of classical control such as rule-based or proportional-integral-derivative (PID). According to Frederiksen and Werner (2014) [9], the ones from A to E are implemented at the production and pumping station level, whereas the control strategy F is implemented at the user substation level.

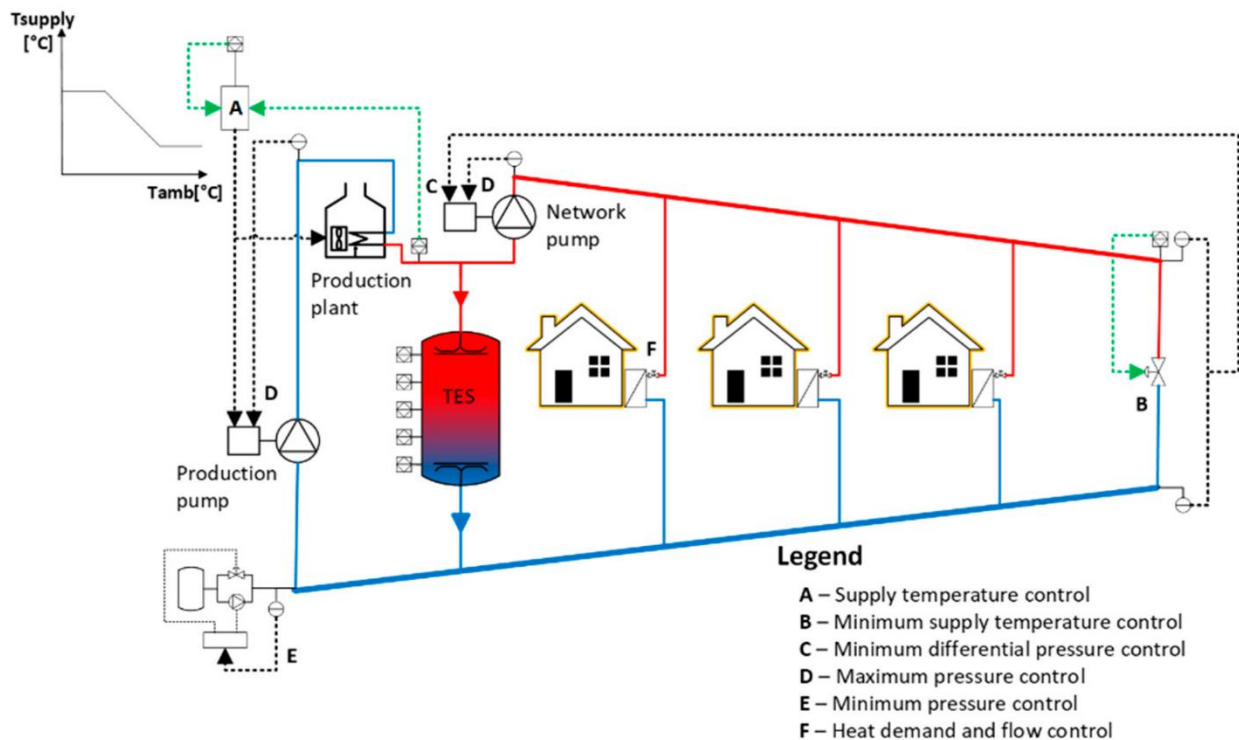


Figure 2-4. Basic control strategies in conventional district heating (DH) systems [26].

A. Supply temperature control: The goal of this control is to modulate the thermal power at the heat generation plant to reach a fixed supply temperature set-point. The latter is generally determined by means of a heating curve as a function of the external ambient temperature, and it is high enough to satisfy the temperature level required for all the customer-sited heat emission systems.

B. Minimum supply temperature control: This control is important, especially in summer, when the DH system operates to supply only the DHW load. During the night, for instance, a by-pass

between the supply and return pipelines at the end of the network allows maintaining a small recirculation in order that the supply temperature always satisfies the comfort level for the users.

C. Minimum differential pressure control: It is essential to maintain a minimum differential pressure between the supply and the return pipelines at the farthest substation from the network pumping station. In this way it is assured that the pressure head is enough to supply all the substations in the between.

D. Maximum pressure control: The pumps are controlled to avoid over-pressure at the supply line that could damage the network.

E. Minimum pressure control: The minimum pressure of the network that occurs at the suction of the pumps is controlled to avoid cavitation and damage of components.

F. Heat demand and flow control: These control strategies are implemented at the user substation level. For instance, a climatic control can be implemented to set the supply temperature on the substation's secondary side. A modulating valve is then used to achieve this set-point by controlling the flow rate on the substation's primary side.

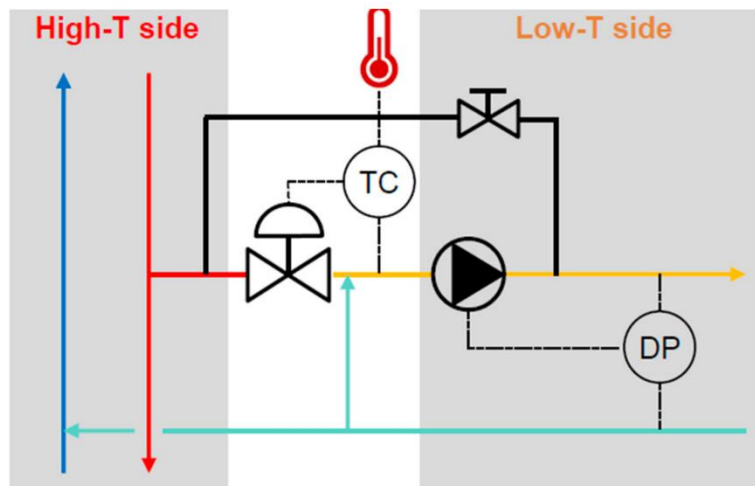
TES systems based on short-term tanks provide several advantages in conventional DH/DC networks. They allow equalizing the load of the heat production plants, while heat demand by consumers is fluctuating, and covering the peak demand by avoiding that peak generation units switch on with high operational costs. Moreover, TES systems allow operating the system when the heat demand is below the technical minimum of the heat production plant and increasing the flexibility of CHP systems by permitting electricity generation during off-peak hours of the heat load without wasting the heat produced. Several temperature meters are usually installed along the height of a tank TES to monitor the temperature stratification and state of charge. To exploit the capacity of TES directly connected to the DH network such as in Figure 2-4, few further control measures are needed: the charging and discharging phases are activated automatically by generating the right amount of positive/negative differential pressure at the connections of the TES at the supply and return DH pipelines by controlling properly the network and production pumps. Moreover, usually, a control to limit the minimum temperature at the top during discharging and the maximum temperature at the bottom during charging can be beneficial to avoid thermocline destruction. The same basic control strategies shown in this section for conventional DH applications are also valid for DC systems. The latter usually operate with a smaller temperature

difference between supply and return concerning DH, with consequent larger flow rates and pumping electricity consumption to supply the same thermal power.

2.3.2 Basic Control Strategies in 4GDH and 5GDHC Systems

The basic control strategies shown in the previous section are usually applied also in 4GDH systems. Generally, these have a supply temperature of $70\div 35$ °C, while if it is lower, small booster HPs are required at the user-sited substation to satisfy minimum DHW comfort temperature and limiting legionella proliferation. The challenge that the current 3GDH systems are facing in the transition towards 4GDH is the supply temperature reduction. This is achievable mainly in those areas with new or refurbished buildings by zoning the DH network, maintaining a high-temperature backbone and low-temperature subnetworks. In this regard, a prototype of a mixing shunt system in a containerized solution has been installed in the DH network of Brescia (Italy) in the framework of the H2020 TEMPO project [27]. In contrast, a commercial solution has been recently installed in the DH network of Albertslund (Denmark) in the framework of the H2020 REWARDHeat project [28], as shown in Figure 2-5. These shunt systems usually include the minimum supply temperature and the minimum differential pressure controls for the subnetwork and unlock the possibility to absorb local peak loads by operating the subnetwork according to a dynamic heat storage strategy. Other benefits of the network supply temperature reduction are:

- The decrease of the distribution heat losses since also the return temperature decreases.
- The increment of the DH network capacity thanks to the larger temperature difference between supply and return at the backbone. This means that more customers could be connected to the existing infrastructure and that a lower flow rate is needed to supply the same thermal power.
- The increment of the life of some DH components thanks to the lower operating temperature.
- The increment of the efficiency in condensing boilers, CHP plants, HPs and solar thermal fields thanks to the lower return temperature.



(a)



(b)

Figure 2-5. (a) Piping & instrumentation diagram of the mixing station installed at the DH system of Brescia [26]; (b) shunt system installed in the district heating and cooling (DHC) system of Albertslund [28]

Nevertheless, to maximize these benefits, it is essential to reduce the return temperature of the subnetwork by acting on the customer's substation and heating system. Apart from the substitution of some critical radiators with high panels or the extension of the heat emission surface, it might be useful to mitigate the effect of high flow rate occurring for instance due to night set back, with control using thermostatic radiator valves (TRV) and return temperature sensor [29].

As far as 5GDHC networks are conceived, basic control strategies can differ from conventional DH/DC systems and 4GDH. 5GDHC systems, which usually operate with a network temperature in the range of 30 ± 0 °C, include HPs at the customer-sited energy transfer station that are in charge of meeting the required heating/cooling supply temperature. For this reason, supply temperature control is usually not implemented at centralized level, and several systems operate with free-floating temperature that is a result of the balance between the heating and cooling loads as well as thermal energy source temperature throughout the year [6]. Minimum supply temperature control is in some cases implemented to limit the risk of very low temperature and possible freezing in the pipes using back-up systems [30]–[32]. Differential pressure control is usually present only when centralized pumping stations are used and, in some cases, together with redundant heat exchangers that separate the HPs from the thermal grid. In other cases, such as in small loops where decentralized hydraulic pumps are installed at the substation level, differential pressure control is absent. Anyhow, the minimum pressure in the network is met by means of pressurization stations.

Remote smart metering is a mature technology, and it is an important aspect to improve the operation in both 4GDH and 5GDHC systems such as with the implementations of demand response (DR) strategies for peak shaving as well as to detect faults in substations. Nevertheless, there are still some barriers to overcome to achieve this as the lack of trust between the DHC operators and the users as well as additional services to provide by DHC companies such as substation maintenance [32].

2.3.3 Advanced Control Strategies in DHC Networks

Given the fact that smart DHC grids are becoming more complicated than before due to the exploitation of non-programmable renewable thermal energy sources and sector-coupling with the power grid, conventional strategies, even if they are robust, are not sufficient to cope with these challenges. Smart control strategies at centralized and decentralized levels are of paramount importance and need to be applied on top of the basic control strategies. These strategies against challenges such as weather uncertainty, user behavior and customer-sited substation operation are trying to achieve good performance of the system satisfying capacity constraints at some points of the DH network.

Linear programming (LP) and mixed-integer linear programming (MILP) are commonly used to individuate complex energy systems' best size or scheduling. A recent application of LP related to this scope for a 5GDHC system supplying several buildings of a university campus can be found in Wirtz et al. (2020) [33], where the problem has been set up in Python and solved by means of the solver Gurobi. A MILP model for the design and operation of an urban energy system in the center of England has been presented by Samsatli and Samsatli [34]. This model is based on a flexible value web framework for representing integrated networks of resources and technologies. It can be used for different temporal and spatial scales. Researchers in [35] have applied MILP to minimize the total annual cost for an industrial area located in the northeast of Italy with the integration of solar thermal production. Their results showed that the yearly total cost and primary energy consumption reduce 5 and 15%, respectively. In the framework of the H2020 FLEXYNETS project [36], to reduce the overall heat generation cost of a DH supplied by a large share of low-grade excess heat, Vivian et al. [37] indicate that the suggested MILP-based controller managed to reduce the system operational costs by 11% with respect to a standard rule-based control. Similarly, in Schütz et al. [38], the authors applied a MILP method to minimize the total costs. To this end, four different strategies for calculating temperature stratification inside thermal

storage are performed. Procedures are tested with an operation scheduling use case that aims at minimizing operational costs by achieving a reduction of 6–7%. MILP has been applied in the work of Giraud et al. [39] using the commercial solver CPLEX in a receding horizon fashion with a timestep of 15 min and a prediction horizon of 24 h. Differently from other works, here, the optimal scheduling of the generation units assessed takes into consideration the effects on the DH network with the integration of a dynamic model in Modelica. The simultaneous optimization of DH production and distribution resulted in the use of the DH network as storage by increasing the supply temperature prior to a peak of the demand, reducing the differential pressure and avoiding the start-up of expensive peak units. In [40], a more complete overview of the results is provided by the authors showing that with respect to an empirical piling method, the production optimization only was capable of achieving 6.4% of savings on the production costs and no energy savings, whereas with both production and distribution optimization, it was possible to obtain 8.3% of savings in production costs and 1.7% reduction in the energy consumption. Researchers in [41] presents an optimization-based investment planning approach to size a heat transfer station for connecting industrial sites to district heating systems. The approach utilizes MILP and takes into account diverse energy demands, waste heat, and transformation strategies using regret optimization. The study demonstrates positive net present value, reduced energy costs, and lower carbon dioxide emissions, achieved through efficient utilization of energy systems and waste heat integration. Merkert et al. [42] introduce a Mixed-Integer Linear Programming (MILP) approach to optimize the supply temperature in a district heating network for short-term periods. This optimization determines the specific time when the network should be heated and the corresponding temperature increase. Based on their model, the temperature propagation wave reaches the buildings with a known a-priori temporal network delay. Gabrielli et al. [43] proposed a mixed-integer non-linear program (MINLP) to optimize the operation of the 5GDHC network at ETH Zurich. They used bilinear products of mass flow rate and fluid temperature to address the computational complexity. To manage this complexity, they transformed the model into a MILP by linearizing the efficiency curves of heat pumps and assuming a fixed profile for the mass flow rate. The 5GDHC network studied had low-temperature variations, allowing them to replace the highly non-linear relationship between heat output, electric power, and inlet temperature at the evaporator of the heat pump with a bivariate linear approximation. However, for 5GDHC networks

with larger temperature fluctuations, the linear approximation resulted in significant errors and was, therefore, not applicable.

The strengths of MILP formulation in addressing optimal operation problems are acknowledged, but its limitations are noteworthy. One of the main challenges of MILP is that it suffers from combinatorial complexity, which can make it difficult to solve large problems to global optimality [44]. The computation time to solve a MILP problem to global optimality via a branch-and-cut solver highly depends on the problem size, the choice of design variables, and the quality of optimization constraint formulations [45]. To address these shortcomings, meta-heuristic algorithms, a type of optimization technique that employs iterative processes to explore optimal responses, are utilized. Genetic algorithm (GA), particle swarm optimization (PSO), and ant colony optimization (ACO) are some of the most used population-based meta-heuristic algorithms. By integrating GA with MILP, the optimization process becomes more versatile and capable of addressing complex, non-linear problems, thereby enhancing the quality of the obtained solutions.

A two-level optimization algorithm contain MILP and GA is proposed in Urbanucci et al. [46]. In the case study, the cogeneration unit directly reaches 70% of both the thermal and electric yearly demand, while 16% of the subsequent is met by storage.

Likewise, a hierarchical optimization strategy is used in Casisi et al. [47]. The higher layer for binary decision is dedicated to the GA, while the MILP algorithm is used in the lower to choose the system's optimal operation. Results show a remarkable reduction in computing time.

The multi-agent system (MAS) approach benefits several critical computer applications such as communication network configuration, process control, planning or concurrent systems. MASs are formed by several agents that have a considerable number of communications with each other. In general, agents act to support the users and have different goals and motivations. An agent is defined as an autonomous entity that can be viewed as perceiving and acting upon its environment. An agent must be able to communicate with other agents [48]. To interact successfully, agents must have the ability to cooperate, coordinate and negotiate with each other, almost as people do. To improve the monitoring and control of a DH system through the use of agent technology, Wernstedt and Davidsson [49] developed a MAS approach. In order to shave the peaks and prevent entering the boilers in the circuit, the authors of [50] have applied the MAS approach. Yielded results show that MAS was capable of decreasing the peak loads by up to 20%. In the same way, Lacroix et al. [51] used the MAS approach to control a compressed unit providing heating,

ventilation and domestic hot water production in a low-energy building. However, findings show that the suggested methodology managed to increase costs by only 2.5%, but they improve thermal comfort by 35%. MAS and PSO's combination is the main idea in Wang et al. [52]. The aim is to maximize the comfort index using minimum power consumption, and the findings indicate the effectiveness of the proposed method.

The MAS approach has been recently applied to 5GDHC systems that enable the concept of decentralized prosumers for all the connected substations. In particular, in Bünning et al. [53] the performance of two 5GDHC systems located in San Francisco and Cologne exploiting an agent-based control have been assessed in comparison with a conventional gas-fired DH and individual chillers solution for space cooling. By exploiting the coordinated balancing effects of several decentralized prosumers with heat pumps and chillers, this control strategy was able to maintain the average temperature of the system within 2 K around the setpoint all year around showing that this approach is beneficial with respect to free-floating temperature control. Future technology could match blockchain with the MAS approach. Blockchain application in 5GDHC have been investigated in the framework of the D2Grid project [76] and is going to be demonstrated at the demo case of Paris-Saclay (France) [77]. The goal is to apply a new business model where smart contracts can be signed automatically and with the exploitation of dynamic energy tariffs to flatten the peaks in the heating and cooling demands by promoting flexibility and demand response (DR) strategies at the customer level. In this regard, an overview of DR applications in the DHC sector is presented in the next section.

In recent years, MPC has become a high-tech solution to several complicated control problems. It attracted research communities' attention in different fields and in particular in the DHC sector.

2.4 Model Predictive Control

MPC is described as an "approach" to control design, not a specific algorithm, signifying a way of thinking in control systems. Users ideally interpret the approach to define algorithms suitable for their own needs. One of the reasons why predictive control is considered logical is that it is based on human behavior, which serves as a good starting point for designing automation techniques. For example, when looking at a PID controller, it can be realized that it is a simplification of a human technique for controlling simple systems. Similarly, humans use predictions for common strategies [54]. For instance, in the context of "driving a car," a core component is that drivers look ahead and anticipate future "targets" or demands, such as changes in the road, pedestrians, other

vehicles, and speed limits. Therefore, anticipation, or prediction, helps determine effective control strategies.

Figure 2-6 illustrates the common traits shared by all the methods within the MPC category.

- For every time step k , the dynamical model of the process is used to predict the future output $y_{k+i|k}$, $i = 1, 2, \dots, N$. The notation $y_{k+i|k}$ denotes the value of the variable at time $k + i$, calculated at time k . The future output relies on both the current state of the system and the current and future control input signals $u_{k+i|k}$, $i = 0, 1, 2, \dots, N$. These control input signals are determined by optimizing specific performance criteria.
- The process receives the control input signal $u_{k|k}$ while disregarding the remaining control inputs. In the subsequent time step ($k + 1$), the updated system state x_{k+1} is already known, and the process is repeated, making predictions for the output, and calculating the control action using the updated information.

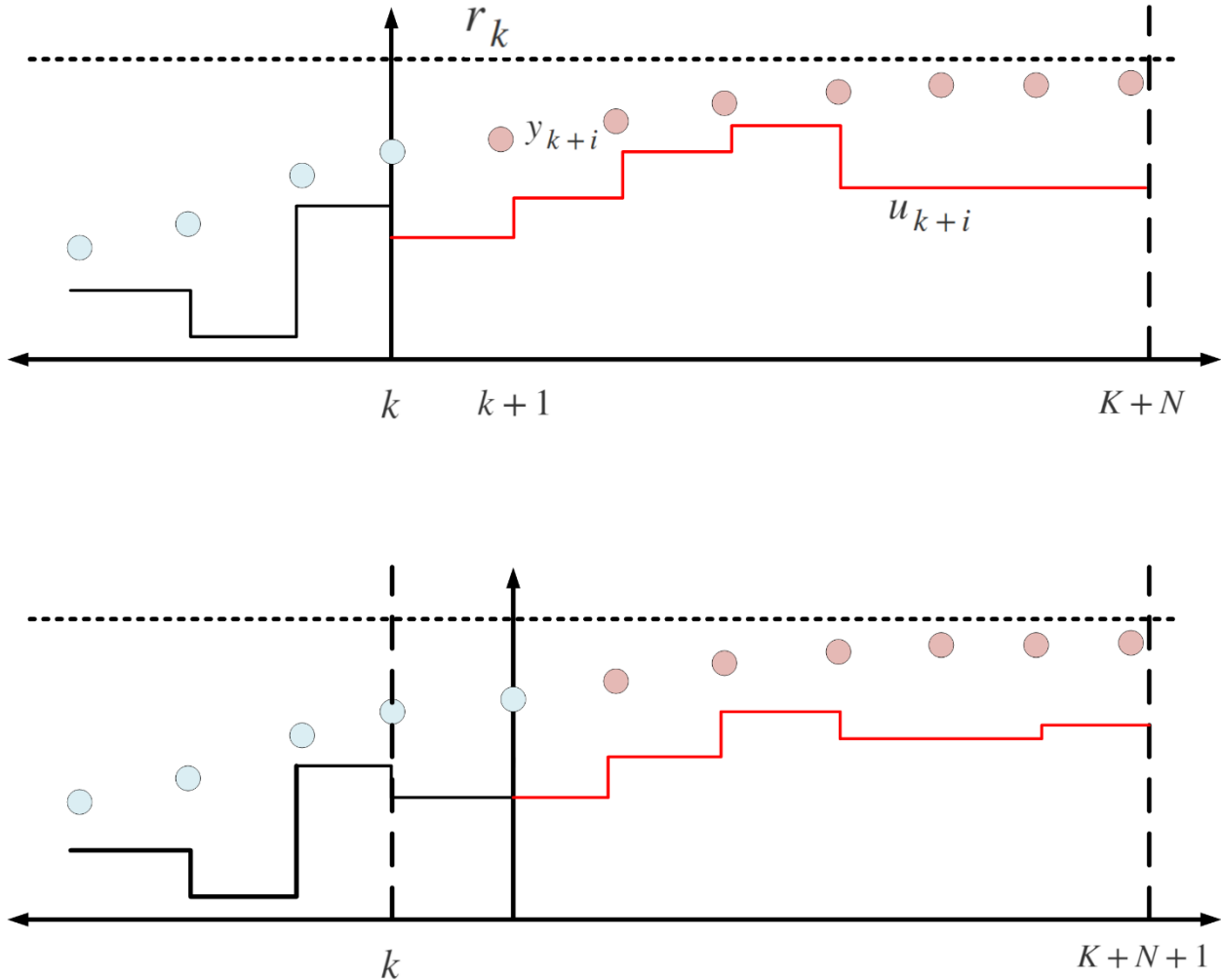


Figure 2-6. MPC strategy. The vertical black arrow marks the present time. Black line past commands. Red line future commands.

Figure 2-7 illustrates the fundamental structure of the approach. This strategy employs a dynamical model to forecast the future states of the process based on the current state and anticipated control signals. These control signals are determined through optimization of an objective function, while adhering to system state and control input constraints, to achieve an optimal control sequence. The prediction horizon denotes the maximum number of time steps considered for predicting the system states, and similarly, the control horizon represents the number of time steps used for calculating future control actions. Since the number of time steps for predictions is finite, this approach is known as finite receding horizon control. Nevertheless, it is worth noting that a finite prediction horizon may compromise the stability of the control system, as discussed in later sections.

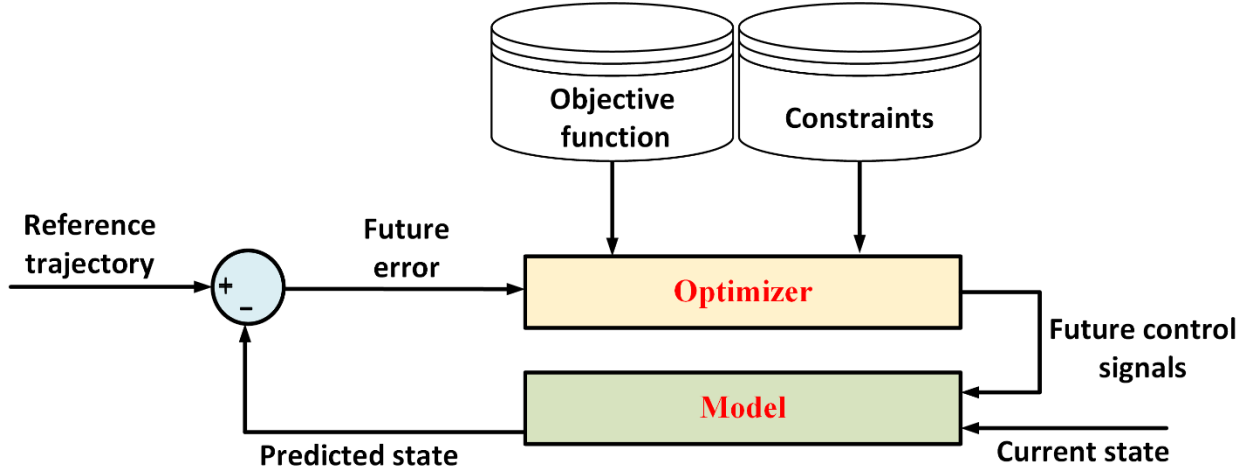


Figure 2-7. Basic design of MPC

The importance of the MPC strategy lies in its objective function. This function serves to express the intentions behind designing the control system and measures the system's performance through the use of a suitable mathematical function. Depending on the control problem, the objective function can take on different forms, such as linear (e.g., economic MPC), quadratic (e.g., nominal MPC), or even nonlinear.

Currently, the focus lies on tracking a specific desired path with minimal input requirements. The system described in Eq. (2.1) allows us to formulate the objective function J for the tracking problem as follows:

$$J(\mathbf{Y}, \mathbf{U}) = \sum_{i=1}^N (\mathbf{y}_{i+k} - \mathbf{r}_i)^T \mathbf{Q} (\mathbf{y}_{i+k} - \mathbf{r}_i) + \mathbf{u}_{i+k}^T \mathbf{R} \mathbf{u}_{i+k} \quad (2.1)$$

The prediction horizon is represented by N . The system states and control inputs have associated positive semi-definite and positive definite weighting matrices, \mathbf{Q} and \mathbf{R} , respectively. The reference value after i time steps is denoted as \mathbf{r}_i . Also, \mathbf{y} and \mathbf{u} are representing the output and input vector. The objective function shows the error between the reference value to be achieved in the future and the future system states. In real-world scenarios, knowing the reference trajectory beforehand allows the system to react in advance, avoiding time-delay effects. As shown in Eq. (2.2), \mathbf{U} is a sequence of control actions you might apply and \mathbf{U}^* is the best sequence of control actions as determined by the MPC optimization process.

$$\begin{aligned} \mathbf{U} &= [\mathbf{u}_k \quad \dots \quad \mathbf{u}_{k+N-1}] \\ \mathbf{U}^* &= [\mathbf{u}_k^* \quad \dots \quad \mathbf{u}_{k+N-1}^*] \end{aligned} \quad (2.2)$$

It should be noticed that, for consistent representation and clarity, we have adopted a notation convention: vectors are denoted by bold lowercase letters, while matrices are indicated by bold uppercase letters.

Constraints are applied to nearly all real-world dynamical systems like car driving, stirred tank systems, and power systems. Consequently, the control action that activates the process must be contained within a specific range, and likewise, the system states should be kept within an allowable limit. The system states and control input sequence are required to meet these conditions.

$$\begin{aligned} \mathbf{x}_k &\in \mathbb{X} \\ \mathbf{u}_k &\in \mathbb{U} \end{aligned} \tag{2.3}$$

where \mathbb{X} is a convex, closed subset of \mathbb{R}^n and \mathbb{U} is a convex, compact subset of \mathbb{R}^m and each set contains the origin in the interior of the set. In general, constraints are treated in two ways in MPC.

- **Soft Constraints:** In a soft constraints approach, the constrained element can break the rules, but it will be penalized heavily for doing so. As a result, the decision to balance between violating the constraints and incurring the penalty is made by the controller. Typically, this method is applied to output variables' restrictions.
- **Hard Constraints:** The limitations on control input are typically regarded as strict rules. In this setting, the constrained variable cannot break these rules. Usually, in MPC, the constraints are included as linear inequalities, similar to problems in mathematical programming.

The objective function J is minimized by an optimizer to obtain the optimal control sequence, while taking into account the constraints and system dynamics.

$$U^* = \min_U J(\mathbf{Y}, \mathbf{U}) \tag{2.4}$$

Subjected to

$$\begin{aligned} \mathbf{x}_{k+i+1} &= A\mathbf{x}_{k+i} + B\mathbf{u}_{k+i}, i = 0, 1, \dots, N-1 \\ \mathbf{y}_{k+i} &= C\mathbf{x}_{k+i} + D\mathbf{u}_{k+i}, i = 0, 1, \dots, N \\ \mathbf{x}_k &= \mathbf{x}(k) \\ \mathbf{x}_{min} &\leq \mathbf{x}_{k+i} \leq \mathbf{x}_{max}, i = 0, 1, \dots, N-1 \\ \mathbf{u}_{min} &\leq \mathbf{u}_{k+i} \leq \mathbf{u}_{max}, i = 0, 1, \dots, N-1 \end{aligned} \tag{2.5}$$

The optimal control input policy, denoted as $U_i^*|_{i=1}^N$, is designed to minimize the difference between the reference temperature trajectory and the future states, considering the system dynamics and imposed constraints. In simpler terms, the U_i^* policy helps steer the system states towards the desired reference values. The values x_{min} , x_{max} , u_{min} , and u_{max} represent the minimum and maximum allowable ranges for the system states and control inputs. To implement the control law, only the first component, U_1^* , is used to compute the system state x_{k+1} . Subsequently, as new information becomes available regarding the reference trajectory, constraints, and disturbances (which will be discussed later), the optimization process is repeated using x_{k+1} as the current state of the system. This approach follows the receding horizon control strategy.

2.4.1 MPC in DHNs

MPC is based on a predictive process that exploits a dynamic model of the system and allows finding the vector of the manipulate inputs over a time horizon by solving an on-line constrained optimization problem that takes into account the system details [55]. For instance, an MPC controller based on a dynamic programming (DP) optimization algorithm has been presented in Saletti et al. (2020) [53] to supply the thermal energy to a school complex located in Northern Italy. Results show a decrease in natural gas consumption of the boiler up to more than 7% in comparison with a standard PID controller. In De Lorenzi et al. (2020) [54], the same tool and approach are applied in different case studies. The comprehensive smart control strategy consists of pledges efficient energy distribution, flexibility and low-carbon energy integration. Achievements are a 6% reduction in operating cost and up to 34% in energy consumption, whereas meeting consumers' needs. Moreover, MPC has been applied in Verrilli et al. (2017) [55] by scheduling boilers, TES units and flexible loads. Results show that the MPC succeeded in reducing operating and maintenance costs in a DH power plant. This methodology integrated projection on fluctuating demand within the optimization problem and answered it in a receding horizon fashion. Labid et al. (2014) [56] developed an MPC to improve the thermal storage tank management in a multi-energy district boiler. The results revealed that the controller reduced fossil energy consumption and CO₂ emissions, while the economic profit increased. A MPC introduced in Lennermo et al. (2019) [57] has been applied to decentralized solar thermal collectors (STC) fields connected to a DH network in the return-supply configuration. The authors showed that the MPC implementation in the real SDH system in Lerum (Sweden) operated in a robust way solving the

problems of the previous PID controller that was not capable of limiting severe supply temperature and flow rate cycling variations that can be a cause of fatigue problems in buried steel pipes. Sometimes for covering the disadvantages of MPC and obtaining the best performance and result, MPC has been merged with other methods. For example, to control the supply temperature in the DH network, authors in Grosswindhager et al. (2013) [58] used the combination of the MPC and fuzzy direct matrix control (FDMC). Findings confirm that FDMC can command the inherent nonlinearity in the acknowledgment characteristics of DH systems by considering the volume flow rate at the plant as a fuzzy variable. Additionally, the trade-off between pumping and heat loss costs can significantly impact minimizing operational costs. A tool named XEMS13 using MPC strategy has been introduced in Lazzeroni et al. (2019) [59] in order to optimize operational costs by considering technical and operational constraints. This tool is developed by the Energy Department of the Politecnico di Torino and LINKS. Different configurations with increasing cost-saving, installation costs, renewable energy source generation and primary energy saving are presented, and results demonstrated the success of the method. Authors in [56] aimed to enhance MPC performance in buildings by addressing weather forecast uncertainty. An error model, based on easily measurable data, was introduced to improve weather forecast data quality. The MPC with the error model achieved significant energy cost savings (3.4%) and reduced indoor temperature violations (73%) compared to conventional controllers. The introduction of the error model consistently improved MPC performance, even with low forecast errors, making it beneficial for practical application in buildings. Hering et al. in [57] focused on optimizing a low-temperature district heating network with a high share of waste heat from high-performance computers. The network includes heat pumps with temperature-dependent characteristics, modeled using quadratic correlations. An optimization model, a mixed-integer quadratically-constrained program, is used to optimize the heat pumps' operation along with thermal energy storages and pipe network temperatures. The optimization achieves 1.55%-5.49% electrical energy savings, depending on heat and cooling demands, by utilizing thermal energy storages and controlling flow and return temperatures. In [58] MPC shows promise in improving heating, ventilating, and air conditioning (HVAC) system efficiency and flexibility. However, widespread adoption faces challenges due to expertise, data quality, and risk aversion. This study implements MPC using an open-source tool-chain in a real office building, achieving 40% HVAC energy savings. It discusses practical challenges and estimates implementation effort, aiming to guide

future workflows and reduce implementation complexity. In [59], authors applied MPC to a university heat prosumer with data center waste heat and thermal energy storage. The MPC framework minimized energy costs and improved cooling system stability, resulting in up to 3.2% monthly energy cost reduction compared to conventional control. Lyons et. Al in [60] proposes a novel approach that combines model reduction techniques with state-of-the-art building energy modeling tools within an MPC framework. The approach is demonstrated through a case study involving a 95-flat communal heating system. Both centralized and decentralized approaches are explored, particularly their ability to incorporate externally imposed constraints on the supply. A forecasted load-and time delay-based MPC has proposed in [61] for district energy systems. The MPC model reduces energy consumption by 9.56% in summer and 7.75% in winter compared to conventional feedback control, and by 5.30% in summer and 2.61% in winter compared to load feedforward fuzzy control. Jansen et al. in [62] presented an advanced control strategy based on MPC, for DHNs. The MPC outperforms the conventional rule-based controller, reducing thermal discomfort and lowering electrical energy use by 3% in winter and 17% in spring. It considers the entire system, including heat demand, and uses anticipation and flexibility for better performance. In [63] MPC has been used to regulate a DH station in China, achieving higher room temperature stability and flexibility. MPC reduced room temperature fluctuations and energy consumption. Practical application showed energy consumption reduced by 5.9% and 7.9% over two years, with improved thermal comfort rates. Bella et. Al in [64] proposed a method for optimizing district heating systems connected to the electrical grid. It combines physical and identified piece-wise linear models for efficient optimization. The method was tested on a real district heating plant in Novate Milanese, Italy, showing promising results with significant cost and gas consumption reductions. Buffa et. al [12] utilized advanced MPC with recurrent artificial neural networks to improve energy transfer station operation in 5GDHC systems. The MPC controller achieved up to 14% electricity consumption shift from on-peak to off-peak hours, enhancing grid flexibility and thermal-electric sector coupling. A predictive control strategy was developed in [65] for the DH system at the Drake Landing Solar Community in Canada. The strategy aims to minimize energy consumption while maintaining a high solar fraction. Simulation results show it can save about 47% of pump electricity use annually, resulting in cost and greenhouse gas emissions reductions of 38% and 32% respectively. Authors in [66] compared two control strategies for a multi-energy DH network DHN: Reactive Rule-Based Control (RBC) and MPC. MPC reduces operational costs

by up to 5% compared to RBC, especially with variable energy costs, intermittent solar energy, and storage capabilities. The study provides a methodology and tools for efficient implementation and validation of complex MPC strategies using Modelica-based simulation and various control strategies. Taylor et. al [67] focuses on optimizing 5GDHCN using MPC to match demand with low-cost electricity supply. To enable MPC application, the paper extends a control-oriented modelling framework for multi-energy systems to accommodate 5GDHC network, including hydraulic pumps, thermodynamic cycle devices (e.g., WSHPs), and multi-energy networks. An economic MPC (eMPC) scheme is proposed for energy management in 5GDHC-based smart districts. A case study comparing the proposed eMPC controller with rule-based control shows its superiority in achieving economic operation of a smart district.

2.5 Model Identification

A wide area of research is organized by the underlying processes described by systems. The methods used in the process of system identification are briefly outlined in this section. The modeling approach chosen depends on the complexity, dynamics, and nonlinearity of systems. The existing approaches in the field of energy systems can be broadly categorized into three main groups.

White-box models, being grounded solely on physics, indeed require a significant amount of effort and time to develop. A comprehensive understanding of the system's physical parameters and the equations governing its behavior is essential to construct an accurate model. The complexity of these models can lead to slow execution in simulations, making them computationally intensive. Despite the challenges, for example, white-box models offer a unique advantage in that they can simulate buildings that have not yet been constructed, provided that all relevant physical properties are known. This capability makes them valuable tools for architects and engineers in the design phase, allowing them to explore various scenarios and optimize the building's energy performance even before construction commences [62]. In the field of energy modeling, several well-established software packages are based on the white-box approach. These tools have become instrumental in assessing energy usage and devising effective building control and operation plans. Among them, EnergyPlus, ESP-r, TRNSYS, Ecotect, and Grasshopper stand out as widely-used platforms [63], [64]. These software applications enable energy analysts and researchers to evaluate the energy efficiency of buildings, study the impact of different design choices, and propose energy-saving measures. By relying on the principles of physics, these white-

box models contribute to advancing sustainable building practices and reducing the environmental footprint of our built environment.

Black-box models, in contrast to white-box models, black-box models, also known as data-driven models, do not rely on the underlying physics or first principles of the system. Instead, they establish relationships between input and output features purely based on historical data. These models use the available data to calibrate and establish correlations, making the modeling process relatively straightforward and quick. The primary advantage of black-box models lies in their ability to handle complex systems where the underlying physics may be difficult to model explicitly. They excel in situations where the relationships between input and output variables are nonlinear and cannot be easily described by conventional physics-based equations. To construct these models in the field of energy, historical data on building energy usage and operating parameters are utilized. By analyzing the data, the model learns patterns and correlations, allowing it to make predictions and optimize energy usage in various scenarios. For training black-box models, it is essential to have on-site observations over an extended period to gather sufficient data that represents different operating conditions. This comprehensive dataset ensures that the model captures the system's behavior accurately and can generalize well to handle diverse situations [68], [69]. Commonly applied approaches in black-box modeling include ANN, Support Vector Machines (SVM) [70], and Statistical Regression. ANN is particularly useful for handling complex nonlinear relationships, while SVM is effective in dealing with classification and regression tasks. Statistical Regression, on the other hand, is a simple yet powerful technique for establishing correlations between variables [71], [72].

Gray-box models, which offers a valuable middle ground between the purely qualitative nature of black-box models and the fully physics-based approach of white-box models. Gray-box models combine both qualitative knowledge and quantitative data to develop a more comprehensive and accurate representation of the system. The gray-box modeling technique allows for the integration of prior knowledge and insights gained from domain experts. This qualitative knowledge can include factors such as system constraints, behavior patterns, and known relationships between variables [73]. By incorporating this domain expertise into the model, it becomes more interpretable and aligned with the real-world understanding of the system. Furthermore, gray-box models make effective use of available data, which may be limited or noisy in some cases. Instead

of relying solely on data-driven techniques like black-box models, gray-box models extract the most meaningful information from the available data while complementing it with the qualitative understanding of the system. The process of developing a gray-box model involves a careful selection of the most appropriate process model, considering all the currently available information [74]. This hybrid modeling approach ensures that the model's predictions are not solely data-driven but also constrained by the underlying physical principles or qualitative insights. The advantage of using gray-box models is evident in scenarios where obtaining large amounts of data might be impractical or expensive. By combining qualitative knowledge with the limited data available, gray-box models can still provide valuable predictions and insights into the system's behavior [75].

Chapter 3

3 Methodology

The methodology section in this thesis centers on the utilization of the MPC approach specifically for the optimal control of substations. MPC is applied for an end-user substation that is linked to the 5GDHC network, with a specific emphasis on its application within residential buildings.

The state of charge of TES and the temperature distribution within the storage tank are crucial inputs for decision making. Understanding both the current and projected future state of TES charge enables the MPC to effectively manage the use of stored thermal energy, contributing to energy efficiency.

The status of HPs is another key consideration. Since HPs operate using electricity, MPC must decide the optimal times for their operation. This decision depends on various factors, including the current grid electricity price. The electricity source supplying the HP and the inlet temperature to the HP, which directly affects its efficiency, play pivotal roles in the decision-making process of the MPC.

A critical factor that requires prediction is the thermal load demand within the residential building. Accurately estimating the future thermal load is essential for MPC to determine the precise amount of heating or cooling needed to meet all the heating requirements of occupants and maintain a comfortable indoor environment.

Among these factors, the prediction of thermal load demand stands as a cornerstone. It serves as a fundamental input, dictating the energy requirements within the residential building. This demand prediction is essential for crafting a well-optimized energy planning strategy, ensuring that the substation operates efficiently and effectively. Therefore, it is necessary to employ a robust and accurate load prediction model.

This model is pivotal in informing the MPC's decisions and contributing to the overall success of the optimized energy planning process. In this section, we outline the steps and methodologies used to select and implement a suitable load prediction model. This model is crucial for achieving the primary objective: utilizing the MPC approach for optimal control of residential substations connected to 5GDHCNs.

3.1 Thermal load prediction

Thermal load refers to the amount of heat energy that needs to be either added or removed from a space or system to achieve the desired temperature conditions. It can represent both the heating load and cooling load. Given that buildings use significant amounts of energy and produce considerable carbon dioxide, accurate thermal load forecasting is crucial for the optimal planning and operation of the energy systems. It helps to reduce energy waste, enhance occupant comfort, and extend the lifespan of building equipment. This type of forecasting is widely utilized in the controls of HVAC systems [2]–[7], HPs [81]–[83], and TES systems [84]–[86]. Load forecasting is typically implemented through various modeling techniques [87]. The choice of modeling approach depends on the complexity, dynamics, and nonlinearity of building energy systems, whether in a single building or multiple buildings.

As mentioned earlier, black box models are like magic boxes that provide predictions without revealing how they work inside, making them great for complex situations. White box models, on the other hand, are like transparent glass, showing you exactly how they make decisions, which is useful when understanding the process is crucial. Gray box models, as the name suggests, are a mix of both, giving you some insight into their inner workings while still preserving some mystery, often striking a balance between understanding and prediction accuracy.

Black box modeling is often preferred over white and gray box modeling in certain situations due to its inherent simplicity, flexibility, scalability, and automation [88]. These advantages make black box models particularly suitable for complex systems where understanding the inner workings is challenging, or when dealing with diverse datasets across various domains. Their ability to handle large amounts of data effectively, relying on techniques like machine learning, makes them well-suited for big data scenarios. Additionally, black box models can provide valuable predictions or classifications without revealing sensitive or proprietary details, addressing privacy and security concerns. In cases of time and resource constraints, black box models offer quicker development and deployment [89]. While interpretability and transparency are essential in some contexts, when the primary goal is accurate predictions and outputs, black box modeling becomes a pragmatic choice, though a balanced approach, incorporating elements of white, gray, and black box methods, can be employed to meet specific needs.

In the context of thermal load prediction in residential buildings, having a one-size-fits-all model for all types of buildings is unrealistic as every building is unique and requires its specific set of

parameters. This is where the black-box model comes in handy, as it can be applied to a wide range of buildings, regardless of their specific characteristics, making it a generic solution [7]. Also, the widespread implementation of automated control systems and the Internet of Things in buildings has resulted in an abundance of data from measuring sensors, providing ample opportunities for developing black box models using Machine Learning (ML) algorithms, including linear regression, autoregressive exogenous (ARX), Support Vector Machines (SVM), extreme gradient boosting (XGBoost), and ANN models [90], [91]. Within the black-box category, choosing the appropriate algorithm is a challenging endeavor, with "Is there a stronger method than others?" as a frequently asked question.

Linear regression [92]–[94], ARX model [95]–[98], and more complicated methods like SVM [99]–[101] and XGBoost [102]–[105] are only a few statistical models and techniques used to predict future building loads. The other cutting-edge data-driven solution is the use of ANN. These networks are popular due to their striking features, such as adaptive learning, self-organization, real-time operations, generalization, stability and flexibility, and parallel processing. ANN has been widely recognized in the building energy domain as a promising approach due to its superior learning abilities and computational advantages. The Multilayer Perceptron (MLP) is a popular type of ANN that is made up of multiple layers of interconnected neurons. Unlike linear regression, which can only model linear relationships, MLP can handle both linear and nonlinear relationships by adding more hidden layers to the network. This allows MLPs to better capture the complex relationships in the data, leading to improved forecasting performance.

In addition to MLPs, the ANN domain includes various advanced ANN architectures such as Recurrent Neural Network (RNN) and Long Short-Term Memory (LSTM) networks. While RNN is widely used and effective for time series forecasting, it is susceptible to the risk of exploding and vanishing gradients and may have a limited capacity for storing features for long sequences [106]. LSTM overcomes these issues and has a more sophisticated structure than conventional RNNs, which allows it to store and access information over an extended period of time, making it more suitable for time series forecasting tasks. Some studies have highlighted the superior performance of LSTM over simple ANN for predicting a building's energy consumption, but this advantage comes at the cost of the increased computational burden [107]. Also, LSTMs require a large amount of training data to produce accurate results. If the training data is limited or noisy,

LSTMs may struggle to learn meaningful patterns. Therefore, the choice of ANN depends on the specific needs of the application [108], [109].

Creating an appropriate ANN model is a complex process that requires careful consideration of several critical steps. The early step involves selecting the most suitable features for the model, and there are various extraction algorithms available to achieve this, including the filter approach, wrapping method, embedding method [110]–[112], and so on. Choosing the right inputs is also a crucial aspect of feature selection, as having too many inputs can make the model overly complex and result in increased training time [113]. On the other hand, having too few inputs may lead to a model with inadequate performance. Therefore, it is essential to find a balance between the number of inputs and the model's performance. Having access to the inputs is also another aspect of feature selection that should be considered. Temporal features that are easily accessible, such as time of day, day of the week, and holidays, can be utilized in data-driven model training to improve the model's accuracy [92]. For example, in a predictive model for building energy consumption, the time of day, day of the week, and holidays can be useful in predicting peak demand periods. While these temporal features can be easy to obtain and process, there may be cases where additional sensors or algorithms are necessary to extract essential features for the model. These sensors and algorithms may come at an additional cost and require more time and effort to implement. For example, utilizing occupancy as a feature for model training can be beneficial. Alternative algorithms, room occupancy detectors, passive infrared sensors [114], or CO₂ sensors [115]–[117] can also provide valuable information about occupancy. Nonetheless, these methods can be expensive for the end user. Ideally, information should come from sensors that would be installed anyway, such as indoor temperature measurement and fluid temperatures in heating and cooling system points.

In this study the goal is to introduce a straightforward MLP model with a single hidden layer as an approach for predicting the thermal load of buildings. The objective was to develop a model that is fast, cost-effective, and adaptable, capable of accurate predictions even with limited data. To achieve this, complex data-driven models were deliberately avoided in favor of simpler alternatives. Instead, the study focused on selecting easy and straightforward inputs that could be universally applied to all building types without requiring detailed information about their physical characteristics. The chosen inputs consisted of commonly embedded sensors in buildings, eliminating the need for additional sensors. The MLP model was specifically designed for a

controller based on model predictive control, emphasizing the necessity of precise predictions for the building's thermal load. Overall, the proposed approach prioritized simplicity and practicality while still achieving accurate predictions.

In the following, the detailed procedure for constructing a self-adaptive ANN model to accurately predict thermal loads in buildings is explored. Subsequently, the model's effectiveness is showcased using a simulated building, emphasizing the potential of this innovative approach.

Before diving into the details, let's recall how the ANN training process works. ANNs are trained using several input and output data pairs that correspond to the input features and output targets. The ANN architecture has a set of trainable parameters which are continuously adjusted in the training phase to minimize/maximize a particular performance indicator, also known as the loss function. In this case, features and targets are snapshots of measured physical quantities observed over a certain period of time. This training process enables the ANN to learn and improve its predictions continuously. The end result is a highly adaptable and versatile model that can be used for energy planning and management in the building.

3.1.1 Case study

The dataset used in this study was generated by simulating the real building in TRNSYS and saving the numerical data in a Comma-Separated Values (CSV) file. The building stratigraphy was already known from the EnergyMatching project (European Union's Horizon 2020 research and innovation program, grant agreement N° 768766). The TRNSYS model was utilized to generate a meticulously prepared dataset that accurately represents the behavior of an existing building subjected to climate conditions typical of Bolzano, Italy [118].

The dataset encompasses all aspects of the building, with a particular emphasis on the HVAC control system. It consists of 65 columns that represent the most crucial information related to the building's thermal behavior and energy consumption. In terms of size, the dataset contains a significant amount of information due to the one-year simulation duration and the 5-minute sampling interval.

The building, as depicted in Figure 3-1, is a small apartment with high insulation levels and a floor area of 62.6 m². The building's annual energy consumption stands at around 50 kWh/m². For space heating, all rooms except the bathroom and kitchen are equipped with a radiant floor heating and cooling system, each with its own dedicated thermostat for individual zones.

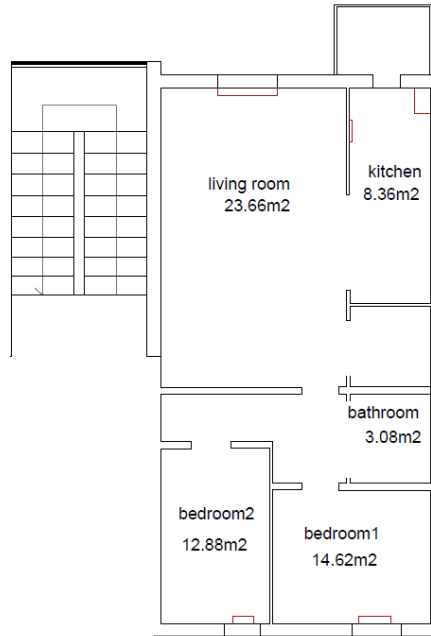


Figure 3-1. The layout of the building in the case study

3.1.2 Input variable selection

Selecting appropriate input features is fundamental to building an ANN. The process of choosing the right features is a challenging task and requires a basic knowledge of the parameters capable of influencing the system. A general principle is to pick the number of features that can adequately model the system dynamics without putting excessive computational burden. To this end, some statistical-based feature selection methods evaluate the relation between input (features) and output (target) variables. These techniques attempt to concentrate on reducing redundant or unhelpful variables and selecting the most meaningful features. The relationship between the input and target variables depends on the variable types (numerical/categorical), leading to different statistical assessment (regression/classification) methods. In this case, the types of variables we encounter are numerical; therefore, we resort to calculating Pearson's correlation coefficient (PCC) to assess the input and target variable relationship. PCC measures the linear correlation ($\rho(X, Y)$) between two variables X and Y using the equation (3.1).

$$\rho(X, Y) = \frac{\mathbb{E}[(X - \mu_X)(Y - \mu_Y)]}{\sigma_X \sigma_Y} \quad 3.1)$$

Where \mathbb{E} is the expected value, μ_X and μ_Y are the mean value of variables X and Y respectively, and σ_X and σ_Y are the standard deviation of variables X and Y , respectively. Based on the outputs of PCC, selected features are shown in Figure 3-2.

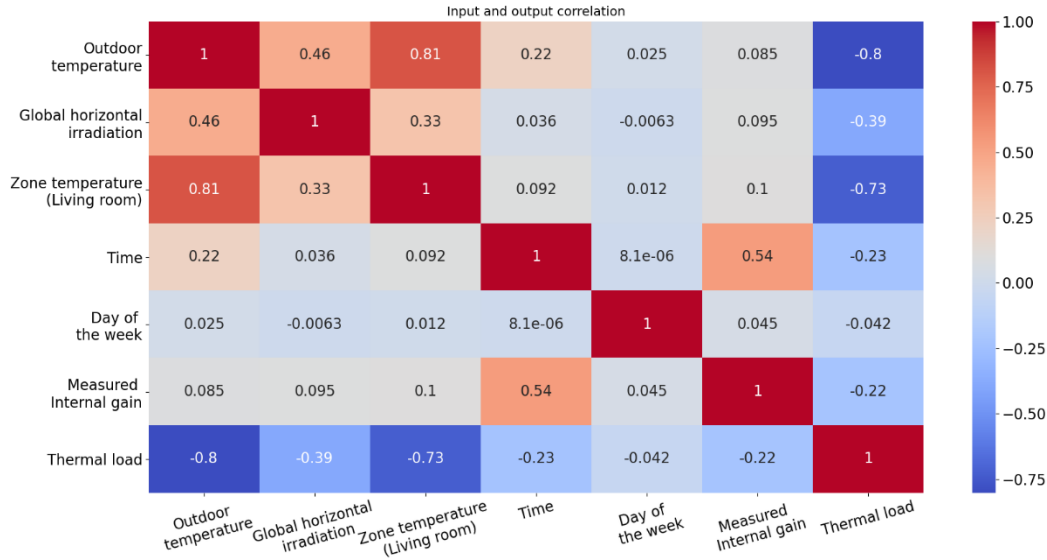


Figure 3-2. Correlation Heatmap showing the Relationship between Inputs and Thermal Load

3.1.3 ANN design and configuration

In this study, various ANN structures were considered, with the goal of selecting the most appropriate one based on the specific needs of the task at hand. While multiple structures were initially explored, the MLP was ultimately found to be the most effective option for the specific requirements of this study. While other structures may have had the potential to achieve higher accuracy or faster speeds with further optimization, the simplicity and efficiency of the MLP were essential for meeting the specific requirements of this study.

The Multilayer Perceptron (MLP) is one of the most used and versatile ANN architectures. MLPs are widely regarded as a powerful tool for solving complex nonlinear problems, including classification and prediction tasks, due to their ability to learn and represent complex nonlinear relationships between input and output data. One of the key advantages of MLPs is their flexibility and adaptability. They can be trained on a wide range of input and output data types, including continuous, discrete, and binary data, and can be used for both supervised and unsupervised learning [119]. Another advantage of MLPs is their ability to incorporate prior knowledge and expert input into the learning process. This makes it possible to tailor the network architecture and learning algorithm to specific problem domains and to optimize the network's performance based on domain-specific knowledge [120].

The MLP model that was chosen for the study has six input features, a hidden layer with 16 neurons, and only one output feature. In order to address the temporal dependence of the problem

at hand, it was deemed necessary to include not only the parameters with the highest correlation but also the day of the week (D_w) and time of the day (t) as input features. The inclusion of D_w and t as input features in the MLP model is significant for capturing the cyclic and diurnal patterns in thermal load behavior. D_w captures differences in thermal load across weekdays and weekends, while t accounts for variations throughout the day due to factors like outdoor temperature and human activities. Including both features allows the model to account for weekly and daily variations in thermal load without the need for additional sensors. D_w and t can be easily derived from available data sources such as timestamps or system clocks.

In the process of developing the ANN model, experiments were conducted to determine the optimal number of neurons in the hidden layer. Several trials were performed with varying numbers of neurons, ranging from a small number to a larger one. Through these experiments, it was found that using 16 neurons in the hidden layer proved to be the most effective choice, as it yielded the best results. Besides, the choice of activation function for the hidden layer was considered. After evaluating different options, the Rectified Linear Unit (ReLU) activation function was selected as the optimal choice. This decision was made based on its ability to improve the model's performance and accuracy, as well as its computation efficiency compared to other activation functions. As the activation function for the output layer, a linear activation was considered in order to produce continuous output values that represent the predicted thermal load of the building. This choice was made to ensure that the output is directly proportional to the input, making it easier to interpret and integrate with the MPC approach used in the controller. Figure. 10 illustrates the architecture of the proposed ANN model.

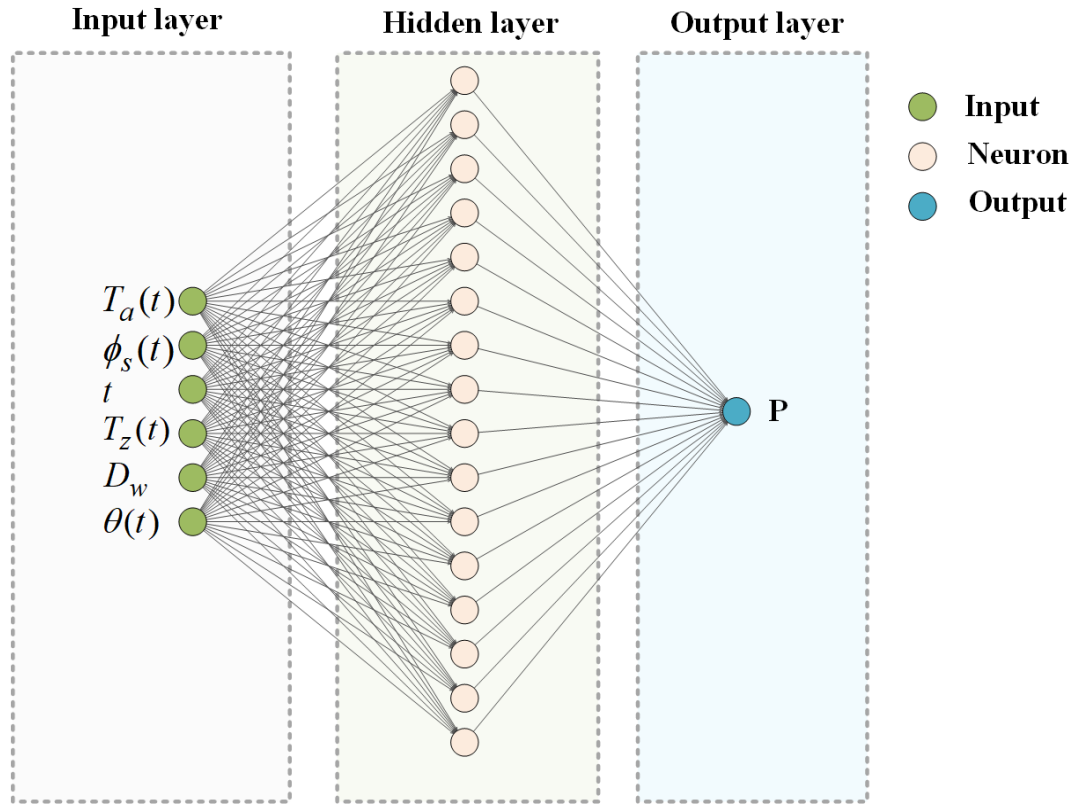


Figure 3-3. Structure of proposed ANN model for load prediction

3.1.4 Technical barriers

In order for the ANN to effectively predict the thermal load, it must have access to the future values of its input features. Therefore, the future input feature values can be obtained through forecasting or made available through other means. In this work, the meteorological data (T_a and ϕ_s) and integral gains (θ) are sourced from TRNSYS, therefore, assuming to have a perfect prediction of outdoor conditions and internal gains. It should be noted that the term "internal gain" refers explicitly to the measured internal gains associated with lighting and electrical appliances that can be easily quantified using electricity meters. Measuring internal gain in the real world is challenging, often requiring models or calculations. To strike a balance between accuracy and practicality, we simplified the model and focused on electrical measurable sources.

As we can see in Figure 3-3, the zone temperature is one of the input features for the thermal load model, implying that it must also be predicted. It turns out that the future values of the zone temperature can be forecasted with satisfying accuracy by making use of a second ANN model where the thermal load is an input feature as they are interdependent. The task of the second ANN model is to predict the zone temperature (T_z). This model requires similar features to those of the

thermal load model with additional features representative of the thermal load and zone temperature at the previous time step. The zone temperature model can be formulated as equation (3.2).

$$T_z(t) = f(T_a(t), \phi_s(t), t, D_w, \theta(t), P(t), T_z(t - 1)) \quad (3.2)$$

The tie induced by the fact that each model output is also an input of the other is solved by connecting the two models in a feedback loop. Figure 3-4 shows the final model structure.

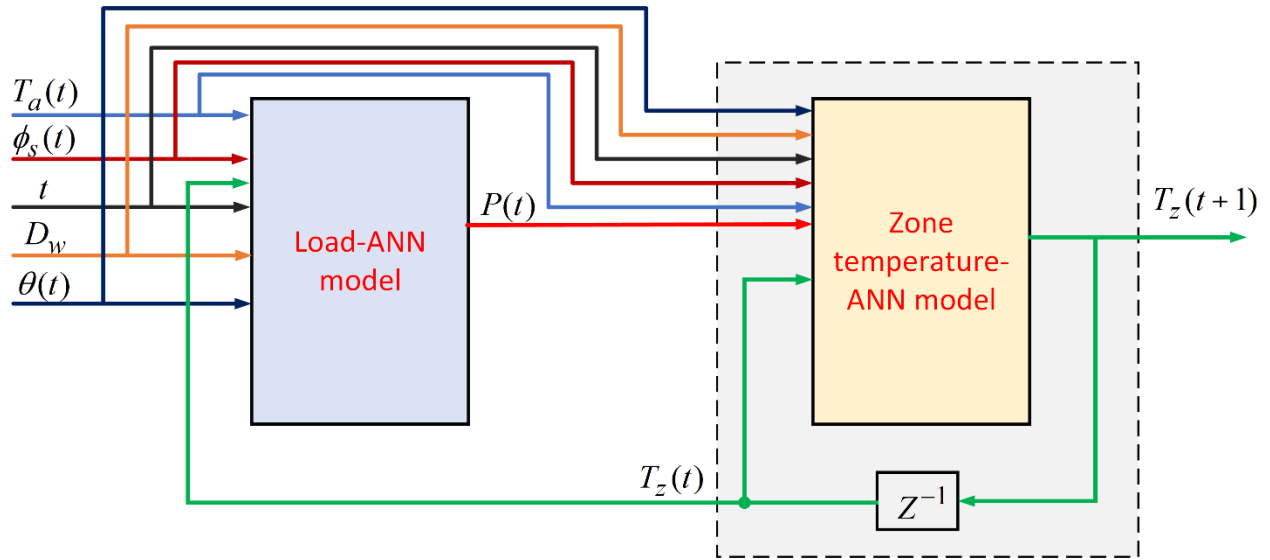


Figure 3-4. Identified model for load (and zone temperature) prediction.

3.1.5 Model enhancement

The mathematical details of the proposed model's implementation are discussed in this section. The model is designed to make hourly predictions over a 24-hour horizon continuously. The model is based on a state-space model that can approximate the input-output relation seen in the data, and this family of functions includes all networks arising from the combination of possible neuronal units, connections, activation functions, and weights. The extended state vector is introduced to include the recent past evolution of state and input variables, and a selector is used to reduce the network's complexity by selecting a subset of extended states to become features fed to the ANN core. We investigated the optimal size of training datasets for a 5-minute time step model and designed a method for weight initialization. The model is trained every day at midnight using the most recent data and then used to make predictions for the next 24 hours. To evaluate the accuracy of the proposed model, various performance metrics were utilized.

3.1.6 Continuous training model

Determining the behavior of a building in response to variations in its boundary and internal conditions can be seen as a (dynamic) system identification task. More specifically, since a real building can show both nonlinear and time-varying (NLTV) behaviors, we are dealing with identifying NLTV systems. Such systems can theoretically be formulated like equation (3.3) as NLTV state-space models.

$$\begin{cases} \mathbf{x}(t+1) = \mathbf{f}(\mathbf{x}(t), \mathbf{u}(t), t) \\ \mathbf{y}(t) = \mathbf{g}(\mathbf{x}(t), \mathbf{u}(t), t) \end{cases} \quad 3.3)$$

In this formula, \mathbf{f} and \mathbf{g} are vector values functions, while $\mathbf{u}(t) \in \mathbb{R}^m$, $\mathbf{x}(t) \in \mathbb{R}^n$ and $\mathbf{y}(t) \in \mathbb{R}^p$ represent the input, state, and output vectors at time t , respectively. In other words, \mathbf{f} represents n scalar functions of $n + m + 1$ (scalar) variables while \mathbf{g} represents p scalar functions of $n + m + 1$ variables. \mathbf{f} is called the state update function, while \mathbf{g} is called the output function. The system identification task consists in determining the state update and output function that best approximates the input-output relation seen in the data in a certain family of functions. In this work, we performed the system identification task using ANNs, therefore the family of functions we are referring to is the family of all the networks arising from the combination of possible neuronal units, their connections, activation functions, and weights.

In this context, due to the use of ANN, we found it helpful to explicitly include the recent past evolution of state and input variables in the mathematical formulation, leading to a modified version of equation (3.3) to read as equation (3.4).

$$\begin{cases} \mathbf{x}(t+1) = \mathbf{f}(\mathbf{x}(t - q_X), \dots, \mathbf{x}(t - 1), \mathbf{x}(t), \mathbf{u}(t - q_U), \dots, \mathbf{u}(t - 1), \mathbf{u}(t), t) \\ \mathbf{y}(t) = \mathbf{g}(\mathbf{x}(t - q_X), \dots, \mathbf{x}(t - 1), \mathbf{x}(t), \mathbf{u}(t - q_U), \dots, \mathbf{u}(t - 1), \mathbf{u}(t), t) \end{cases} \quad 3.4)$$

Here, q_X is the number of past samples of the state variables, and q_U is the number of past samples of the input variables. Note that although in equation (3.4) we used the same symbols as in equation (3.3), the symbols denote different state update and output functions. The total number of scalar arguments of the two functions is $n(q_X + 1) + m(q_U + 1) + 1$, including the time dependence.

It is easy to show by introducing the extended state vector $\boldsymbol{\xi}(t)$,

$$\boldsymbol{\xi}(t) = [\mathbf{x}(t - q_X); \dots; \mathbf{x}(t - 1); \mathbf{x}(t); \mathbf{u}(t - q_U); \dots; \mathbf{u}(t - 1)] \quad 3.5)$$

that the modification does not change the structure of the formulation, as (3.4) can be cast in the same form as equation (3.5),

$$\begin{cases} \boldsymbol{\xi}(t+1) = \boldsymbol{\varphi}(\boldsymbol{\xi}(t), \mathbf{u}(t), t) \\ \mathbf{y}(t) = \boldsymbol{\gamma}(\boldsymbol{\xi}(t), \mathbf{u}(t), t) \end{cases} \quad 3.6)$$

where $\boldsymbol{\varphi}: \mathbb{R}^{n(q_X+1)+mq_U} \times \mathbb{R}^m \times \mathbb{R} \rightarrow \mathbb{R}^{n(q_X+1)+mq_U}$ is the new (extended-)state update function and $\boldsymbol{\gamma}: \mathbb{R}^{n(q_X+1)+mq_U} \times \mathbb{R}^m \times \mathbb{R} \rightarrow \mathbb{R}^p$ is the new output function.

A diagram representing the relationship between extended state $\boldsymbol{\xi}(t)$, state at the next moment $\boldsymbol{x}(t+1)$ and input $\boldsymbol{u}(t)$ is given in Figure 3-5, using two vector delay lines (VDL), one related to the state variables and the other to the input variables. The two VDLs consist of several vectorial one-step delay blocks (denoted by z^{-1}). As represented in Figure 3-6, a vector delay block is composed of various scalar one-step delay elements (also denoted by z^{-1}).

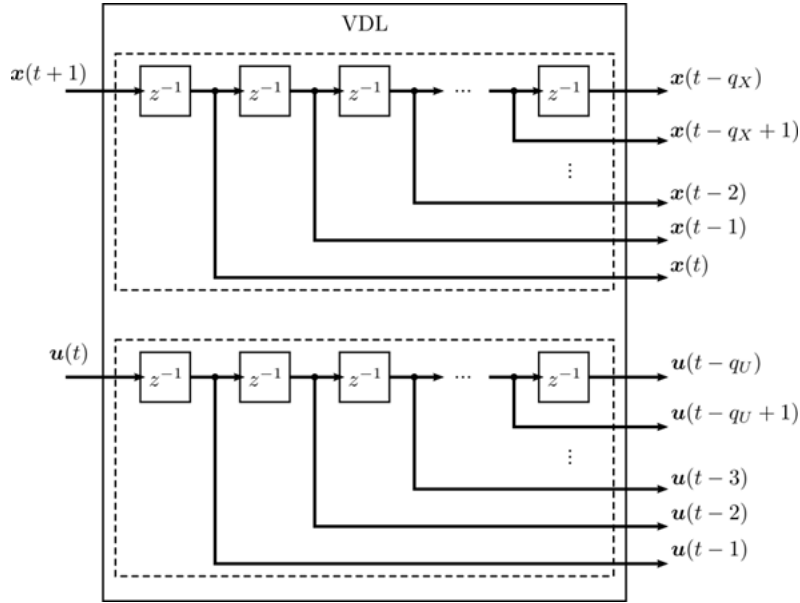


Figure 3-5. Graphical representation of the construction of the extended state $\boldsymbol{\xi}(t)$ carried out by the VDL block.

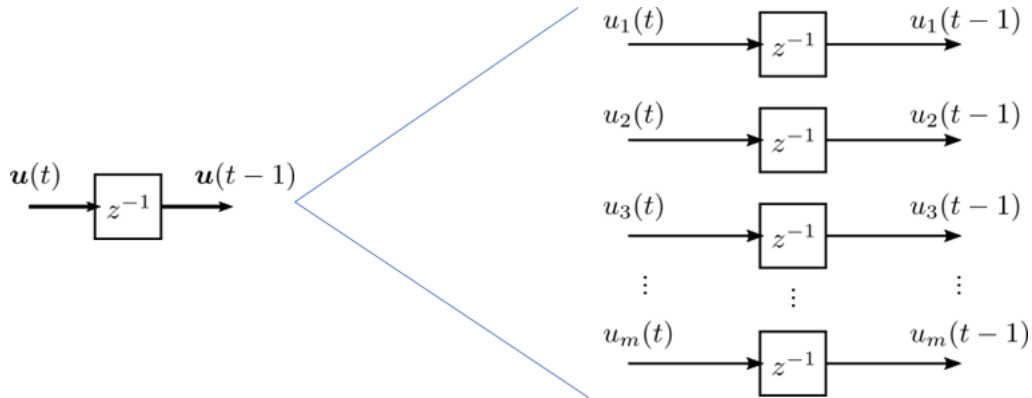


Figure 3-6. Illustration of the vector representation in the case of the delay block.

Decimation, or down-sampling, is the process of reducing a signal sample rate. Decimation decreases the sampling rate of the inputs by an integer factor by periodically selecting one sample out of N samples. To ease the system identification with neural networks, we consider a different

structural feature regarding the reduction of the extended states. The reasons for introducing this feature in the model are outlined below. In certain conditions, it may be helpful or even necessary to use relatively high values of the parameters q_X and q_U in order to capture "ancient" samples (like those of 24 hours before). However, the fact that very old samples are needed does not mean that feeding the ANN element with the entire record of past samples (including the present) is the most appropriate choice. To provide the ANN element with a reduced number of samples, we introduce the selector $\mathbf{\Pi}: \mathbb{R}^{n(q_X+1)+mq_U} \rightarrow \mathbb{R}^{n_f}$, allowing, in general, to select a subset of extended states to become features to be fed to the ANN core.

In this way, $\tilde{\mathbf{f}}$ and $\tilde{\mathbf{g}}$, the final state update and output functions are obtained. We remark that reducing the number of inputs to an ANN can reduce the network's complexity and consequently increase both the learning speed and the evaluation speed, especially in the case of shallow networks. In theoretical developments, $\mathbf{\Pi}$ can be assumed to be a full-rank matrix with $n_f: \mathbb{N}$ rows and $n(q_X + 1) + mq_U$ columns, consisting of only numbers one and zero and having precisely one number 1 per row. The reduced (extended-)state $\mathbf{\Pi}\xi(t)$ and the current input $\mathbf{u}(t)$ concur to form the set of features fed to the neural network, which aims to produce certain output targets. Briefly, the structure of the model is written like equation (3.7).

$$\begin{cases} \mathbf{x}(t + 1) &= \tilde{\mathbf{f}}(\mathbf{\Pi}\xi(t), \mathbf{u}(t), t) \\ \mathbf{y}(t) &= \tilde{\mathbf{g}}(\mathbf{\Pi}\xi(t), \mathbf{u}(t), t) \end{cases} \quad 3.7$$

This description using mathematical symbols can be illustrated in Figure 3-7. Figure 3-7 highlights the fundamental structural elements of the functional block called ANNModel: the double VDL, the selector of the extended-state $\mathbf{\Pi}$, the ANN block and the feedback loop ($\mathbf{x}(t + 1)$). Both the load model and the zone temperature model are instances of this ANN-model functional block. The load model has no state variables ($\mathbf{x}(t)$ is empty, $n = 0$) while the zone temperature model has no outputs apart from its state variable ($\mathbf{y}(t)$ is empty, $p = 0$). Both models however have an extended state because both make use of past inputs. Although the model allows for a flexible method to reduce the extended state to create the features, in this works we used only the decimation approach.

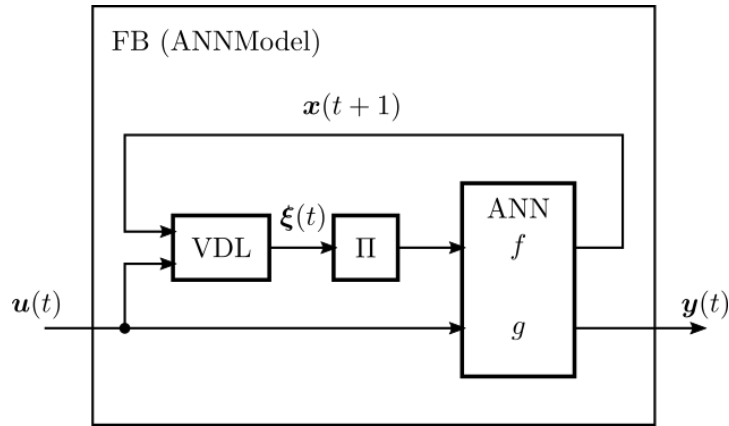


Figure 3-7. Graphical representation of a functional block (FB) implemented by the neural network.

3.1.7 Length of the dataset for training and validating

The datasets for training, validating, and testing the proposed ANN model were generated from yearly simulations of the TRNSYS model. These datasets are referred to as TRNSYS datasets. In the deployable implementation, as it is not possible to embed meaningful data for training and validating before the installation of the system, the model requires some time to gather experimental data before it can begin training and making predictions. The size of the dataset is of paramount importance, as having the right amount of data can reduce computational time, while not having enough data can result in the model not achieving acceptable performance. Empirical processes and experiments are a way of answering the question of how much data is needed for a well-performing model, as the answer depends on the type of problem. Therefore, based on the TRNSYS dataset, the size of the data required for the model to be well-trained and proficient was investigated. It was discovered that the learning of the model is significantly impacted by days with frequent zero thermal loads. Consequently, it would be better not to use zero days for training. The size of the training dataset was also explored. As previously stated, a model that can be trained effectively with less data has a competitive advantage. The results of several experiments showed that on a 5-minute time step model, 14 days of recorded data are sufficient to achieve acceptable performance. Utmost care has been taken to ensure that new data is consistently included in the training dataset while the oldest samples are left for validation. This approach allows for a more accurate and up-to-date model. Additionally, it is important to note that the size of the dataset may vary depending on the complexity of the problem and the type of model used. Thus, it is important to experiment and evaluate the performance of the model with different dataset sizes to find the optimal size for the specific problem.

3.1.8 Learning through weight adjustments

Proper weight initialization is a crucial step in developing a neural network model. The optimization approach used in neural network modeling, stochastic gradient descent, gradually alters network weights to minimize a loss function, ultimately resulting in a set of weights that can generate accurate predictions. However, this optimization process needs a starting point, which is where weight initialization comes into play. Weight initialization is the process of assigning initial values to the weights of a neural network, often small random values. This serves as the starting point for the optimization process [121]. Choosing the appropriate weight initialization strategy is essential for the network to converge and reach a global minimum of the loss function. For example, it has been shown that using appropriate weight initialization techniques such as Xavier initialization [122] or He initialization [123] can lead to faster convergence and better performance of the model. The correct weight initialization can help to overcome local optima and help the model to converge faster. Therefore, weight initialization is a crucial step in developing a neural network model, and it should be carefully considered in the model design process.

In this study, the proposed model is designed in a way to be retrained every 24 hours and make predictions hourly over a horizon of 24 hours. This process is repeated daily, for example, at midnight. Each training starts with an initial set of weights. The weights can be set at random or with the previous best gains. Starting from the steps of the previous weight rather than starting at random can improve convergence speed. It might be interesting in the future to combine the two options, allowing for "blur" only a portion of your previous gains. In addition to that, the applied weights for the next 24 hours after the retraining are a convex combination of the most recent optimal gains and the previous optimal gains. Equation (3.8) shows precisely how the weights are manipulated. The factor δ is a floating number in the $[0,1]$ range. One entirely discards the previous weights, whereas zero dismisses the new ones (rendering the model totally non-adaptive). Figure 3-8 represents the structure of weight initialization and weight selection in the proposed ANN model. Also, the role of a switch is formulated in equation (3.9).

$$\hat{W}_i = (1 - \delta)W_{i-1} + \delta W_i \quad \delta \in [0, 1] \quad 3.8$$

$$\begin{cases} \delta = 1, & s = 0 \\ \delta \in [0, 1], & s = 1 \end{cases} \quad 3.9$$

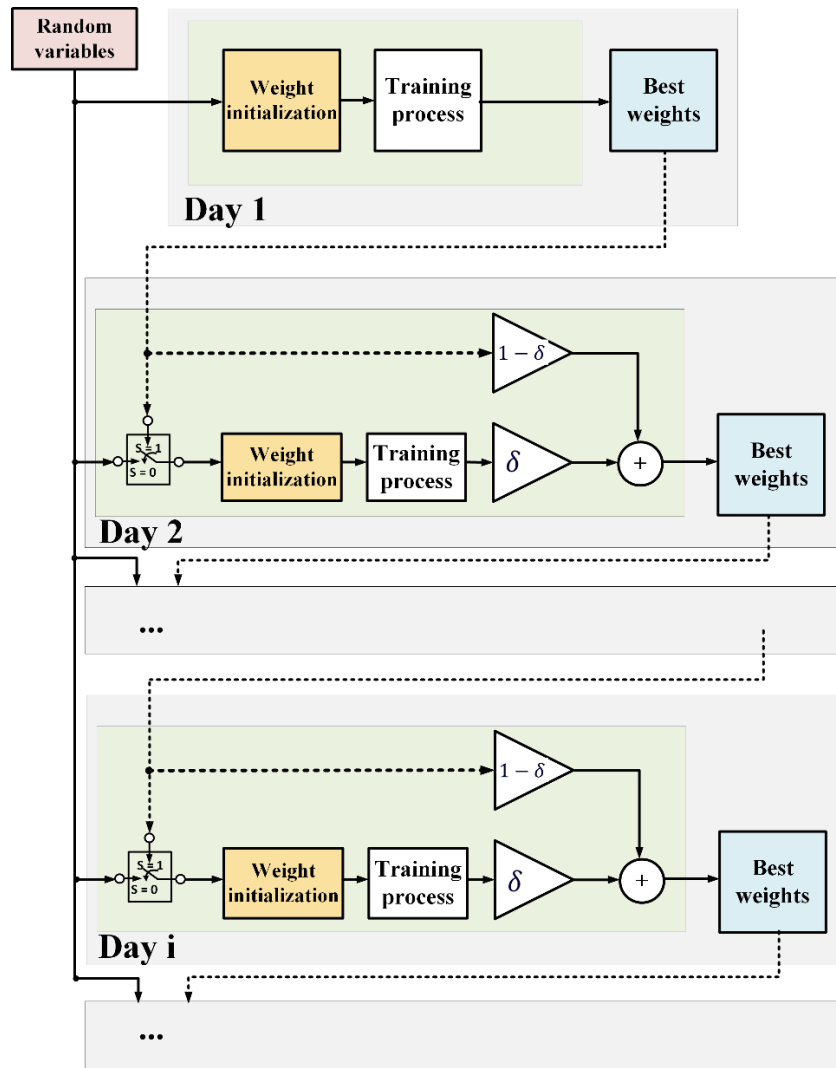


Figure 3-8. The structure of the proposed idea regarding weights in ANN

3.1.9 Resetting state

In this study, the proposed ANN model was designed to predict thermal load and indoor temperature for the following 24 hours. Typically, models can predict the first few hours with high accuracy, but their accuracy decreases over time, leading to diverging predictions. However, since in real-world scenarios, continuous access to sensor data is available, the proposed model is able to update its predictions more frequently, every hour. This is achieved by updating the internal state of the model with the most recent information and then running a 24-hour simulation. It is important to note that the process of training the model and making predictions are distinct. The model is trained every day at midnight, using the most recent data available. After the training process is complete, the trained model is used to make predictions every hour for the next 24 hours.

3.1.10 Key performance indicators (KPIs)

To evaluate the accuracy of the proposed model, several key performance indicators (KPIs) were used. One of the most widely used error metrics in the regression problem is the mean square error (MSE). MSE measures the average squared discrepancies between a dataset's predicted and actual target values. Root Mean Square Error (RMSE) is an extension of the mean squared error [124], and it is a commonly used measure of the difference between values predicted by a model or an estimator and the true values. An important feature of RMSE is that the units of the RMSE are the same as the original units of the target value that is being predicted. Another commonly used metric is mean bias error (MBE). MBE is a measure of the long-term performance of a model, as it indicates the average difference between the predicted and actual values. A positive number indicates that the estimated values are typically overestimated and vice versa [125]. To make the MBE findings comparable, the normalized mean bias error (NMBE) index is used, which normalizes the MBE index by dividing it by the mean of the measured values [126]. This allows for a more accurate comparison of the performance of the model across different datasets and scenarios.

$$MSE = \frac{\sum_{i=1}^N (\hat{y}_i - y_i)^2}{N} \quad 3.10)$$

$$RMSE = \sqrt{MSE} \quad 3.11)$$

$$MBE = \frac{\sum_{i=1}^N (\hat{y}_i - y_i)}{N} \quad 3.12)$$

$$NMBE = \frac{\sum_{i=1}^N (\hat{y}_i - y_i)}{(N - 1)\bar{y}} \times 100 \quad 3.13)$$

In equations (3.10) to (3.13), N is the number of samples, \hat{y}_i is the predicted value, y_i is the actual value and \bar{y} is the average of actual values.

3.1.11 Method assessment

This section presents the simulation results that evaluate the effectiveness of the suggested model for thermal load prediction. The proposed ANN model was implemented in Python on a laptop with an i7 2.3 GHz CPU and 32 GB memory. It is a versatile model capable of predicting the thermal load of a building zone, such as an apartment, throughout the year. Regardless of the building's size and location, the model requires two weeks of performance data to be collected. Since it is a black-box model, it does not have pre-existing data in its repository, highlighting the

importance of data collection as a crucial step. Once the data is gathered, the model can generate predictions for control purposes. It produces hourly predictions and self-trains every 24 hours, replacing old data with newly recorded data. The training and validation period for the model spans two weeks. In the prediction model, for each time step, the model examines the data from the past 6 hours and generates a prediction.

Figure 3-9 provides a detailed illustration of the model performance during the winter season. In the beginning, the model is trained on data spanning from the 17th to the 30th of November. It was deployed for prediction for the next seven days. During the winter, the thermostat hysteresis is set between 20.75 and 21.25 °C. The figure is divided into three sections. The initial section gives a summary of the ambient temperature (T_a) and the relative global horizontal irradiance (ϕ_s). In the following section, the temperature of the zone is presented, showcasing both the actual values and the model's predicted values. The actual temperature is represented by a black line, while the model's hourly predictions are distinguished using various colors. Lastly, the third section displays the thermal load of the living room, depicting both the ground truth and the predicted values in a similar format.

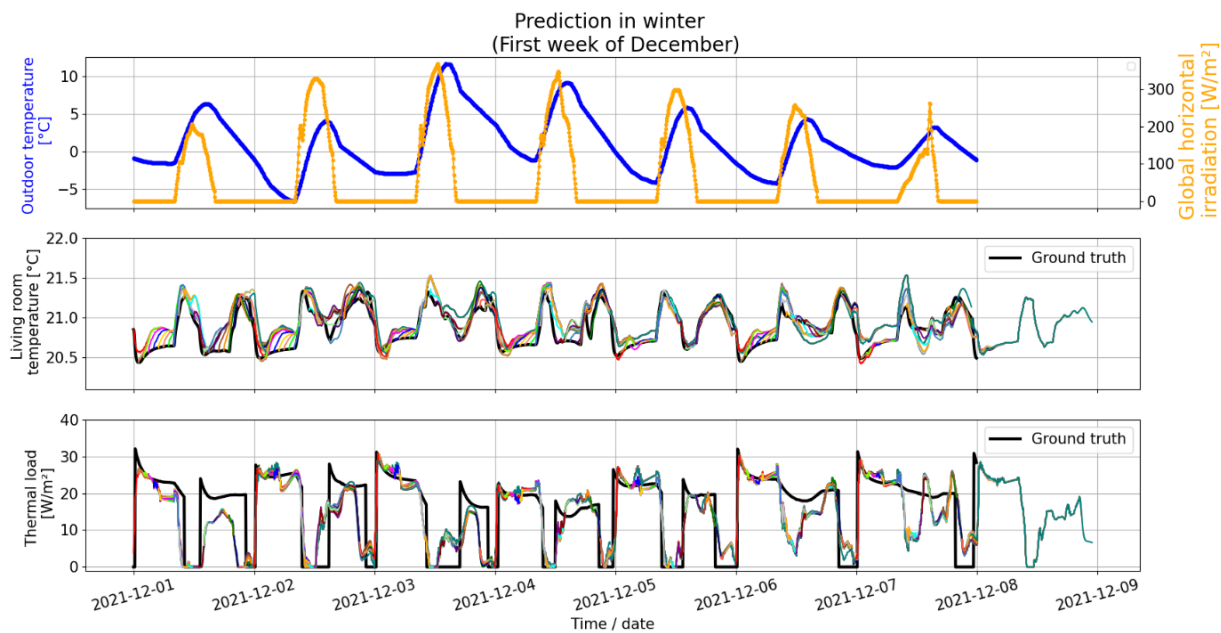
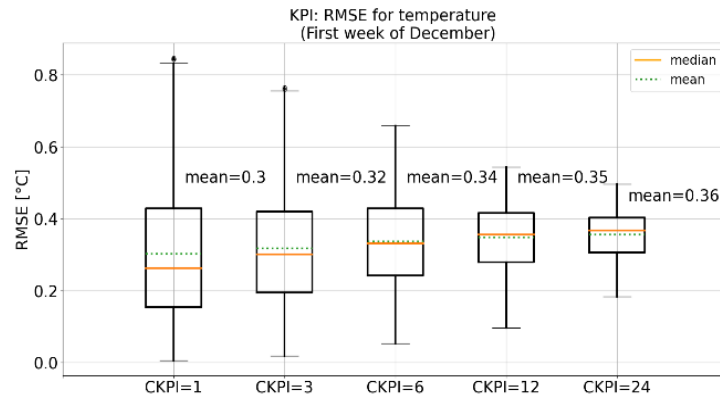


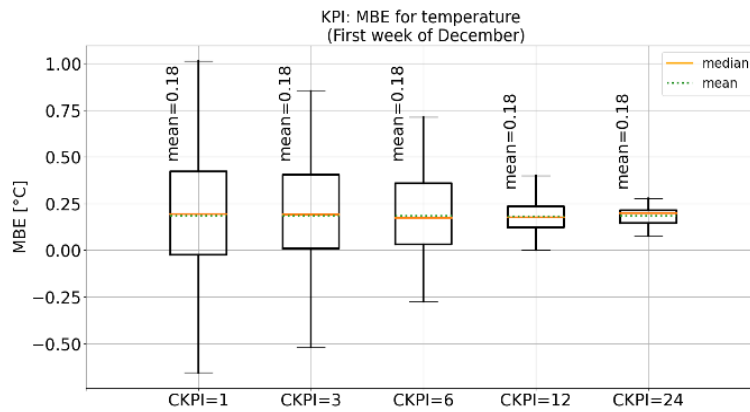
Figure 3-9. Living room's temperature and thermal load prediction for the first week of December

Figure 3-10 (a) and (b) show the RMSE and MBE, which are used to assess the accuracy of the zone-temperature ANN model. Typically, KPIs are calculated in the literature based on the

prediction horizon, which means that if the prediction horizon is 24 hours, all points of ground truth and forecast are considered, and the relative KPI is generated. As previously stated, models can generally accurately anticipate the first several hours. Nonetheless, their accuracy goes down over time, making it critical to know the accuracy at various intervals. To that purpose, computed KPI (CKPI) was established to calculate error hourly and over 3, 6, 12, and 24 hours. Figure 3-10 (a) depicts the RMSE for temperature in different CKPIs where the mean of all errors is around 0.3 °C. As can be seen, when the CKPI is computed at a 24-hour interval, the error range is narrow, but when the CKPI is computed at a 1-hour interval, the error range widens. Figure 3-10 (b) shows the range of the temperature bias error. Like RMSE, the error distribution varies depending on the data aggregation; for a 24-hour period, the error range is lower than for a shorter period. The mean of MBE for all CKPIs is 0.18 °C. To enhance the clarity of the data visualization, outliers have been deleted from all the box plots. This was done to provide a clearer view of the box and improve the overall visual representation of the data.



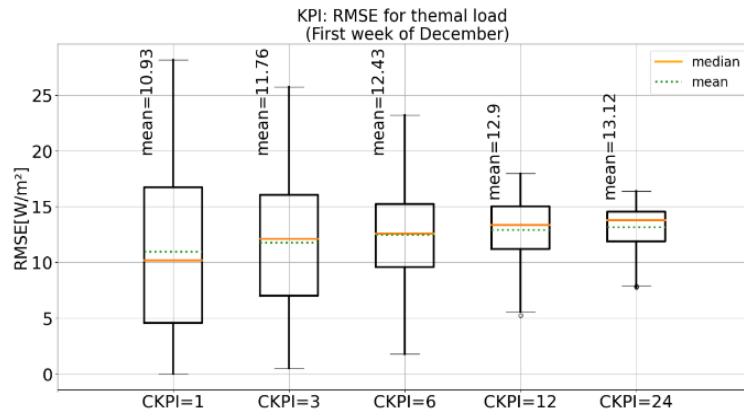
(a)



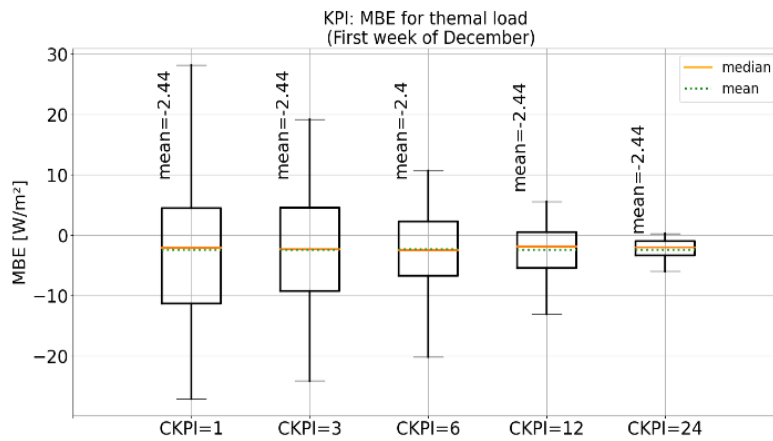
(b)

Figure 3-10. RMSE (a) and MBE (b) for temperature in the winter

Figure 3-11 (a) and (b) show the RMSE and MBE of the thermal load model. The average of RMSE and MBE is about 12 and -2.4 W/m^2 , respectively.



(a)



(b)

Figure 3-11. RMSE (a) and MSE (b) of thermal load in the winter

The NMBE of the thermal load is shown in Figure 3-12. According to Eq. (3.13) we are dealing with \bar{y} in the denominator and as it observed from Figure 3-12 in some intervals \bar{y} is zero. While the amount of CKPI is less than 6, \bar{y} sometimes will be zero, resulting in the amount of error being infinite. To address this problem, the mean period (MP) is introduced, which considers the average of the next 6, 12, and 24 hours. The range of the NMBE will be reduced concurrent with increasing CKPI.

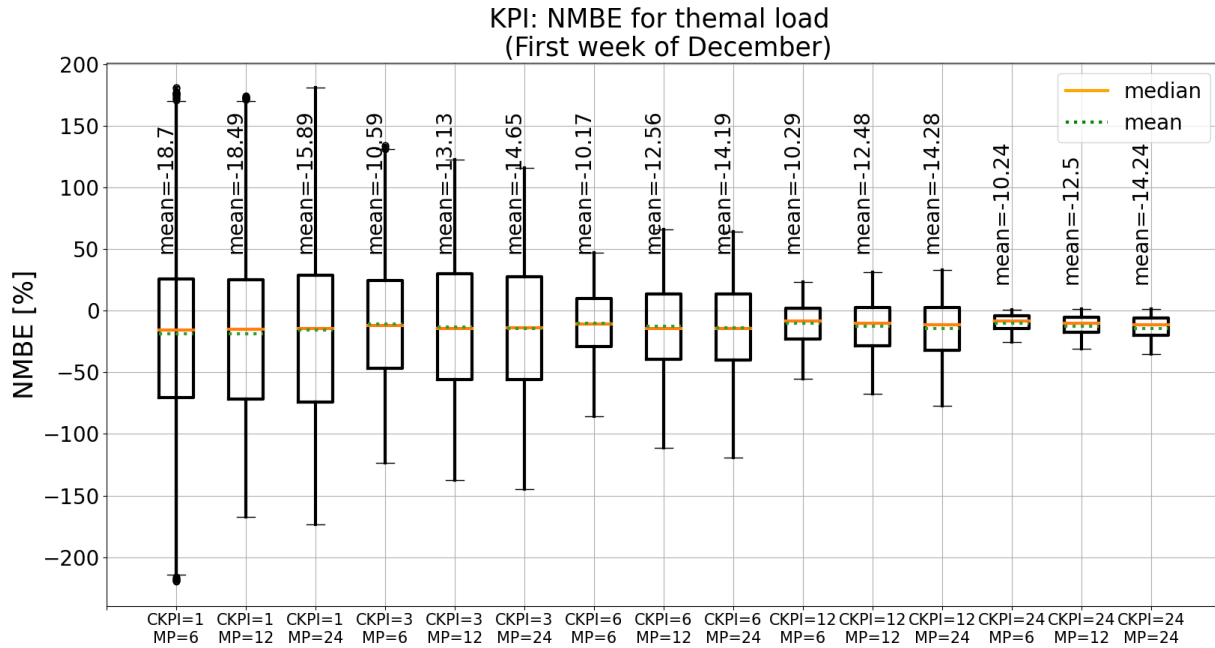


Figure 3-12. NMBE for thermal load

Figure 3-13 represents the results of the model during summer. The model has been trained by data from the 17th of June to the 30th of June and started predicting the 1st to the 7th of July. During the summer, the thermostat hysteresis is set between 24.5 and 25.5 °C. The cooling load is considered here as a negative value.

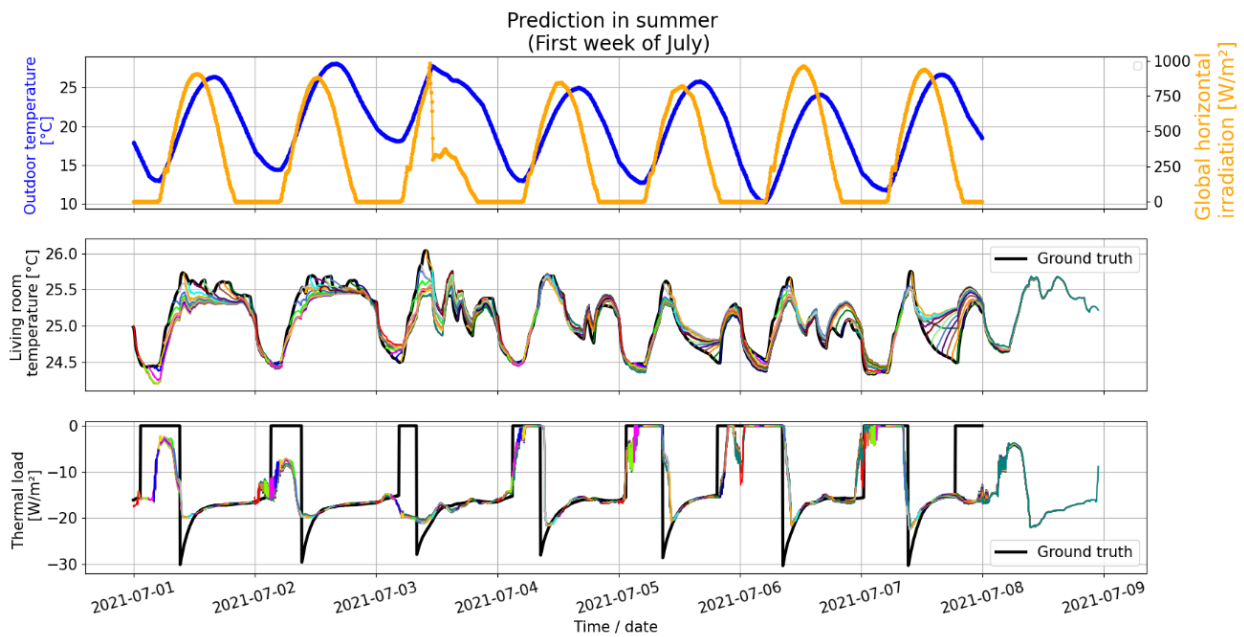


Figure 3-13. Living room's temperature and thermal load prediction for the first week of July

Figure 3-14 (a) shows the RMSE of the temperature model in summer. In all CKPIs, the average and median of RMSE is less than 1°C. Also, as presented in Figure 3-14 (b), the average MBE in summer is around 0.2 °C.

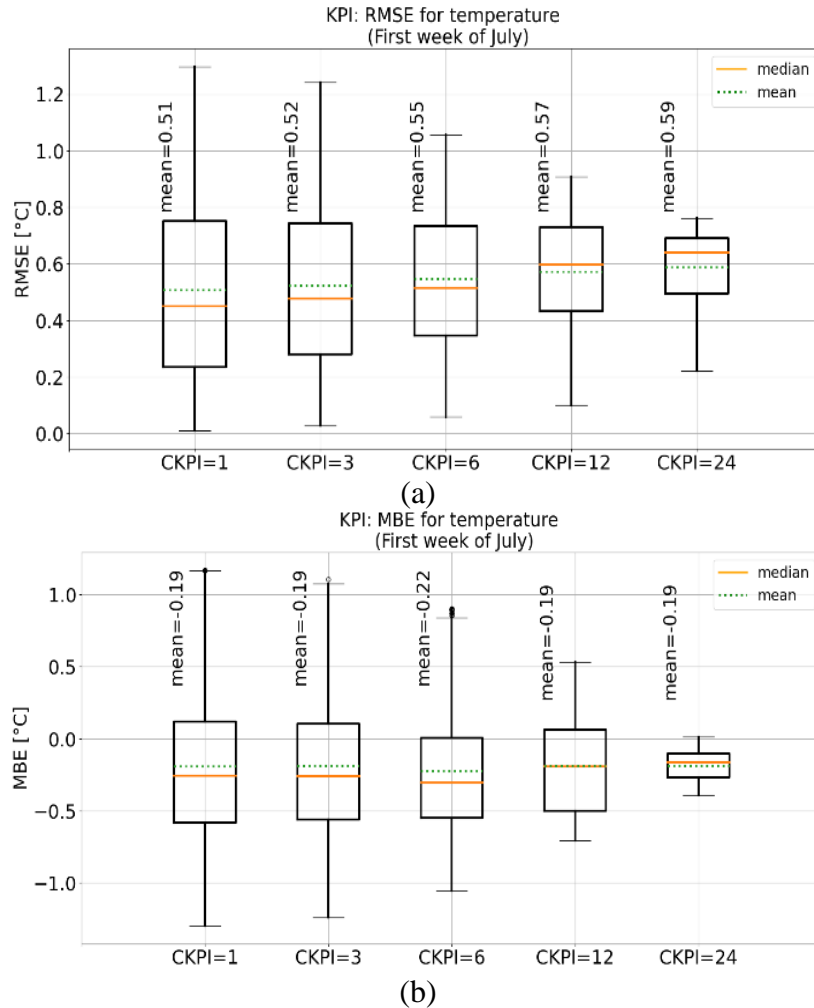


Figure 3-14. RMSE (a) and MBE (b) for temperature in the summer

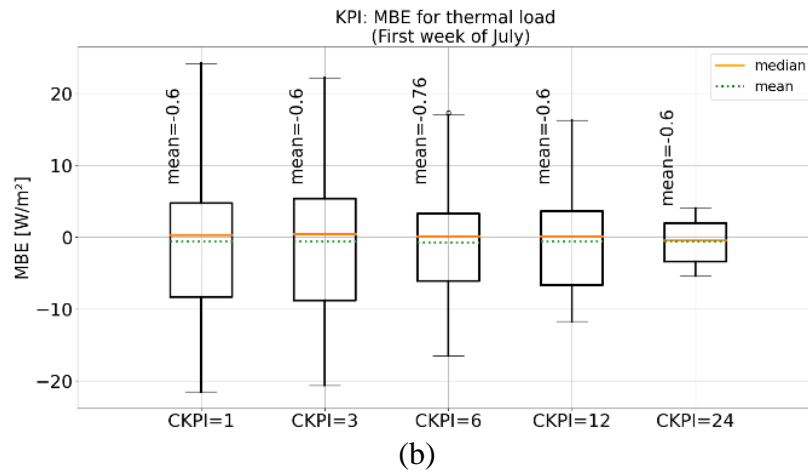
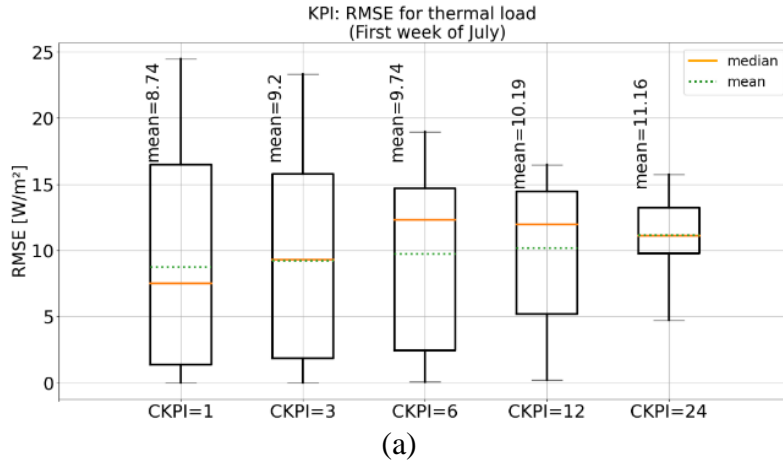


Figure 3-15. RMSE (a) and MBE (b) for thermal load in the summer

In Figure 3-15 (a) and (b), the average of RMSE and MBE for thermal load is about 10 and -0.6 W/m^2 , respectively. Based on Figure 3-12, same as winter, the average of ground truth in some intervals is zero, which can result in a high amount of NMBE. Especially once MP is 6, since the value of \bar{y} is close to zero, as it observed from Figure 3-16 in some period of time (between 5th to 7th of July), the range of error increased substantially.

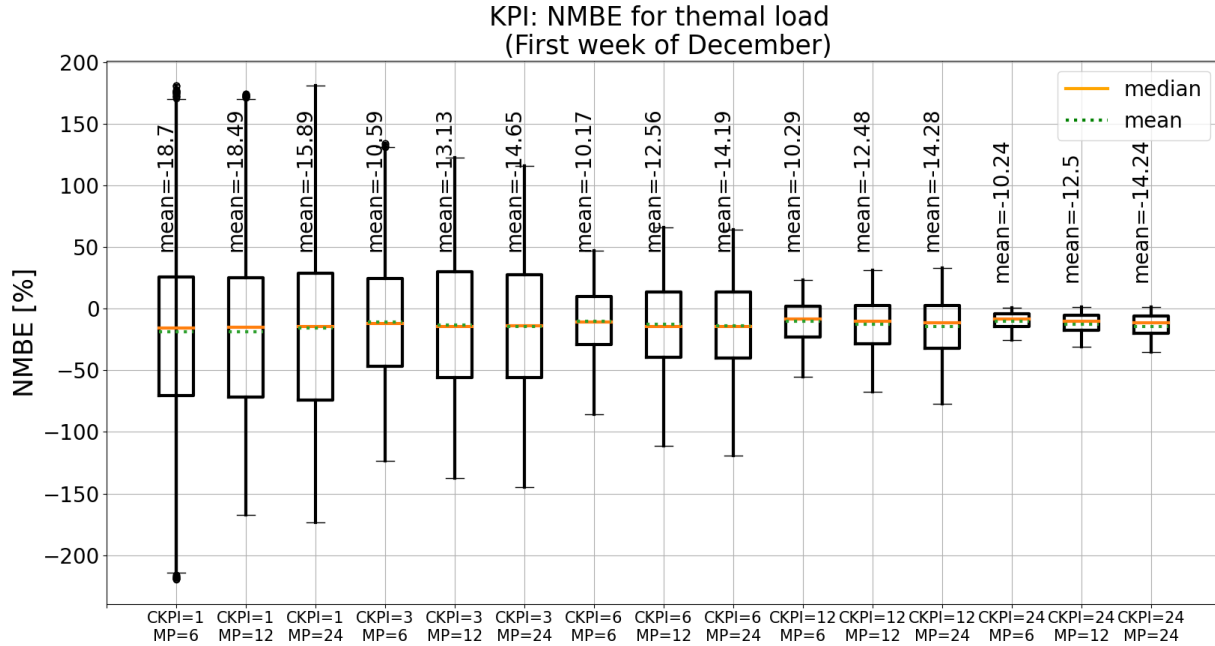


Figure 3-16. NMBE for thermal load

In the proposed model, training load-ANN and zone temperature models are trained sequentially, with the training load model being trained first and then the zone temperature model being trained on the output of the load model. In this regard, the total training time for both models are presented in Table 3-1. The total training time for both models is between 1.3 to 2.9 minutes, which is reasonable for a model that provides hourly predictions for an entire year. The training time is shorter during the summer season, which can be attributed to the lower thermal load and the relatively stable weather conditions during this period.

Also, As the results are presented for a one-week period, and one prediction is made every hour, it is not feasible to present all the simulation times. However, the model's minimum and maximum simulation times were 4.1 and 8.6 seconds, respectively.

Table 3-1. Time of training for winter and summer [minutes]

Days	1st day	2nd day	3rd day	4th day	5th day	6th day	7th day
Winter	2.9	2.7	1.5	1.3	2.4	2.6	1.6
Summer	2.7	1.4	2.1	1.4	1.3	1.8	1.8

To optimize training time, one can enhance the computational power of the training system or employ parallel processing methods. The duration required to train a machine learning model depends significantly on the specifications of the computer system utilized. In general, a more robust system yields faster training times. For instance, a high-end graphics processing unit (GPU) can significantly expedite the training process by leveraging parallel processing techniques.

Similarly, a system equipped with ample random-access memory (RAM) can reduce data loading time during training. Consequently, the reported training times were influenced by the specific system specifications employed, and using a different system with distinct specifications may lead to varying training times.

3.1.11.1 Weight Initialization: Classic Approaches vs. Proposed Method

The Keras library offers various pre-existing methods for weight initialization. However, based on the observations, the commonly used methods in the Keras library did not consistently yield optimal results for this specific use case. Consequently, we developed a novel initialization method that demonstrated improved outcomes and faster convergence compared to the conventional approaches. Notably, this method enables the partial retention of previous gains, which is advantageous when the physical system undergoes structural changes. Furthermore, the proposed method includes a switch that allows users to either discard previous weights entirely or render the model non-adaptive, enhancing flexibility in model development. For comparison, the results presented in Figure 3-17 were obtained using Glorot uniform (GU) initialization for winter. It is evident from the results that GU initialization has led to chaotic predictions and produced unsatisfactory results. This chaos is particularly noticeable in the temperature section, which is concerning as temperature prediction is used as an input for load modeling and can significantly affect thermal load prediction.

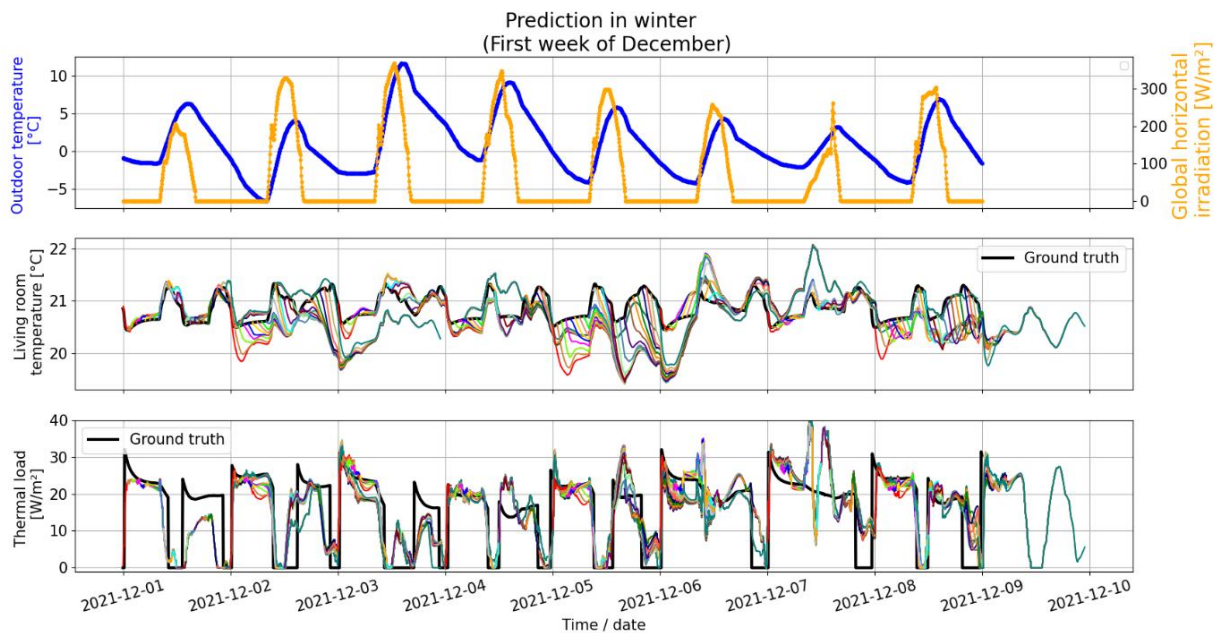


Figure 3-17. Living room temperature and thermal load prediction for the first week of December. Weight initialization: Glorot uniform

To compare the performance of the proposed weight initialization method with the GU initialization, we considered only RMSE as a quantitative measure. Figure 3-18 (a) shows the RMSE of thermal load prediction in winter with GU initialization, which is the same as the graph in Figure 3-11 (a) for the proposed initialization method. Interestingly, both the mean and range of RMSE values in Figure 3-18 (a) are higher than those in Figure 3-11 (a). Moreover, Figure 3-18 (b) shows the RMSE of living room temperature prediction with GU initialization, while Figure 3-11 (a) presents the RMSE for the proposed initialization method. Again, we observe that the mean RMSE is higher, and the error range has increased when using GU initialization.

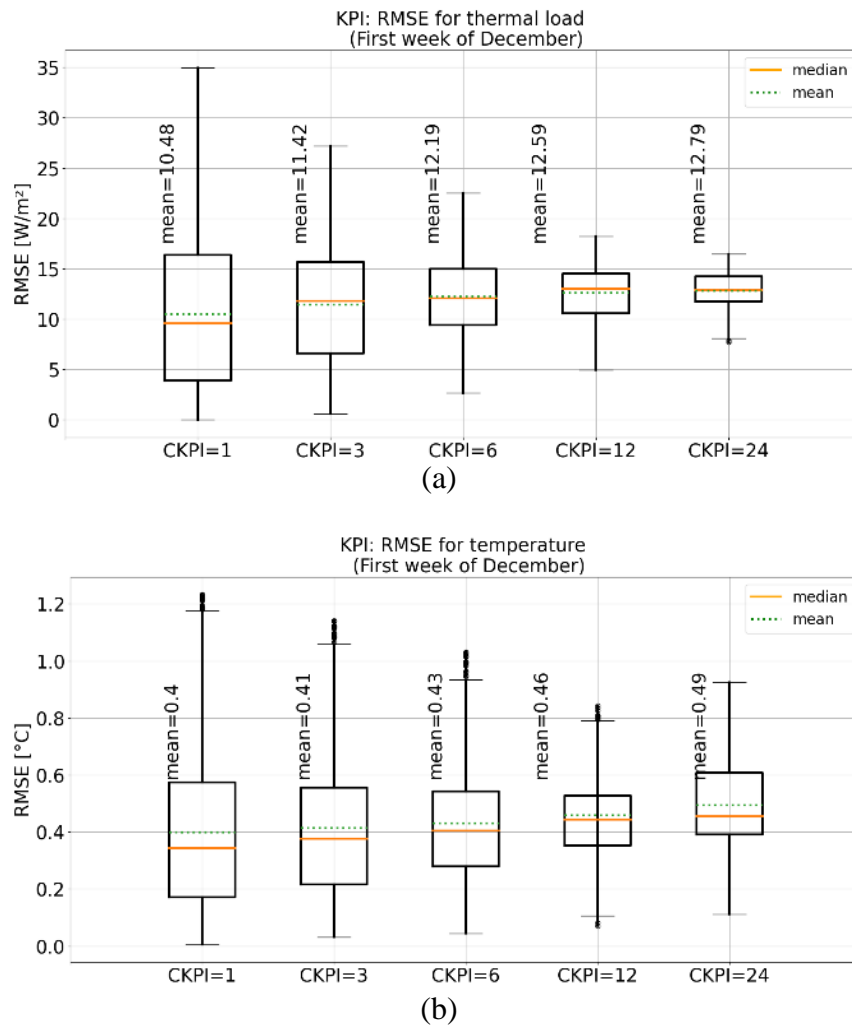


Figure 3-18. RMSE of thermal load (a) and temperature (b). Weight initialization: Glorot uniform

Research findings indicate that utilizing the GU initialization method results in both an increased average error and a broader range of errors compared to the proposed initialization method.

The strong performance of the proposed initialization method and the satisfactory outcomes it produced for model control suggest that it can be effectively used in practical applications.

Table 3-2. Comparison of training time for proposed and GU initialization methods for winter [minutes]

Days	1 st day	2 nd day	3 rd day	4 th day	5 th day	6 th day	7 th day
Proposed weight initialization	2.9	2.7	1.5	1.3	2.4	2.6	1.6
GU initialization	2.6	7	3	1.5	1.2	1.2	1

Table 3-2 provides a comparison of the training times for the two initialization methods over a period of seven days. The minimum and maximum times for the proposed method are 1.3 and 2.9 minutes, respectively, while for the GU initialization method, they are 1 and 7 minutes, respectively. The proposed method generally shows more consistent and faster training times than the GU initialization method.

While other initialization methods might yield better results with further investigation and experimentation, the current focus was on developing an effective initialization method specifically for this project, rather than exhaustively comparing all possible methods. Thus, proposed method is well-suited for the purpose of this project, and it is believed to be a valuable contribution to the field.

3.1.12 Discussion

The major findings of this work highlight several advantages of the proposed ANN model compared to previous studies and existing methods. These advantages can be summarized as follows:

1. **Versatility and Adaptability:** Unlike conventional approaches that rely on specific assumptions about building characteristics or location, the proposed model adopts a black-box data-driven approach, making it highly versatile and adaptable to different building types and sizes. It learns underlying patterns and relationships by collecting data from the building's performance over time, without explicitly requiring detailed information about the specific characteristics of each building.
2. **Practicality and Cost-effectiveness:** proposed model utilizes simple and commonly available inputs, such as outdoor temperature, global horizontal irradiation, zone temperature, internal gain, day of the week, and time. By focusing on easily accessible inputs, it can be applied to a wide range of buildings without requiring complex or

specialized data collection. This practical and cost-effective solution sets it apart from other methods that may require extensive building-specific information.

In comparing proposed approach to previous studies, this model offers notable advantages. It is designed to be adaptive and continually trained with newly available data, enabling it to improve its forecasts over time and accommodate changes in building characteristics and behavior. Furthermore, this model achieves accurate predictions with minimal data by employing a simple MLP architecture with advanced techniques like specific internal state reset and specialized weight initialization functions. This simplicity not only allows for efficient implementation across various building types but also showcases the effectiveness and potential of proposed method in achieving superior outcomes.

While acknowledging that each building may possess unique characteristics, this approach provides a practical and cost-effective solution for accurate thermal load predictions. The model's adaptability, simplicity, and the use of common inputs make it suitable for general applications across a wide range of building types and characteristics.

However, it is important to address potential limitations and conflicting results. Further investigation is warranted to assess the model's performance in specific scenarios with unusual building characteristics or extreme climatic conditions. Additionally, future studies could explore potential refinements to enhance the model's robustness and accuracy.

In summary, this work advances the field by offering a versatile, practical, and cost-effective ANN model that surpasses previous approaches. It demonstrates the advantages of adaptability, simplicity, and accuracy while acknowledging the need for continued research to address potential limitations and explore further refinements.

3.2 Thermal energy storage model

Thermal Energy Storage (TES) is a game-changing tech that stores heat or cold, like how batteries store electricity. It captures excess heat for later use, boosting energy efficiency and system reliability. TES taps into renewable sources and industrial processes, preventing energy waste and reducing grid stress during peak demand. This tech cuts costs by using cheaper energy when available and cutting emissions.

A prevalent form is sensible heat storage, well-suited for buildings due to its cost-effectiveness and absence of risks associated with toxic materials. Sensible heat storage harnesses the heat capacity and temperature variation of the storage medium during the charging and discharging phases. The quantity of stored heat relies on the medium's specific heat, temperature shift, and the volume of storage material [127]. Equation (3.14) accurately depicts this relationship.

$$Q_s = \int_{T_{start}}^{T_{end}} mC_p dT = \int_{T_{start}}^{T_{end}} \rho V C_p dT \quad 3.14)$$

where: Q_s is the quantity of heat stored, in J ; m is the mass of heat storage medium, in kg ; C_p is the specific heat, in $J/(kg \cdot ^\circ C)$; T_{start} is the initial temperature, in $^\circ C$; T_{end} is the final temperature, in $^\circ C$; ρ is the density in kg/m^3 and V stands for volume in m^3 .

The thermal storage capabilities of various solid-liquid materials are highlighted, and it becomes evident that water is favored as the preferable choice for efficient storage of sensible heat. This preference can be attributed to its cost-effectiveness and notably high capacity to hold heat. A simplified diagram of a hot water tank has been crafted to depict the tank's operation during both charging and discharging phases. Figure 3-19 illustration showcases how the tank functions in these two operational modes. The subscripts "in," "out," "d," and "c" denote the terms "inlet," "outlet," "discharge," and "charge," respectively.

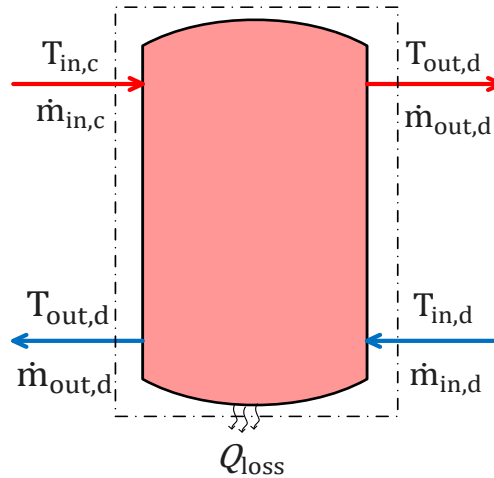


Figure 3-19. Simplified diagram of TES

However, situations where temperatures go beyond 100°C require the use of oils, molten salts, liquid metals, and similar materials [128]. The method of using hot water tanks to store thermal energy is well-known. They are utilized to save energy in water heating systems that depend on solar energy or HPs. When combined with heat pumps, TES increases effectiveness by reusing stored warmth. The efficiency of this combination is further improved by sophisticated controllers, such as MPC, which optimize energy consumption for both comfort and environmental well-being. As previously mentioned, MPC is a method of control that relies on having a model capable of predicting future outcomes. This model helps the controller make decisions about how to control something to get the best results. So, having a good model that can predict accurately how a system will react to different controls is important for MPC to work well. Therefore, it's clear that making model for TES system when using MPC is necessary.

While ANN hold potential for this task (same as thermal load model), their utilization can be accompanied by notable challenges. One significant hurdle involves the process of hyperparameter tuning. ANNs contain various settings that dictate their performance, and determining the ideal combination of these parameters can be a complex and time-consuming task [129]. What proves effective for one dataset might not yield satisfactory results for another, requiring meticulous experimentation and fine-tuning to attain optimal performance. Moreover, the efficacy of ANNs often hinges on the availability of substantial amounts of training data. The process of training neural networks requires a diverse and representative dataset to ensure accurate predictions. However, in scenarios where data collection is limited, sparse, or resource-intensive, this requirement can present a substantial obstacle. Gathering the requisite volume of data might be

impractical or time-consuming, potentially impeding the effective utilization of ANNs for predictive modeling in MPC. To address these challenges, an alternative approach that holds promise is mathematical modeling. Mathematical modeling is the craft of creating a set of equations. These equations should be intricate enough to mirror the real world and yet straightforward enough to offer understanding into the situation [130].

Mathematical models offer a distinct set of advantages that directly address the concerns associated with ANN-based modeling. These models provide transparency and interpretability, allowing for a clear understanding of the relationships between input variables and system behavior. Additionally, they often do not demand an extensive dataset for effective implementation, making them well-suited for cases where data availability is a constraint. Furthermore, mathematical models inherently offer a level of control and flexibility that can prove invaluable in the context of MPC. These models can explicitly incorporate underlying physical principles and constraints, enabling a more intuitive integration of control objectives. Importantly, they can lead to faster computations compared to the iterative training and optimization processes characteristic of ANNs, an attribute that aligns well with the real-time demands of predictive control strategies. In conclusion, while ANNs hold promise for predictive modeling in MPC, challenges related to hyperparameter tuning and data requirements can hinder their efficacy, particularly in scenarios where time and data availability are limited. Mathematical modeling emerges as an attractive alternative, offering transparency, efficiency, and accuracy. By capitalizing on the strengths of mathematical models, practitioners can achieve reliable predictions and well-informed decision-making, ultimately enhancing the effectiveness of control strategies in dynamic systems.

3.2.1 Mathematical model of thermocline TES

Water becomes less dense when it gets heated. This makes the warmer water stay at the top of the tank. So, there's a layer of hot water at the tank's upper part. At the same time, because cold water is denser than hot water, it goes down to the tank's bottom, forming a cold region. The difference in temperature between the cold and hot water in the tank creates something called a 'thermocline' layer. This thermocline layer acts like a kind of wall, stopping the hot and cold water from mixing together. Inside this thermocline, the temperature changes quickly, and that makes a sharp change in temperature. This sharp change helps heat move faster from the hot layer to the cold layer, which makes the energy storage tank work better. When the thermocline is thinner, the difference between the cold and warm parts is even bigger.

In this thesis, a TES system with three distinct layers has been considered. These layers consist of the upper layer and the lower layer and thermocline layer. The location of the thermocline adjusts depending on whether the system is undergoing charging or discharging processes. As a result of these shifts, the volumes of the upper- and lower-layers experience modifications. To visualize this setup, refer to Figure 3-20, which illustrates the proposed model's schematic configuration. This model serves to explain how the proposed TES functions, depicting the relationship of the thermocline, the upper layer, and the lower layer during different operational phases.

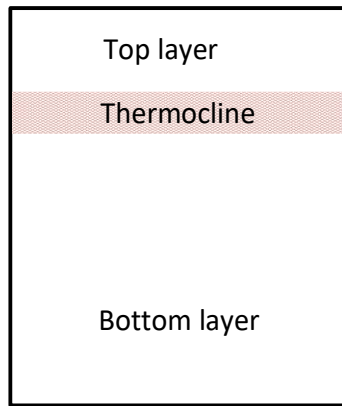


Figure 3-20. Stratification of the proposed model

The temperature distribution across the tank is visually represented in Figure 3-21. A linear temperature distribution is assumed within the thermocline. T_{max} is allocated as the highest temperature present within the tank, while T_{min} signifies the lowest temperature within the tank.



Figure 3-21. Distribution temperature in the tank

The calculation of a weighted average temperature for the upper and lower portions can be achieved based on T_{max} , T_{min} , the thermocline width, and the heights of the top and bottom layers. A more detailed depiction of the tank's arrangement is presented in Figure 3-22.



Figure 3-22. Stratification of the proposed model with more details

W is the width of thermocline. h_{top} represents the height of the upper layer, measured from the tank's top to the middle of the thermocline's width. h_{bot} signifies the height of the lower layer, extending from the tank's bottom to the middle of W . H is the general height of the tank. The

parameters h_1 and h_2 indicate the positions of the upper and lower edges of the thermocline, which vary along the height of the tank. h_1 can be mathematically represented as Eq. (3.15).

$$h_{1_i} = \dots \quad 3.15$$

The weighted average of the T_{top} and T_{bot} can be shown in Eq. (3.16) and Eq. (3.17).

$$T_{top,i} = \dots \quad 3.16$$

$$T_{bot,i} = \dots \quad 3.17$$

To characterize the temperature distribution within the tank with precision, a set of equations is employed as Eq. (3.18). These equations define how the temperature (T) varies at different heights (z) within the tank. The function $T(z)$ is structured as a piecewise expression to accurately capture the variations. In the region between h_1 and h_2 , $T(z)$ changes gradually from T_{min} to T_{max} as z varies. This transition corresponds to the thermocline, where a distinct change in temperature occurs. For heights beyond h_2 , the temperature stabilizes at T_{max} . For heights below h_1 , the temperature stabilizes at T_{min} . This arrangement of equations provides a comprehensive representation of the temperature profile within the tank.

$$T(z) = \begin{cases} T_{min} & z < h_1 \\ \dots & h_1 < z < h_2 \\ T_{max} & z > h_2 \end{cases} \quad 3.18$$

The energy balance equation is employed to depict the movement of energy within the hot water tank. Facilitates comprehension of how temperature alterations are influenced by the inflow and outflow of heat. Through the consideration of energy inputs and outputs, a deeper insight into the tank's thermal dynamics can be attained. The energy balance equation can be represented as Eq. (3.19).

$$\rho C_v A (\dots) = \dots \quad 3.19$$

The expanded form of this equation can be represented as (3.20). This extended version provides a more detailed account of the various factors involved in the energy balance within the tank.

$$\rho A C_v (\dots) = \dots \quad 3.20$$

In equations (3.19) and (3.20), ρ is density, A shows area, \dot{m} represents the mass flow rate, C_p signifies the specific heat capacity, UA refers to the overall heat transfer coefficient, T_{in} is the inlet temperature and T_{out} is outlet temperature. T_{amb} represents the ambient temperature and Δt is timestep.

3.2.1.1 Dynamic Stages of TES

In the realm of mathematical modeling, the thermocline TES system that has been formulated features four marked stages (both in charge and discharge). These stages encapsulate the dynamic behaviors inherent in the TES system during both charging and discharging processes. Each stage is established by its distinct properties and equations, as dictated by the mathematical model. The focus is on understanding the intricate behaviors and reactions of the thermocline TES system as it progresses through these stages. The equation used in the modeling of TES varies slightly between the charging and discharging processes. Let's begin by discussing the charging process before addressing the discharge process.

3.2.1.1.1 Charge mode

3.2.1.1.1.1 Stage one: Expansion

In the context of the mathematical modeling of thermocline TES during charging mode, consider a water tank initially possessing a uniform temperature. Upon commencement of the charging process, the gradual formation of a thermocline takes place. This thermocline emerges within the proximity of the water inlet. The progression of the thermocline's formation will cease if either of the following two conditions is met:

- 1) When the upper edge of the thermocline comes into contact with the top of the tank.
- 2) When the width of the thermocline (W) reaches the predetermined optimal width known as W_{opt} .

The process used to identify the W_{opt} can be characterized as an optimization procedure. It entailed systematically running the model with a range of W values and concurrently evaluating the resulting RMSE for each setting. This iterative method facilitated the discovery of the optimal W value that minimizes the RMSE, effectively optimizing the performance of the model.

In this phase, while the thermocline is in the process of formation and remains in a state of immobility, alterations will not occur in the values of h_{top} , h_{bot} , h_1 , and h_2 . However, a dynamic evolution is observed in the parameter W over time. The depiction of the thermocline formation (in charging) is presented in Figure 3-23. In this illustration, it's evident that the process commenced at $t_{start,ex}$ and concluded at $t_{start,ex} + n + k$ (to provide a clear example, we have taken into account a scenario where W is equal to W_{opt}). The “*ex*” notation is used to indicate the “expansion” phase.

Figure 3-23. Thermocline formation in charge mode

For the purpose of determining the energy balance during this phase, the expression denoted as (3.20) can be formulated in the subsequent manner:

$$\rho AC_v(\dots) = \dots \quad 3.21)$$

In Eq. (3.21), $T_{top,i}$, $T_{bot,i}$ and $T_{out,i}$ are unknown. Consequently, recourse can be taken to employ equations of weighted average temperature derived from the top and bottom layers as a means of resolving these indeterminate variables.

$$T_{top,i} = \dots \quad 3.22)$$

$$T_{bot,i} = \dots \quad 3.23)$$

Through the utilization of the weighted average temperature involving both the upper and lower layers, certain variables are indeed determined. However, several unknowns, notably T_{max} , T_{min} , and W , remain. This underscores the pivotal role of assumptions in shaping the dynamics of this modeling process. Assumptions wield significant influence in mitigating the complexities arising from unresolved variables, thereby aiding in generating a more comprehensible and manageable representation of the system under study.

However, their effectiveness hinges on a crucial factor: these assumptions must align seamlessly with the realities of the system being studied. To put it simply, assumptions act as bridges between proposed model and the real world. These bridges are strongest when they're built on solid ground – the ground of reality. Assumptions are not just empty spaces; they function as essential components that make the model applicable and effective in real-world scenarios. While assumptions assist us in untangling puzzles involving things like unknown temperatures and width, they can't be disconnected from the real world. Assumptions are tools that help proposed model make sense of the reality, but they're effective only when they mirror how things truly operate. As mathematical modeling progresses, it is important that the assumptions made are in sync with the real world. In this way, the proposed model becomes a clearer reflection of reality, enabling a better understanding of and interaction with the sophisticated mechanisms that shape the surroundings.

An essential assumption arises from the equation (3.18). It implies that since the thermocline is positioned above the sensor out, we can consider $T_{min,i}$ to be the same as $T_{SensorOut,i-1}$. Simultaneously, we can assume that when thermocline is not reaching the sensor out yet, $T_{out,i}$ also can be equate to $T_{min,i}$ which is equal to Therefore, these two assumptions can be represented as:

$$T_{min,i} = \dots \quad 3.24)$$

$$T_{out,i} = \dots \quad 3.25)$$

The quest to unravel the unknown $T_{max,i}$ still remains. To address this puzzle, a solution emerges in the form of calculating the weighted average of the water mass situated above the thermocline. The methodology involves formulating the temperature $T_{max,i}$ as follows: it's determined by the weighted combination of two temperature components. The first component, $T_{in,i}$ which is associated with the incoming water mass rate (represented by m), and it takes into account the change in time (Δt). The second component, $T_{max,i-1}$, corresponds to the preceding T_{max} value, but it's influenced by the adjustment made with respect to the vertical distance $h_{top_ex,i-1} - \frac{W_i}{2}$ and the mass of water that is stored there.

$$T_{max,i} = \dots \quad 3.26)$$

At this point in time, by employing all the equations (3.21), (3.22), (3.23), (3.24), (3.25) and (3.26), we have the capability to determine all the unknown values which are $T_{min,i}, T_{max,i}, T_{top,i}, T_{bot,i}, T_{out,i}, W_i$.

As discussed, the thermocline formation halts either when it reaches the top of the tank or when its width equals W_{opt} . There are times when our calculations might place W just a bit under W_{opt} . Even though it's near, the following step could gently push it past the limit, which is W_{opt} . It's same to finding balance on the edge of a line – a slight push can cause a shift. Similarly, even if the width of the thermocline is okay, we need to be cautious about where the top part is headed next. Sometimes, even if it's fine now, in the next step, it might go too high and violate the top of the tank, which wouldn't make sense. Hence, to monitor the forthcoming values of W and the upper edge of the thermocline, consideration has been given to equation (3.27).

$$\begin{aligned} \Delta x_i &= \dots \\ x_{i+1} &= \dots \end{aligned} \quad 3.27)$$

As a result, if using this equation indicates that the next step may exceed the bounds, it's time to commence movement rather than proceeding to the next iteration.

3.2.1.1.1.2 Stage two: Movement

After the completion of the thermocline's formation, that's when the movement of the thermocline begins in a downward direction. Therefore, alterations will occur in h_{top} , h_{bot} and the thermocline's position. However, following the commencement of thermocline movement, the width of the thermocline will stay consistent. So, in contrast to equations (3.21), (3.22), (3.23), (3.24), (3.25) and (3.26) where h_{top} and h_{bot} remained constant while W changed, the situation changes here. At this point, h_{top} and h_{bot} change while W remains steady. This W now matches the last value determined in the 'expansion' stage. Figure 3-24 illustrates the progression of thermocline movement in charge mode.



Figure 3-24. Movement of thermocline in charging mode

Therefore, equations (3.21), (3.22), (3.23) and (3.26) can be written as follows:

$$\rho A C_v(\dots) = \dot{m}_l C_p (T_{in,i} - T_{out,i}) \dots \quad 3.28)$$

$$T_{top,i} = \dots \quad 3.29)$$

$$T_{bot,i} = \dots \quad 3.30)$$

$$T_{max,i} = \dots \quad 3.31)$$

Equations (3.24) and (3.25) will remain unchanged from their previous forms. Hence, by employing Equations (3.28), (3.29), (3.30), (3.31), (3.24) and (3.25), it becomes possible to compute the unknown variables existing at this point that are $T_{min,i}$, $T_{max,i}$, $h_{top,i}$, $T_{top,i}$, $T_{bot,i}$, $T_{out,i}$. Upon comparing the equations utilized in both the 'expansion' and 'movement' phases, the sole distinction pertains to the notation assigned to the variables. Here, the symbol "m" is employed to denote the "movement" phase. It is intended to continue the movement until the lower edge of the thermocline encounters the sensor output, situated precisely at the outlet port. Upon contact, the subsequent stage will commence.

The position of the thermocline can be determined at this stage based on the movement of the thermocline. Also, since $h_{top,i}$ is calculated by the system of equations, $h_{bot,i}$ can also be easily calculated. Equation (3.32) determined all these parameters.

$$\begin{aligned}
 \Delta h_i &= \dots \\
 h_{1,i} &= \dots \\
 h_{2,i} &= \dots \\
 h_{bot,i} &= \dots
 \end{aligned}
 \tag{3.32}$$

The speed of the thermocline is represented by Equation (3.33).

$$S_i = \dots \tag{3.33}$$

The alteration of the thermocline's position causing variations in h_{top} and h_{bot} results in modifications to the masses of both the upper and lower layers. The calculation of these changes is explained by Equation (3.34).

$$\begin{aligned}
 m_{top,i} &= \dots \\
 m_{bot,i} &= \dots
 \end{aligned}
 \tag{3.34}$$

3.2.1.1.1.3 Stage three: Assumption revision

When the lower edge of the thermocline reaches the outlet port, this signals the beginning of changes in T_{out} . Since T_{min} represents the tank's minimum temperature, in that, it's essential to notice that T_{min} cannot be equated with ... anymore. Thus, Eq. (3.24) can be turned to Eq. (3.35).

$$T_{min,i} = \dots \tag{3.35}$$

Apart from this alteration, none of the remaining equations will undergo modification and thermocline will persist in its motion until it reaches the tank's bottom. Consequently, just like in the 'movement' stage, all the unknowns will be computed.

3.2.1.1.1.4 Stage four: Contraction

After the lower part of the thermocline reaches the bottom of the tank, contraction phase will start. An innovative technique was employed to simulate the controlled contraction of the thermocline. To achieve this, a strategic decision was made to artificially prevent the lower edge of the thermocline from moving, while allowing the upper edge to undergo adjustments. By blocking the lower edge's movement, we essentially restricted the thermocline's shrinkage to upward direction

and thermocline will be contracted downwardly. Hence, in this phase, the unknown variables encompass $T_{min,i}, T_{max,i}, h_{top,i}, T_{top,i}, T_{bot,i}, T_{out,i}, W_i$.



Figure 3-25. Contraction stage in charging mode

In the 'formation' stage, as evident from equations (3.22) and (3.23), $h_{top,i}$ and $h_{bot,i}$ remained consistent while W_i underwent variations. In contrast, in the 'movement' or 'assumption revision' stage, within the framework of equations (3.29) and (3.30), W_i remained stable while $h_{top,i}$ and $h_{bot,i}$ experienced changes.

Transitioning to the 'contraction' stage, as demonstrated by Eq. (3.16), (3.17) and (3.36) all three parameters — $h_{top,i}$, $h_{bot,i}$ and W_i — are subject to alterations, rendering them unknown variables.

$$T_{max,i} = \dots \quad 3.36$$

Given that we currently have 7 unknowns and only 6 equations available, we require an additional equation to facilitate the solution for these unknowns. In this stage, the width of the thermocline is calculated using the equation (3.37).

$$W_i = \dots \quad 3.37$$

To clarify why the coefficient for (...) was considered ., following description provides a deeper insight.

The artificial constraint introduces a mathematical anomaly that must be addressed. When the upper edge moves by Δh_{top} the actual middle position of the thermocline does not shift by the same unit due to the immobilization of the lower edge. This shift discrepancy results from the fact that any change in $h_{top,i}$ only affects half of the thermocline's effective height. To explicate, consider a scenario where $h_{top,i}$ experiences an increment of 1 cm. Given that the lower edge remains static, the 'center' or 'midpoint' of the thermocline shifts only by 0.5 cm. Such a differential behavior requires an adjustment in our mathematical representation to ensure that it mirrors the physical reality of the system.

At this stage, ultimately, using equations (3.25), (3.28), (3.35), (3.16), (3.17), (3.36) and (3.37) we are able to calculate all the unknowns.

An important point is that once the thermocline has completely passed through the outlet sensor, the simulation terminates, as there are no additional sensors for measurement beyond the outlet point.

3.2.1.1.2 Discharge mode

3.2.1.1.2.1 Stage one: Expansion

As the discharge process initiates, the gradual development of a thermocline occurs. This thermocline emerges close to the water inlet. The progression of the thermocline's formation ceases if either of the following two conditions is met:

- 1) When the lower edge of the thermocline comes into contact with the bottom of the tank.
- 2) When the width of the thermocline (W) reaches the predetermined optimal width known as W_{opt} .

Same as charging mode, during this stage, as the thermocline forms and stays still, the values of $h_{top,i}$, $h_{bot,i}$, $h_{1,i}$ and $h_{2,i}$ do not change. The parameter W_i undergoes a changing process as time goes by. Figure 3-26 displays how the formation of the thermocline occurs during the discharge process. As it observed, the process commenced at $t_{start,ex}$ and concluded at $t_{start,ex} + n + k$ (to provide a clear example, we have taken into account a scenario where W_i is equal to W_{opt}). Same as charging mode, the "ex" notation is used to indicate the "expansion" phase.



Figure 3-26. Thermocline formation in discharge mode

In this stage, $T_{min,i}$, $T_{max,i}$, $T_{top,i}$, $T_{bot,i}$, $T_{out,i}$, W_i are unknowns. What's interesting is that the equations used to figure out these unknowns are pretty much the same as what we used during the charging phase. Equation (3.21), (3.22), (3.23) and (3.25) are the same and remain unchanged. However, in the discharge phase, there's a switch in the roles of T_{min} and T_{max} . To put it simply, what we thought of as T_{min} during charging becomes T_{max} during discharge, and vice versa. Equation (3.38) and (3.39) representing these changes.

$$T_{max,i} = \dots \quad 3.38)$$

$$T_{min,i} = \dots \quad 3.39)$$

At this point in time, by employing all the equations (3.21), (3.22), (3.23), (3.25), (3.38) and (3.39) we have the capability to determine all the unknown values.

3.2.1.1.2.2 Stage two: movement

Following the completion of thermocline formation during the discharging phase, the upward motion of the thermocline comes into play. Consequently, adjustments are made to $h_{top,i}$,

$h_{bot,i}$ and the position of the thermocline. Same as charging process, once the thermocline's upward movement begins, the width of the thermocline remains constant. In this stage, $T_{min,i}, T_{max,i}, h_{top,i}, T_{top,i}, T_{bot,i}, T_{out,i}$ are unknowns that using equations (3.25), (3.28), (3.29), (3.30), (3.38) and (3.39) can be calculated. Figure 3-27 illustrates the progression of thermocline movement in discharge mode.



Figure 3-27. Movement of thermocline in discharge mode

Just like in the charging mode, after the thermocline forms, it begins to move. This movement carries on until the upper part of the thermocline reaches the sensor placed at the outlet port. Same as charge mode, height of bottom layer and the position of the thermocline, the speed of movement of the thermocline and the mass of each layer are calculated through the equation (3.32), (3.33) and (3.34).

3.2.1.1.2.3 Stage three: Assumption revision

When the highest point of the thermocline reaches the output port, the start of changes in $T_{out,i}$ is indicated. Since $T_{max,i}$ stands for the highest temperature of the tank, it's important to observe that $T_{max,i}$ can no longer be considered equal to $T_{SensorOut,i-1}$ because it the time that output temperature start decreasing. Thus, Eq. (3.38) can be turned to Eq. (3.40).

$$T_{max,i} = \dots \quad 3.40)$$

Apart from this adjustment, none of the other equations are changed, and the thermocline continues its movement until it reaches the upper part of the tank. Therefore, just like in the 'movement' stage in discharge, all the unknown values are calculated.

3.2.1.1.2.4 Stage four: Contraction

Similarly, during the 'contraction' phase in discharge mode, once the upper edge of the thermocline makes contact with the tank's ceiling, we deliberately halt the upward movement of the upper edge. This action initiates the process of compressing the thermocline. Figure 3-28 illustrates the process of contraction in discharge mode.



Figure 3-28. Contraction stage in discharge mode

Unknown in this stage are $T_{min,i}$, $T_{max,i}$, $h_{top,i}$, $T_{top,i}$, $T_{bot,i}$, $T_{out,i}$, W_i which can be calculated using equation (3.25), (3.28), (3.16), (3.17), (3.37), (3.39) and (3.40).

Similar to the charging mode, once the thermocline has completely passed through the outlet sensor, the simulation terminates, as there are no additional sensors for measurement beyond the outlet point.

3.2.2 Methodology validation

3.2.2.1 Case study

A study involving the analysis of a commercial hot water storage tank (KOOLTANK 2000, IMA s.r.l.) for a thermal energy storage case study has been conducted at Eurac Research's Energy Exchange Lab. This tank features four ports serving specific purposes:

1. The top-left port is connected to the heat pump's outlet.
2. The top-right port is linked to the load.
3. The bottom-left port connects from the tank to the heat pump.
4. The bottom-right port connects from the load to the tank.

Figure 3-19 simply depicts how the tank operates in charge/ discharge mode. To monitor temperature variations within the tank, various sensors have been positioned at different heights.

A LabVIEW-based control and data acquisition system, operating at a 2-second sampling rate, is installed in the Energy Exchange Lab. The platinum RTD thermometer has a maximum inaccuracy of $\pm 0.24^\circ\text{C}$ at 85°C . Measurement of volumetric flowrate is achieved through a magnetic flowrate sensor, accurate within $\pm 0.008 \text{ m}^3/\text{hr}$. Mass flowrates are calculated under the assumption of constant water density. Figure 3-29 provides an expansive view of the TES setup within the laboratory.



Figure 3-29. TES setup within the laboratory

The tank present in the laboratory does not possess a perfectly cylindrical shape. Instead, its overall volume is composed of three distinct sections: two spherical caps situated at the tank's ends and a central cylindrical volume. Given the tank's non-perfect cylindrical shape, we intend to simplify our analysis by assuming the tank to be a pure cylinder. This assumption requires us to compute the equivalent heights at the two spherical caps, a critical step in our approach.

The tank's configuration, as depicted in Figure 3-30 (a), is derived from the manufacturer's datasheet. In contrast, Figure 3-30 (b) displays the calculations we have performed to establish the tank's configuration under the assumption of a perfect cylinder. The values presented in the figures are expressed in millimeters.

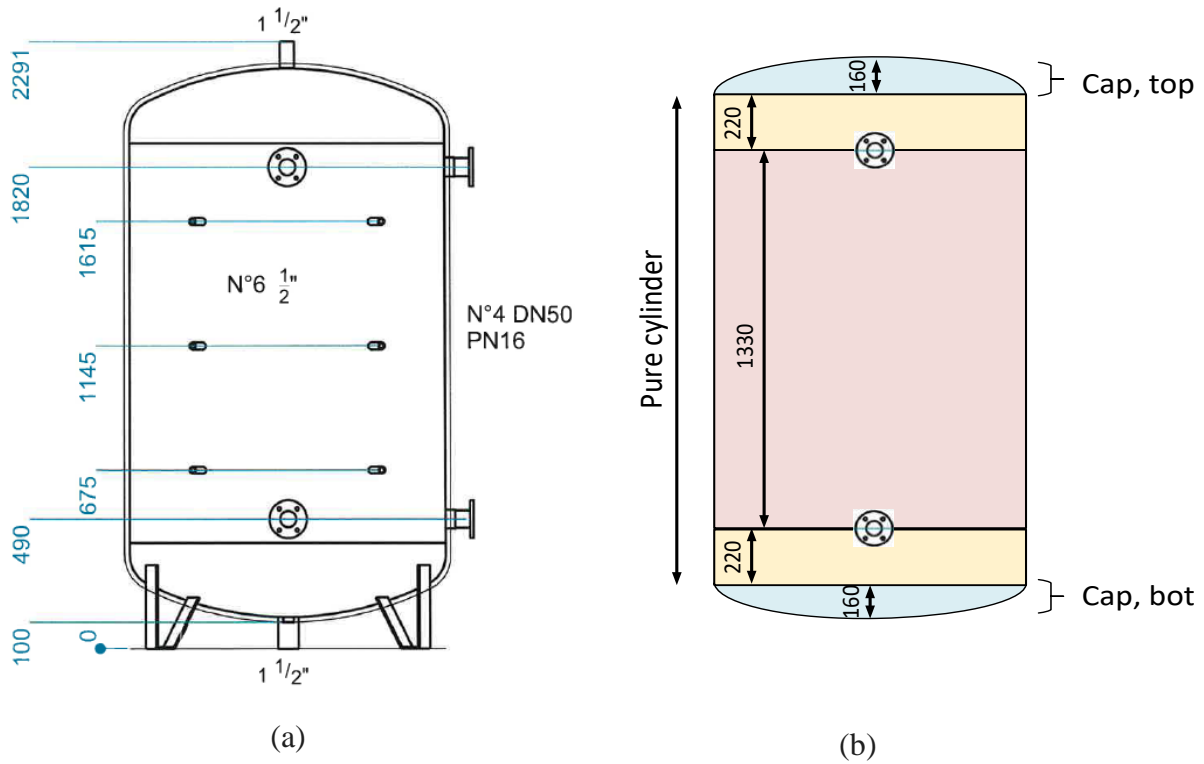


Figure 3-30. (a) tank's configuration derived from the manufacturer's datasheet, (b) tank's configuration under the assumption of a perfect cylinder.

Under the assumption of a perfect cylinder, the overall height of the idealized cylinder is fixed at 177 cm. Consequent to this assumption, Table 3-3 details the placements of sensors and inlet/outlet ports in accordance with this established height. The measurements provided in the table are expressed in centimeters and are referenced from the base of the tank.

Table 3-3. Vertical Positions within the Tank under the Assumption of a Perfect Cylinder (referenced from the base of the tank)

	Position (cm)
Inlet port	155
Sensor top	134
Sensor middle	87
Sensor bottom	40
Outlet port	22

The remaining parameters regarding the tank are documented in Table 3-4.

Table 3-4. Characteristics of the hot water storage tank.

Parameters	Material	Dimension (unit)
Internal diameter	-	120 cm
External diameter	-	140 cm
Thermal conductivity of the tank material	Carbon steel	$50 \frac{W}{m.K}$
Thickness of insulation 1	Polyethylene	2 cm
Thermal conductivity of insulation 1	Polyethylene	$0.3 \frac{W}{m.K}$
Thickness of insulation 2	Polyurethane foam	8 cm
Thermal conductivity of insulation 2	Polyurethane foam	$0.03 \frac{W}{m.K}$

3.2.2.2 Result and discussion

In the lab, tests were conducted on our hot water tank to study its performance during both charging and discharging phases. Various experiments were carried out with different mass flow rates, and temperature distributions were examined. During these tests, the tank was observed to be charged and discharged under controlled conditions. Different parameters were measured and recorded to better understand how the hot water tank behaves in various scenarios. The recorded data primarily consist of ambient temperature, water inlet/outlet temperature, and mass flow rate. After gathering all this information, our proposed TES model was evaluated.

As a crucial point, the measurement of two specific points holds significant importance. Firstly, the sensor output is crucial because it directly influences the calculation of the Heat Pump's COP by providing the inlet temperature of the heat pump. Secondly, the sensor at the top of the tank is equally vital. The temperature recorded at the tank's uppermost part helps inform decisions regarding when to activate or deactivate the heat pump. As such, achieving accuracy in these specific measurement points is of utmost importance.

3.2.2.2.1 Test one, charge mode

This test was conducted in the charging mode, where the mass flow rate of water entering the tank was set at 0.28 kg/s. Initially, the tank had a consistent temperature of approximately 30 °C, while the desired final temperature for the charging process was 40 °C. To monitor this process, we employed various sensors, as indicated in Table 3-3, to measure the temperature of the water inside

the tank. In section 3.2.1.1, we talked about the four stages of our proposed model, and we used Figure 3-31 to show them, based on the test results. We used different colors to distinguish each stage and better understand how the thermocline's behavior changes during the charging process. In "Stage 1", the formation of the thermocline commences and continues until one of the end formation conditions is met. In this test, the formed W at the end of formation stage was 38.5 cm. Subsequently, in "Stage 2," the thermocline begins to move smoothly. Upon reaching the output port, no changes occur in its speed, but this marks the commencement of "Stage 3," during which one of the assumptions undergoes modification (refer to section 3.2.1.1.1.3). "Contraction stage" initiates when the lower edge of the thermocline reaches the bottom of the tank. At this point, the width of the thermocline begins to decrease, as elegantly depicted in Figure 3-31 (b).



Figure 3-31. Stages in our proposed model (based on the result of "Test-1")



Figure 3-32. Charge test. (a) Height changes in each layer (b) Mass changes in each layer in entire process of charging

Figure 3-32 illustrates alterations in the height and, as a result, the mass of the layers. In "Stage 1", no changes occur because there is no movement in the thermocline. As the lower edge of the thermocline gets closer to the tank's bottom, the upper layer's height goes up, and the lower layer's height goes down. When contraction stage commences, the rate of height alterations decreases and approaches zero.



Figure 3-33. Charge test. (a) temperature in the top and bottom layer, (b) monitored and simulated temperature of water along the tank

As depicted in



Figure 3-33 (a) when the charging process begins, the temperature in the top layer starts to rise. As time passes, the temperature of the bottom layer gradually rises. However, when the thermocline descends to the tank's bottom, the bottom layer becomes quite thin, and its temperature stays constant. In fact, once the thermocline reaches the tank's bottom, the bottom layer's height

$(h_{bot,i})$ equals half of the thermocline's width. It's important to mention that the temperature shown here is the weighted average temperature calculated using equations (3.16) and (3.17).

The temperature distribution along the tank is depicted in




Figure 3-33 (b), with solid lines denoting the observed data and dashed lines indicating simulated data. Notably, our proposed model effectively reproduces the observed data. It's important to emphasize that our model assumes a linear temperature profile within the thermocline, resulting in a linear temperature increase, in contrast to the sigmoid-shaped pattern observed in the monitored data. The simulated temperature for the output sensor is not entirely linear; it exhibits a curved shape, particularly in the latter section. This curvature can be attributed to the "contraction" phase. To evaluate the model's accuracy, we utilized the RMSE. The RMSE values between the observed and simulated data at various sensor locations, including the top, middle, bottom, and outside sensors, are 0.5 °C, 0.44 °C, 0.34 °C, and 0.44 °C, respectively. The key consideration here is that the RMSE is computed for the whole of the charging process.



Figure 3-34. Charge test. (a) Power gives to the tank, (b) The absolute difference between observed and modeled data.

In Figure 3-34 (a), the power supplied to the tank is displayed in black based on the monitored data, while the power calculated from simulated data is shown in red. Additionally, Figure 3-34 (b) presents the absolute difference between the monitored and simulated data. It is evident that our proposed model has satisfactorily captured the monitored data. Furthermore, it should be noted that the average of these discrepancies is less than one kW.

3.2.2.2.2 Test two, charge mode

The test was carried out in the charging mode, with the mass flow rate of water entering the tank being set to 0.14 kg/s. Initially, the tank was maintained at a stable temperature of around 30 °C, while the target final temperature for the charging process was set at 70 °C.



Figure 3-35. Charge test. (a) Speed of thermocline, (b) Width of thermocline, (c) Height changes and (d) Mass balance

In Figure 3-35 (a), the speed of thermocline movement is depicted. In Figure 3-35 (b), the formation of the thermocline is illustrated. The optimal W , as identified from the monitored data,

was 40 cm, whereas, according to our model, the formation of the thermocline ceased at 39.9 cm. Figure 3-35 (c) and (d) demonstrate alterations in the height and mass within each layer.

Figure 3-36. Charge test. (a) temperature in the top and bottom layer, (b) monitored and simulated temperature of water along the tank

In Figure 3-36 (a), the weighted average of the top and bottom layer temperatures is presented. Like test 1 (charge), when the thermocline reaches the bottom of the tank, the temperature of the bottom layer remains unchanged. Upon initial examination of Figure 3-36 (b), your attention is drawn to a delay in the proposed model. This delay arises from the extended time required for thermocline formation and a subsequent delay in thermocline movement. Consequently, it is observed that the simulated results exhibit a delay of approximately 20 minutes. Despite this delay contributing to an increased RMSE, it is essential to acknowledge that the model's consistency persists. RMSE values for the top, middle, bottom, and outer sensors stand at 3.1 °C, 3.38 °C, 3.04 °C, and 2.77 °C, respectively.

Figure 3-37. Charge test. (a) Power gives to the tank, (b) The absolute difference between observed and modeled data.

Upon analyzing the power data in Figure 3-37 (a) and (b), it becomes evident that our proposed model exhibits consistency, as it successfully replicates the monitored data. The average discrepancy between the two sets of data is approximately 1.3 kW.

Our model is employed as a critical component in the decision-making process of the MPC controller. Specifically, the optimal times for the activation of the HP are determined by the controller based on factors such as the load or State of Charge (SOC) of TES system. When the HP is activated, it becomes essential to predict the response of the TES system.

Despite potential delays in temperature prediction, our model maintains consistency from an energy perspective. This means that reliable estimations of energy interactions within the system are provided, which are vital for the MPC controller to make informed decisions about when to activate the HP for the effective management and control of the thermal energy storage process.

3.2.2.2.3 Test three, discharge mode

The test was done in a way where water flowed into the tank at a rate of 0.28 kg/s. At first, the tank stayed at a steady 40 °C temperature, and the final goal temperature for the discharging

process was set to 30 °C. As shown in Figure 3-19, during the discharge, the tank is filled with water from the bottom, and water exits from the top of the tank. During the discharge, a thermocline is formed in the area of inlet water port. Over time (as shown in Figure 3-27Figure 3-29), it begins to move upward from the bottom of the tank until it reaches the top of the tank. The results of the test are depicted in Figure 3-38. Figure 3-38 (a) illustrates the speed at which the thermocline moves. By comparing the results of test 1 (3.2.2.2.1), it's evident that the speed of movement in both Test 1 (3.2.2.2.1) and present test is roughly the same because the mass flow rates in both tests are similar.



Figure 3-38. Discharge test. (a) Speed of thermocline, (b) Width of thermocline, (c) Height changes and (d) Mass balance

Based on monitored data, we determined that W_{opt} (optimal width) is equal to 10 cm. As shown in Figure 3-38 our proposed model also predicts that the width of the thermocline is 10 cm. Figure 3-38 (c) and (d) also demonstrates how the height and mass in each layer change based on the movement of the thermocline.



Figure 3-39. Discharge test. (a) temperature in the top and bottom layer, (b) monitored and simulated temperature of water along the tank

Even though our model accurately identified the same value of W as the monitored data, it exhibits a delay in its formation of approximately 10 minutes.

In Figure 3-39 (a), a comprehensive view of temperature variations within each layer during the discharge process is presented. Notably, the inlet port is precisely positioned at a depth of 155 cm, as specified in Table 3-3. Given these established parameters, even as the thermocline completely passes through the inlet port, which signifies a pivotal moment in our simulation, It can be anticipated that the temperature in the top layer will exhibit minimal change. This expectation stems from a key insight: T_{top} , representing the temperature of the top layer, is derived as a weighted average of the temperatures within that specific layer. In the context of the scenario under discussion, where the thermocline does not ascend to the uppermost region of the tank, it implies that the majority of the top layer remains unaffected by temperature fluctuations. Consequently, it

is reasonable to expect that the temperature across most of the top layer remains close to the initial value of around 40 °C, as previously discussed.

Due to the delay in the formation and subsequent movement of the thermocline in our model, we observe that our model aligns with the monitored data, albeit with around 10 minutes time lag, as depicted in Figure 3-39 (b). Despite the presence of a time lag, our model produces encouraging results as evidenced by the calculated RMSE. The RMSE values for the top, middle, bottom, and outlet port are 1.21°C, 1.09°C, 1.07°C, and 0.67°C, respectively. These results indicate a satisfactory level of accuracy in our model's ability to predict temperature variations across different segments of the tank.



Figure 3-40. Discharge test. (a) Power given to the tank, (b) The absolute difference between observed and modeled data.

When we look at the power data in Figure 3-40 (a) and (b), we can see that our proposed model consistently matches the monitored data. There's only about a 0.77 kW difference on average between the monitored data and simulated results.

3.2.2.2.4 Test four, discharge mode

The test was conducted by allowing water to enter the tank at a rate of 0.14 kg/s. Initially, the tank was maintained at a constant temperature of 70 °C, and the target temperature for the end of the discharging process was set at 30 °C.



Figure 3-41. Discharge test. (a) Speed of thermocline, (b) Width of thermocline, (c) Height changes and (d) Mass balance

In Figure 3-41 (a), we can see the speed at which the thermocline moves, and it closely resembles Figure 3-35 due to the matching mass flow rate. Figure 3-41 (b) illustrates how the thermocline forms. The optimal width, determined from the monitored data, was 10 cm. However, our model indicates that the thermocline stopped forming at 8.9 cm. Figure 3-41 (c) and (d) show changes in both height and mass within each layer.




Figure 3-42. Discharge test. (a) temperature in the top and bottom layer, (b) monitored and simulated temperature of water along the tank

As previously discussed in Test 3 (3.2.2.2.3), we do not anticipate significant changes in T_{top} , and Figure 3-42 (a) confirms this expectation. However, over time, as the tank was continuously filled with water at a temperature of 30°C, the temperature in the bottom layer gradually decreased. Because of the delay in the formation and movement of the thermocline in our model, we notice that our model matches the monitored data, although with a time lag of approximately 20 minutes, as shown in Figure 3-42 (b). Despite this time lag, our model delivers promising results, as indicated by the RMSE calculations. Particularly, the RMSE values for the top, middle, bottom, and outlet port are 2.64°C, 2.34°C, 3.5°C, and 1.89°C, respectively. These outcomes affirm that our model performs well in predicting temperature changes in various parts of the tank.



Figure 3-43. Discharge test. (a) Power given to the tank, (b) The absolute difference between observed and modeled data.

Upon examining the power data presented in Figure 3-43 (a) and (b), it becomes evident that our suggested model consistently aligns with the observed data. On average, there is merely a 1 kW discrepancy between the observed data and the simulated results.

3.2.2.3 Conclusion

In conclusion, our study delved into the behavior of a TES system, focusing on the dynamic nature of water temperature within the tank. As water heats up, it becomes less dense, leading to the formation of distinct layers: a warm upper layer and a cool lower layer, with a crucial boundary known as the thermocline that prevents mixing. Our TES system comprised three layers (upper, lower, thermocline) whose volumes and positions changed during charging and discharging processes. Temperature distribution was considered linear within the thermocline, with a maximum and minimum temperature in the tank. Mathematical modeling revealed four distinct stages during both charging and discharging, aiding our understanding of system behavior. Our practical study analyzed a commercial hot water storage tank, emphasizing the critical role of accurate temperature measurements at specific points within the system. The sensor output directly impacted HP's COP, while the upper tank sensor influenced heat pump activation decisions. We performed a total of four tests, two during the charging phase and two during the discharging phase, and these tests successfully forecasted temperature fluctuations in different areas of the tank.

3.3 Heat Pump

Reversible heat pumps have the capacity to fulfill the space heating, space cooling, and domestic hot water requirements of buildings without producing local pollutants. They can harness renewable heat from the air, water, and ground, making them a promising technology with the potential to play a significant role, even in regions with more challenging climates [131]. Various types of heat pumps are examined, each being characterized by its unique heat source and method of heat distribution. Notably, the water source heat pump is recognized for its exceptional energy efficiency. A water-to-water heat pump (WWHP) functions by transferring heat between two water streams, one serving as the heat source and the other as the heat sink. In essence, it operates on the fundamental principles of traditional heat pumps, but it employs water as the medium for heat exchange. Consequently, it harnesses the heat energy contained within water to offer both heating and cooling capabilities. Remarkably, suitable water sources encompass groundwater, industrial cooling water, pre-chilled process water, and even sewage water. In fact, rivers and seawater can also serve as heat sources. This makes WWHPs incredibly versatile, catering to both heating and cooling requirements. During heating mode, they extract heat from the water source and channel it into the heating system. Conversely, in cooling mode, the heat pump reverses its operation, extracting heat from the building and releasing it into the water source. This versatility sets the WWHP apart, excelling in both cooling and heating tasks, thereby optimizing energy utilization. A WWHP comprises three key components: the evaporator, compressor, and condenser. The evaporator's role is to extract heat from a water source by circulating a refrigerant through coils. As the refrigerant evaporates, it absorbs heat from the water source, causing the water temperature to decrease. The vaporized refrigerant is then compressed by a compressor, raising both its temperature and pressure. In its transformed state as a high-temperature, high-pressure refrigerant, it passes through a condenser where it transfers its heat to another water distribution system. In the condenser, the refrigerant releases heat into the second water flow, which is subsequently employed for heating. As the refrigerant releases its heat, it condenses back into a liquid state, ready to initiate the process once more. When cooling is required, the WWHP functions similarly but in reverse order: condensation, compression, and evaporation.

WWHPs are recognized for their high energy efficiency. High COPs can be achieved by WWHPs, contributing to a reduction in energy consumption and a lowering of utility bills. When compared to other alternatives, such as air-based heat pumps, WWHPs typically present a higher level of

efficiency. Consequently, COPs in the range of 2.8 to 4 are typically observed in the context of WWHPs. However, these values are contingent on the temperature difference between the heat source and the heat sink, with a warmer heat source and a colder heat sink resulting in higher heat output and efficiency [132]. As a means of integrating renewable energy, WWHP are employed, allowing for the optimization of clean, sustainable energy utilization. In this capacity, the constant temperature of the water source can be harnessed without dependence on fossil fuels, resulting in a reduction in greenhouse gas emissions. Thus, they are deemed a viable option in the effort to expedite progress towards achieving net zero carbon emissions. Therefore, the benefits of WWHP are numerous, encompassing cost-effectiveness, quiet operation, dependable performance, and energy recovery [133].

As it discussed earlier, the essence of MPC lies in its ability to use a model to predict the system's future behavior and adjust control inputs accordingly to achieve desired outcomes. The HP plays a cardinal role in regulating the building's temperature, making it crucial for any control strategy to have a profound understanding of its dynamics. However, capturing the complexities of a HP's operations is not always straightforward, given its nonlinear characteristics and dependencies on various external and internal conditions.

Given this backdrop, a "state machine" approach for modeling the HP was already proposed and implemented by Eurac Research employees. State machines, by their design, offer a structured yet flexible way to capture the various operational modes and transitions of a system. For a component as versatile as the HP, which can operate under different modes (e.g., heating, cooling, standby) and transition between them based on specific criteria (e.g., temperature thresholds, demand), the state machine approach seems apt.

A state machine is often described as a conceptual tool used to represent the different states of a system and the transitions between these states. In the context of system design and control, state machines are commonly employed to capture the behavior of systems that can exist in different conditions or modes. At the heart of how a state machine operates are the distinct conditions in which a system can exist, known as states. Each of these conditions is identified and defined clearly. These states are interconnected by movements called transitions. Specific criteria or triggers, which when met, cause these transitions to occur, allowing the system to shift from one state to another. Every state machine starts with an initial condition or state, which is the condition in which the system is found when first activated or initialized. In some machines, there might be

a specific condition that marks the end or completion of its process, referred to as the final state[134] . Taking a simple example, a light bulb can be in two states: "Off" or "On". The act of flipping a switch can be seen as a transition that moves the bulb between these two states.

One of the primary advantages of state machines is the simplicity and clarity they bring. By breaking down a system's behavior into well-defined states and transitions, its operation becomes easier to understand [135]. This clarity is coupled with flexibility; as the system evolves or its requirements change, new states or transitions can be added without needing to redesign the entire system. Furthermore, they offer a degree of predictability; if one knows the current state of a system, its future behavior can be anticipated based on the defined transitions. This predictability also aids in error handling. Unwanted or unexpected conditions can be detected when the system enters states that aren't defined or when illegal transitions are attempted [136]. Lastly, state machines have the advantage of reusability [137]. Once designed for a specific system, the same state machine framework can often be adapted or reused for other similar applications.

In [138] authors use a state machine to model the start-up and shut-down sequences of a heat pump. The state machine has four states: Off, On, Heating, and Cooling. The transitions between states are triggered by events such as the thermostat being turned on or off, the pressure switch being activated, or the temperature of the heat pump reaching a certain threshold. In [139] authors also use a state machine to model the heating process of a building. The state machine has three states: Off, Heating, and Cooling. The transitions between states are triggered by events such as the temperature of the building dropping below a certain threshold, or the temperature of the building rising above a certain threshold.

3.3.1 HP state machine model

In Figure 3-44 (a), the state machine corresponding to the HP is depicted (As mentioned before, the model was already available in Eurac Research). This model represents any single-stage heat pump, where the fluid at the load and source sides is defined based on the thermal properties of the respective fluids, such as air or water. Figure 3-44 (b) also is an example how transition works. The state machine is designed to mimic the ramps depicted in the Figure 3-44 (b), serving as an illustrative example for better understanding.



Figure 3-44. State machine of HP

The state machine for the designed heat pump consists of 10 distinct discrete states, with two fundamental states related to operational modes: heating and cooling. The other 8 states predominantly relate to the operation of the compressor and its various stages. It should be noted that the modulation of the compressor is determined by the inlet temperature at the load side of the heat pump and a specified setpoint temperature.

IDLE (Stand-by): In this state, the heat pump is not entirely shut off. Instead, it consumes a minimal amount of energy for peripheral activities within the unit. While it doesn't actively cool or heat, the system remains primed for prompt activation.

Warm_up: it primarily serves as a preliminary stage. Upon entering this state, the compressor is introduced into the circuit, not at its maximum speed, but it initiates operations at its minimum speed. This is essential as, before ramping up and tracking the load, the heat pump should remain at this minimum speed.

Stable_min: In this state, the compressor operates at its minimum speed, delivering the necessary thermal power or temperature level to meet the current load without requiring any escalation.

Ramp_up: In the Ramp_up state, the speed of the compressor is incrementally increased.

Stable_PL: This denotes a 'Stable Part Load' state where the compressor operates at a speed between its minimum and maximum thresholds.

Stable_max: The compressor is operating at its peak capacity during this state.

Ramp_down: A reduction in the compressor's speed is observed in this state.

Cool_down: In this state, prior to transitioning to the IDLE, the compressor operates at its minimum, similar to the warm-up state. The system hasn't fully transitioned to IDLE yet. The behavior of the state machine can be mathematically characterized by defining the transitions between states based on various parameters. Before delving into specifics, symbolic representations and their corresponding definitions are presented. It's noteworthy to mention that the logic of the state machine compares inputs and determines subsequent states, highlighting the essential inputs required for the model.

- τ_{idle} indicating the duration, the system has been in the IDLE.
- τ_{warm_up} indicates the time duration the compressor has been in the Warm_up state.
- T_{inlet_load} denotes the current inlet load temperature.
- T_{set_heat} stands for the temperature setpoint for the heating mode.
- T_{set_cool} represents the temperature setpoint for the cooling mode.

- ϵ is the temperature margin, which is 0.5°C.
- ω signifies the current speed of the compressor.
- τ_{cool_down} measures the duration in the Cool_down state.
- $\tau_{warmup,min}$, $\tau_{idle,min}$, and $\tau_{cool_down,min}$ represent the minimum duration thresholds for their respective states.

These symbols primarily encompass various timers that monitor the duration a specific state is active, the inlet load temperature, which is pivotal for decision-making processes in state transitions, setpoints that define target temperatures for different operational modes, a margin value providing a temperature buffer, and details about the compressor's operational speed. Each of these notations acts as a cornerstone to understand and dictate the nuanced behavior and state transitions of the heat pump, ensuring it operates optimally and responds properly to varying conditions.

Now, discussing transitions and their conditions:

1.
2. ...
3. ...
4. ...
5. ...
6. ...
7. ...
8. ...
9. ...
10.
11. ...
12. ...
13. ...
14. ...
15. ...
16. ...
17. ...

18. ...

19. ...

20.

1. **Speed (ω):** Represents the current operational speed of the compressor, which is instrumental in regulating the heat transfer capacity of the HP. The speed of the compressor is generally expressed in normalized revolutions per minute (RPM).
2. **Heat Energy Delivered (Q_{th}):** This metric quantifies the amount of thermal power transferred to the load, giving a direct insight into the HP's heating or cooling efficacy. Typically measured in Watt (W) or kilowatt (kW).
3. **Electrical Energy Consumed (W_{el}):** By monitoring the power intake, we can gauge the system's demand on the power grid and assess its operational cost. This is usually measured in Watt (W) or kilowatt (kW).
4. **Coefficient of Performance (COP):** A pivotal measure, COP provides a ratio of the heat energy delivered to the electrical energy consumed, thus serving as a benchmark for the HP's efficiency. COP is a ratio, so it doesn't have a unit. It's the amount of heat energy delivered divided by the electrical energy consumed.
5. **Mass Flow Rate from Load Side (\dot{m}_{load}):** This indicates the volume or mass of the operating fluid at the load side flowing through the HP's load side, reflecting the system's cooling, or heating load. Generally quantified in kilograms per second (kg/s) or kilograms per hour (kg/h), depending on the capacity and size of the system.
6. **Mass Flow Rate from Source Side (\dot{m}_{source}):** Correspondingly, this measures load side mass flow rate on the source side, showing the heat source's contribution. This is usually expressed in kilograms per second (kg/s) or kilograms per hour (kg/h).
7. **Outlet Temperature from Load Side ($T_{out,load}$):** A vital metric for user comfort and safety, it indicates the temperature of the fluid as it exits the HP, moving towards the conditioned space. Temperature is typically given in degrees Celsius ($^{\circ}\text{C}$) or Kelvin (K).
8. **Outlet Temperature from Source Side ($T_{out,source}$):** This reflects the temperature of the fluid after it has extracted or dumped heat to the external environment or heat source. Temperature is typically given in degrees Celsius ($^{\circ}\text{C}$) or Kelvin (K).

Among these outputs, the COP stands out as particularly significant. The COP is defined by Eq. (3.41).

$$COP = \frac{Q_{th}}{W_{el}} \quad (3.41)$$

Where Q_{th} is the thermal power delivered or extracted by the HP and W_{el} is the electrical power consumed by the HP.

In the proposed model, a regression analysis is employed to compute values for Q_{th} and W_{el} . This analysis is rooted in a performance map crafted from data sourced either from real-time monitoring or rigorous laboratory tests. This map pairs specific combinations of input parameters - such as the compressor's speed, inlet temperatures from both the load and source sides, and mass flow rates - with their corresponding outputs, notably Q_{th} and W_{el} . By leveraging non-linear regression techniques, the most fitting curve to represent these relationships is derived. Hence, when the system encounters specific inputs, it refers to this curve to predict the likely outputs, ensuring the model remains attuned to previously observed patterns and behaviors.

3.4 Optimization

Optimization is the process of making something better or more effective based on certain criteria or constraints. In the context of mathematics and engineering, optimization is about finding the best solution from a set of feasible solutions. Optimization problems can vary in complexity and can be found in a multitude of disciplines, from economics to engineering, and from machine learning to logistics. The importance of optimization cannot be overstated. In a world filled with limited resources and endless possibilities, optimization provides the tools and techniques to maximize or minimize desired quantities. It could be about reducing costs, increasing profits, minimizing errors, or maximizing throughput. By framing problems in terms of optimization, it's possible to leverage powerful algorithms and mathematical tools to find solutions that would be unattainable or highly time-consuming through intuition or trial and error alone. As it mentioned earlier, MPC is a type of control strategy that employs a model of the system to predict its future behavior. What truly distinguishes MPC from other control strategies is its inherent reliance on optimization at every control step. Through optimization, MPC ensures the system's performance closely adheres to desired setpoints or trajectories, even when considering constraints. This continual recalibration of the optimal control input based on the latest information allows MPC to achieve a level of performance that is challenging to match with traditional control methods MPC

is a powerful control strategy that can handle constraints on both the control inputs and the states of the system. By formulating the control problem as an optimization problem, MPC can ensure that these constraints are consistently respected. This is crucial in systems where safety or operational boundaries cannot be compromised [140].

Moreover, the combination of MPC with optimization endows the control strategy with a flexibility that's hard to find elsewhere. MPC can adapt readily to changes within the system or its external environment, making it an invaluable tool for non-linear, time-varying, or uncertain systems [141], [142]. As a result, it frequently leads to reduced operational costs by making optimal control decisions, often resulting in minimized energy consumption or decreased wear and tear. This not only makes systems more efficient but also adds to their effectiveness.

Also, the predictive nature of MPC, when paired with optimization, offers a layer of reliability to systems [143]. By continuously monitoring and adjusting based on the predicted behavior, MPC ensures that systems operate within safe and reliable boundaries, effectively mitigating the chances of unforeseen events or system failures.

In essence, optimization serves as the lifeblood of MPC. It equips MPC with the tools necessary to make informed, forward-looking decisions that boost the performance, reliability, and efficiency of systems. As technology continues to evolve, the synergy between MPC and optimization remains pivotal in tapping into the maximum potential of our systems in the most optimal manner. As discussed in section 2.2, district heating networks play a pivotal role in delivering efficient and sustainable energy solutions. Within this framework, substations form a crucial nexus point, especially when integrating advanced systems like HP and TES. Given the dynamic nature of energy demands and supply conditions, managing these systems requires a strategy that is both adaptable and future-facing. This is where MPC becomes invaluable. At the heart of this is the optimization capability of MPC. Consider the HP, which can draw power from either PV panels or the electrical grid. To operate this HP most efficiently, one needs to decide the optimal source of power at any given time. Factors influencing this decision include current solar irradiance (affecting PV output), grid electricity prices, and anticipated energy demand. The cost variability of the electrical grid introduces a unique challenge. It's advantageous to tap into the grid during periods of low pricing. Yet, predicting these periods requires knowledge of future electricity prices, demand profiles, local weather conditions affecting PV output, and the state of the TES. The predictive nature of MPC thrives in such environments. By leveraging models that forecast

these variables, MPC can anticipate the best times to use grid electricity versus stored or solar-generated energy. This not only ensures optimal performance of the HP but also leads to economic benefits by capitalizing on lower grid prices.

Furthermore, integrating TES into the mix amplifies the importance of MPC. TES systems store excess heat for future use, acting as a buffer against demand fluctuations. Utilizing mathematical models that describe the behavior and dynamics of the TES, MPC can determine the optimal times for charging or discharging based on the system's current state, predicted heating demands, and other influencing variables. This precise modeling and the predictive capability of MPC together foster a synergistic relationship between the HP and TES. Under the guidance of MPC, both systems cooperate to ensure that energy is both utilized and stored in the most efficient manner, optimizing both energy usage and cost.

3.4.1 Dynamic programming

Dynamic programming (DP) is a powerful mathematical and computational technique used to solve problems by breaking them down into simpler subproblems. It is particularly effective for optimization problems, where the goal is to find the best solution among a set of feasible solutions. At its core, DP addresses the challenge of large, complex problems by decomposing them in a way that avoids redundant work and accelerates problem-solving. The name "dynamic programming" might be misleading as it doesn't directly refer to "programming" in the context of writing computer code. Instead, it refers to a systematic procedure or "program" to solve a problem. Introduced by Richard Bellman in the 1950s [144], The technique is built upon the concept of optimal substructure, meaning that an optimal solution to the problem can be derived from optimal solutions to its subproblems.

A characteristic feature of DP is the use of a table to store solutions to subproblems, ensuring that each subproblem is solved only once. This concept, known as "memorization," reduces the computational effort by retrieving stored solutions rather than recalculating them [145]. In essence, DP is a blend of recursion and iterative problem-solving, optimizing the process to tackle complex problems with increased efficiency. It has found applications in numerous fields, from economics to bioinformatics, and from computer science to operations research and energy, serving as a testament to its versatility and power.

DP emerges as a pivotal tool in [146], bolstering the efficiency and user comfort of the HVAC system. Through DP, the study adeptly frames HVAC control as a constrained optimization

challenge, ensuring intelligent decision-making to strike a balance between comfort, preferences, and energy costs. A novel feature, the 'thermal energy storage in building', is introduced to circumvent a challenge in DP's typical reliance on historical state data. When this approach is applied, not only does the system optimize operations based on room temperature and the remaining start hours of the Primary Air Unit, but it also substantially outperforms existing expert rules. Specifically, compared to a standard rule maintaining a 20°C room temperature, the method guided by DP realizes a remarkable 35.1% reduction in energy and emissions, all while preserving comfort. This highlights the transformative role of DP in refining HVAC system controls.

DP was used in [147] to find the best way to balance electricity use, costs, and comfort. A smart move in the study is using a simplified thermal model with DP. This helps because traditional DP sometimes struggles to get indoor temperatures right, especially when considering things like how long warmth stays in a room. When they put their DP method to the test, it did better than other common methods. For example, when compared to another method using EnergyPlus to guess indoor temperatures, the DP method did better, even with its simpler approach. This shows how DP can be a game-changer in making HVAC systems work better, leading to savings and more comfort.

In [148], a study conducted on pharmaceutical industry buildings in Southern Germany, DP was employed to optimize the cooling demands met by their chilled water plant. Given the increasing cooling loads, the study evaluated whether to add a chiller or introduce a chilled water TES system. The optimization, rooted in DP, focused on refining the TES system's charge/discharge strategy, and was paired with mixed integer programming for individual chiller dispatch. Results indicated that by adopting a TES system, not only would there be a significant cost savings — with investments being recouped within three to six years — but also operational benefits like improved system reliability and the ability to bypass less efficient chillers in favor of more effective ones.

From its foundational principles to its practical applications, it's clear that DP is more than just a theoretical tool—it's a driving force behind many innovative solutions, especially in the realm of HVAC systems. The studies outlined above underscore DP's ability to bridge the gap between theoretical optimization and tangible energy savings and user comfort.

In this thesis, DP was utilized for optimization, building upon a model previously developed at Eurac Research by another researcher.

3.4.1.1 DP mathematical framework

Consider a scenario in which a transition from state $\mathbf{x}(t)$ at time t through the control $\mathbf{u}(t)$ incurs an instantaneous cost given by $\mathcal{L}[\mathbf{x}(t), \mathbf{u}(t), t]$. The total cost over a finite horizon of $N + 1$ points starting at time t_0 to concluding at time $t_0 + N$ can be represented as (3.42).

$$J = \sum_{t=t_0}^{t_0+N} \mathcal{L}[\mathbf{x}(t), \mathbf{u}(t), t] \quad 3.42$$

A sequence of controls $\mathbf{u}(t)$ exists that minimizes J as described in (3.43) and (3.44).

$$V(\mathbf{x}_0, t_0, N) = \min_{\mathbf{u}(t) \in \mathbf{U}, t=t_0, \dots, t_0+N} \left\{ \sum_{t=t_0}^{t_0+N} \mathcal{L}[\mathbf{x}(t), \mathbf{u}(t), t] \right\} \quad 3.43$$

subject to

$$\mathbf{x}(t + 1) = \mathbf{f}(\mathbf{x}(t), \mathbf{u}(t), t), \forall t \in \{t_0, \dots, t_0 + N - 1\} \quad 3.44$$

In Eq. (3.43) $\mathbf{U} \subseteq \mathbb{R}^m$ is a space where the control action belongs to. Similarly, $\mathbf{X} \subseteq \mathbb{R}^n$ will denote the space where the state variables are bounded to. Given our state vector and control vector, the next state vector is determined by the equation Eq. (3.44) where \mathbf{f} is a vector-valued function mapping vectors of the state space \mathbf{X} , vectors of the input space \mathbf{U} and the time t to a vector in \mathbf{X} . For any initial state vector and time, our optimal control sequence is governed by the Bellman equation which is represented in Eq. (3.45).

$$V(\mathbf{x}(t), t, N) = \min_{\mathbf{u} \in \mathbf{U}} \{ \mathcal{L}[\mathbf{x}(t), \mathbf{u}(t), t] + V(\mathbf{f}(\mathbf{x}(t), \mathbf{u}(t), t), t + 1, N - 1) \} \quad 3.45$$

Consequently, an iterative formula was identified that can be used to establish $V(\mathbf{x}(t), t, N)$ for every $\mathbf{x}_k \in \mathbf{X}$, with \mathbf{X} being the collection of permissible states.

In summary, the least expense at state $\mathbf{x}(t)$ and step t over a horizon of $N + 1$ points, $V(\mathbf{x}(t), t, N)$, is determined by minimizing the combined cost of the current step t and the minimal expense to reach the process's end from the subsequent state at step $t + 1$ ($V(\mathbf{x}(t + 1), t + 1, N - 1)$). This mirrors Bellman's Principle of Optimality.

It should be noticed that in this thesis, the DP optimization approach has been utilized, which was previously developed and made available by colleagues at Eurac Research.

3.5 Integration of substation

In this thesis, the primary focus is placed on the conditions at the decentralized substation rather than on the internal dynamics of the DH network itself. Consequently, details concerning the

production of heat within the DH network and other internal processes are not considered within the scope of this research. The primary objective is to assess how the temperature and mass flow rate from the DH network influence the performance of the integrated substation and the MPC. The critical parameters for this system include the temperature and mass flow rate of the water entering the decentralized substation.

This research considers four different types of schemes for connecting the DH to the decentralized substation. Each of these connections occurs under certain conditions, which will be discussed in detail. These schemes are designed to enhance the effectiveness and efficiency of substations, ensuring optimal performance under various scenarios.

Figure 3-45 illustrates scheme 1, which depicts the initial configuration for connecting the DH network to the substation.



Figure 3-45 Schematic diagram of scheme 1

In this scheme, the configuration and operation of the DH network rely on specific temperature conditions to ensure optimal performance. For scheme 1 to be viable, the following temperature relationships must be satisfied, as presented in Eq. (3.46).

$$\dots \tag{3.46}$$

Here, T_{in_max} represents the maximum inlet temperature at the source side (evaporator) of the WWHP. Efficient operation of the heat pump is ensured without exceeding the thermal limits set by the manufacturer, who specifies $T_{in_max} = 55 \text{ }^\circ\text{C}$.

T_{ret_TES} is the temperature of the water returning from TES to the load side (condenser) of the HP. T_{DH} denotes the temperature of the water in the district heating supply.

In Figure 3-46, which presents scheme 2, the process is triggered when T_{DH} exceeds When T_{DH} surpasses ... can be utilized to feed the HP condenser, leading to higher efficiency. Thus, in scheme 2, modifying the connection between the district heating system and the heat pump enhances overall efficiency. Equation 3.47 illustrates the conditions necessary for transitioning to scheme 2.

$$\dots \tag{3.47}$$



Figure 3-46. Schematic diagram of scheme 2

Figure 3-47 illustrates scheme 3. In this scheme, when T_{DH} exceeds the ..., feeding the heat pump directly is not feasible due to safety concerns and limitation of Consequently... is connected to the source side of the heat pump (evaporator), while the load side of the heat pump (condenser) is supplied by DH. Equation 3.48 outlines the conditions under which the transition to scheme 3 occurs:

$$\dots \tag{3.48}$$



Figure 3-47. Schematic diagram of scheme 3

In scheme 4, when the district heating temperature exceeds ..., the heat pump does not need to be activated. Instead, the district heating is directly connected to the TES. This process is described by Equation (3.49):

$$\dots \tag{3.49}$$



Figure 3-48. Schematic diagram of scheme 4

Therefore, based on ... different operational schemes can be switched to achieve the highest system efficiency.

The substation is managed through four different operational schemes, each with its own specific criteria for transitioning between them. To ensure smooth and efficient transitions, a hysteresis structure is employed. Hysteresis helps prevent frequent switching between schemes by defining upper and lower thresholds (dead bands) for each temperature variable. By adjusting to the most suitable scheme according to these temperature variables, the system's optimal performance and energy use are ensured.

In the substation, five different hysteresis mechanisms have been considered: HA, HMa, HMb, HMc, and HMd. These hysteresis controls are crucial for managing the transitions between different operational schemes. Each hysteresis serves a specific purpose, regulating various aspects of the heating process based on the state of the temperature variables.

The “HA” hysteresis is specifically used for the activation and deactivation of HP. As shown in Figure 3-49, sensor activation is exactly at sensor top, as described in Figure 3-30 and Table 3-3. Sensor deactivation is slightly above sensor bot.



Figure 3-49. Position of sensor activation and deactivation within the tank

For activation of the HP:

- When the temperature difference between the top temperature sensor of TES ($T_{sens,top}$) and the set point temperature ($T_{set,TES}$) is less than the upper hysteresis threshold (HA_{UP}), the value of HA is set to 0. This indicates that the heat pump should be activated to increase the temperature.

For deactivation of HP:

- When the temperature difference between the deactivation temperature sensor ($T_{sens,deactivation}$) and the set point temperature ($T_{set,TES}$) is greater than the lower hysteresis threshold (HA_{LW}), the value of HA is set to 1. This means that the heat pump should be turned off to prevent overheating.

Important note: In typical hysteresis control systems, a value of 1 indicates the system is ON, while a value of 0 indicates it is OFF. However, in this thesis, the hysteresis control labeled as HA is operated in the opposite manner. This means that when the temperature reaches the upper threshold, the heat pump CS is 1 and means OFF. Conversely, when the temperature drops below the lower threshold, the heat pump CS is 0 and it turns ON.

Equation. (3.50) represents the control signal (CS) status of HP, indicating its activation and deactivation based on the sensed temperatures and setpoint differential.

$$CS_{HP} = \dots \quad 3.50)$$

The thresholds for HA_{UP} and HA_{LW} are set at -5°C and $+5^{\circ}\text{C}$ respectively. This hysteresis structure helps maintain a stable temperature within the system, avoiding rapid cycling that can lead to inefficiencies and increased wear on the heat pump and also letting TES to have lengthy cycle of charge and discharge. Figure 3-50 represents how hysteresis HA is working (the values shown are dummy data).



Figure 3-50. Example of the performance of hysteresis HA

The conditions for the HA hysteresis are described in Table 3-5.

Table 3-5. Conditions for HP Activation and Deactivation Based on HA Hysteresis

	HA	NOT (HA)
...
...

Besides having two sensors for activation and deactivation, the option of using only one sensor for both the activation and deactivation of the HP was also considered. In this scenario, as shown in Eq. (3.51), $T_{sens,top}$ is responsible for the control signal. Therefore, the control logic is as follows:

$$CS_{HP} = \begin{cases} \dots & \dots \\ \dots & \dots \\ \dots & \dots \end{cases} \quad (3.51)$$

HMa is the hysteresis control mechanism for managing the substation based on the temperature difference between T_{DH} and The conditions for the HMa hysteresis are described in Table 3-6. The thresholds for HMa_{UP} and HMa_{LW} are set at 0°C and -5°C, respectively. ... also is set to 60 °C.

Table 3-6. Condition for activation and deactivation of HMa

	HMa	NOT (HMa)
...
...

HMb is the hysteresis control mechanism used to regulate the substation by monitoring the T_{DH} and $T_{ret,TES}$. The thresholds for HMb_{UP} and HMb_{LW} are set at 2°C and -2°C respectively. The conditions for the HMb hysteresis are described in Table 3-7.

Table 3-7. Condition for activation and deactivation of HMb

	HMb	NOT (HMb)
...
...

The HMc hysteresis control mechanism is employed to regulate the substation by monitoring the temperature difference between The thresholds for HM_{cUP} and HM_{cLW} are set at 0°C and -5°C, respectively. The conditions for the HMc hysteresis are described in Table 3-8.

Table 3-8. Condition for activation and deactivation of HMc

	HMc	NOT (HMc)
...
...

The hysteresis control identified as HMd is essential for regulating the substation by evaluating the temperature difference between ... and With thresholds set at 0°C for HM_{dUP} and -5°C for HM_{dLW} , it ensures efficient system operation. The specific conditions for the HMd hysteresis are detailed in Table 3-9.

Table 3-9. Condition for activation and deactivation of HMd

	HMd	NOT (HMd)
...
...

With five different hysteresis mechanisms involved, there are 32 possible cases at each step. All 32 cases are described in Appendix 2. However, only one case can be active (represented by 1) at any given time, while the remaining cases are inactive (represented by 0). Table 3-10 summarizes the conditions required for the substation to be in each of the four schemes. Each scheme is defined by the activation or deactivation of specific hysteresis mechanisms.

Table 3-10. Conditions for Transition Between Different schemes

Scheme	Conditions
...	...
...	...
...	...
...	...

A set point temperature of 55°C was established for the user side. A constant ΔT of 10°C was also considered for the load side. A mixing valve was used to cool down the return temperature from the building. If the temperature of the water in the tank sent to the building exceeds 55°C, the water is recirculated to maintain the desired temperature.

In this thesis, the mass flow rate in the substation is considered a constant value, though it depends on the specific scheme used. Generally, the load side of the HP is considered to have a mass flow rate of 3.5 m³/h. However, the source side varies depending on the scheme. For schemes 1 and 2, the mass flow rate on the source side of the HP is 80% of the mass flow rate on the load side. In contrast, for schemes 3 and 4, the mass flow rate on the source side is the same as that on the load side.

As presented in Figure 3-45 to Figure 3-48 , the mass flow rate in the DH system varies according to the scheme implemented. In scheme 1, the DH mass flow rate is the same as the source side of the HP. Once scheme 2 is in use, as depicted in Figure 3-46, the DH mass flow rate becomes the summation of the mass flow rate of both the source and load sides of the HP. In schemes 3 and 4, the DH mass flow rate matches the load side of the HP. Table 3-11 presents the mass flow rate values for the different schemes of substation.

Table 3-11. mass flow rate in the substation and DH [m³/h]

	DH	Source side of HP	Load side of HP
...
...
...
...

Chapter 4

4 Results and Discussion

In this section, the substation integration is performed, and the MPC is executed. The resulting outcomes are subsequently discussed. As illustrated in Figure 1-1, the 5GDHC showcases the integration of a district heating network with a residential building. On the left side, the 5GDHC network operates at lower temperatures that are not useful for direct heating purposes. At the center, a decentralized substation is depicted, containing HP and TES. On the right side, a residential building is shown, which benefits from the thermal energy supplied by the substation for space heating (SH) and domestic hot water (DHW).

The load specifications are provided for a reference building, which is a small multi-family house. This building consists of five floors, with two dwelling units per floor, each unit having an area of 50 m². In total, the building covers an area of 500 m². Located in Stuttgart, the building has been renovated to improve energy efficiency. The space heating demand for the building is specified to be 70 kWh per square meter per year. This demand profile is crucial in evaluating the performance of the integrated substation and the effectiveness of the MPC implementation.

4.1 Simulation campaign for performance analysis of the developed substation

To thoroughly analyze the performance of the developed substation, an extensive simulation campaign was conducted during the first week of December. During this campaign, a variety of district heating temperatures were tested to determine their impact on system efficiency and effectiveness. Additionally, different sizes of TES units were considered to evaluate how the storage capacity influences the overall performance of the substation. Various setpoints for the TES were also explored to understand how different operational parameters affect the system's stability and efficiency. The effect on the user-side delivered temperature was also examined. This comprehensive approach ensured that all relevant factors were taken into account, providing a detailed understanding of the substation's performance under diverse conditions. For the DH temperature, two constant values were considered: 30°C and 50°C. For the thermal TES, three different capacities were evaluated: 1 m³, 2 m³, and 3 m³. Regarding the setpoints of the TES, three

temperature values were examined: 55°C, 60°C, and 65°C. Table 4-1 presents the combinations of tests conducted for the different parameters and values considered in the simulation campaign.

Table 4-1. Parameters and Values Considered in the Simulation Campaign

Test number	T _{DH} (°C)	Tank size (m ³)	Set point (°C)
1	30	1	55
2	50	1	55
3	30	2	55
4	50	2	55
5	30	3	55
6	50	3	55
7	30	1	60
8	50	1	60
9	30	2	60
10	50	2	60
11	30	3	60
12	50	3	60
13	30	1	65
14	50	1	65
15	30	2	65
16	50	2	65
17	30	3	65
18	50	3	65

The size of our HP is 35 kW, and it has been carefully sized to effectively fulfill the heating load requirements. The heat pump tested in this study is a high-temperature model capable of producing output temperatures up to 80°C.

Figure 4-1 shows temperature ranges for top of the tank and user-side temperature stability across various combinations of (setpoint, tank size and DH temperature).

The x-axis labels depict various combinations as specified in Table 4-1. For the lower DH temperature (30°C, highlighted in blue), it is noted that the temperature range increases in correlation with both the TES setpoint and capacity. This trend suggests that as the TES setpoint

and capacity rise, the system's output temperature also escalates. Similarly, for the higher DH temperature (50°C, highlighted in pink), the same pattern emerges, where higher TES setpoints and capacities result in increased temperature ranges. In the lower plot (second subplot), it is consistently shown that the delivered temperature to the user remains stable across all examined combinations. This stability signifies that the substation is adept at maintaining a uniform user-side temperature, ensuring dependable performance regardless of the specific operational conditions. Additionally, the analysis reveals that larger TES units and higher setpoints significantly boost output temperatures. Consequently, the system demonstrates its ability to provide stable and reliable temperatures to the user, affirming its effectiveness under various conditions. Outliers in this figure have been excluded for clarity.



Figure 4-1. Temperature Ranges for top of the tank and User-Side Temperature Stability Across Various Combinations of (setpoint, tank size and DH temperature). Outliers Removed.

Figure 4-2 represents the performance of the HP_{ON} a minute-by-minute basis and the substation operational mode scheme. Additionally, electricity consumption and ON/OFF cycles have been investigated. In this analysis, the combinations of setpoints, tank sizes, and DH temperatures are indicated on the y-axis. The left side of the plot illustrates the HP performance, represented in gray, based on the total minutes of operation over one week for each test. It is also noted how much of this performance time was allocated to scheme 1 or scheme 2. According to figures and equations 3.46) to (3.49), it can be concluded that due to the DH temperature, transitioning to scheme 3 or scheme 4 is impossible. Specifically, when DH is set to 30°C, only scheme 1 is followed, as dictated by Eq. (3.46). This restriction highlights the influence of lower DH temperatures on the operational scheme selection. In general, it can be concluded that a higher DH temperature correlates with less HP operation time, while a lower DH temperature necessitates longer HP operation. This inverse relationship underscores the efficiency impact of DH temperature settings on HP performance. The HP's electricity consumption is displayed on the right side of the plot. Since electricity consumption is mainly related to HP performance, it can be observed that longer HP operation times result in higher electricity consumption. Additionally, the ON/OFF cycles of the HP are shown in blue. Each cycle represents the period from when the HP turns on to when it turns off. Generally, a higher DH temperature results in more ON/OFF cycles. When the DH temperature is lower, the HP needs to operate longer to reach the setpoint, thereby extending the operation time and reducing the number of ON/OFF cycles. Conversely, when the DH temperature is higher, the HP can quickly satisfy the setpoint, leading to an increased number of cycles compared to lower DH temperatures.

The analysis reveals several key points. The selection of operational schemes is heavily influenced by the DH temperature, with lower temperatures restricting the system to scheme 1. Higher DH temperatures reduce the HP operation time, enhancing overall efficiency. Electricity consumption is proportional to the duration of HP operation, with longer operation times leading to higher consumption. The number of ON/OFF cycles increases with higher DH temperatures, as the HP can more rapidly achieve the setpoint temperature. These insights highlight the importance of DH temperature settings to balance HP efficiency, electricity consumption, and operational stability.



Figure 4-2. Performance of HP minutely, operational schemes, electricity consumption, and ON/OFF cycles for one week.

Figure 4-3 represents the distribution of HP operation minutely by the hour of the day for various combinations of setpoints, tank sizes, and DH temperatures. The left y-axis displays the HP operating minutes, while the right y-axis shows the average thermal load in kWh. Each line corresponds to a specific combination of parameters as indicated in the legend. The black line with markers illustrates the average load curve. In examining the plot, it is observed that HP activity sharply increases in the early morning hours (around 4-6 AM), peaks during the morning (7-9 AM), and gradually declines towards the afternoon. A secondary peak occurs in the evening (5-7 PM), reflecting typical household heating demand patterns. This pattern suggests that the HP_{ON} curves closely follow the thermal load demand throughout the day, ensuring that the heating needs are met efficiently. The parameter combinations reveal that higher setpoints (e.g., 65°C) and larger tank sizes generally result in higher operation of HP during peak hours. This indicates that more frequent HP activation occurs with these settings, likely due to the need for maintaining higher temperatures and accommodating larger thermal storage.

Lower DH temperatures (30°C) necessitate longer HP operation times to reach the setpoint, resulting in increased HP_{ON} compared to higher DH temperatures (50°C). The average load curve mirrors the HP_{ON} times, reinforcing the correlation between HP operational patterns and overall thermal load demand. Combinations such as (60, 1, 30) and (65, 3, 30) show significant activity during this period, suggesting that higher setpoints, larger tank sizes and low DH temperature lead to increased operation of the HP to meet the system's requirements.



Figure 4-3. The “distribution of HP operation” by the hour of the day for various combinations

Figure 4-4 provides a comprehensive analysis of the HP system's performance by displaying both the coefficient of performance (COP) of the system (COP_{sys}) and the HP_{ON} times minutely categorized by scheme state.

The left image displays a box plot of COP_{sys} , representing the COP at the terminal between the HP and the TES. The box plot showcases the range and distribution of COP_{sys} across various setpoints and tank sizes and DH temperatures. Notably, the COP_{sys} values are higher when the system operates in scheme 2 compared to scheme 1. The median COP_{sys} values increase significantly when the system moves from scheme 1 to scheme 2, indicating improved performance. In the right image, the performance of the HP is illustrated based on operational minutes across different combinations. The gray bars represent the total HP activation in a minute basis, while the colored segments denote the distribution of these counts across various schemes. When the system operates exclusively in scheme 1, the average COP_{sys} ranges from approximately 2 to 5. However, when scheme 2 is engaged, the COP_{sys} experiences a significant increase, demonstrating enhanced efficiency.

The analysis further reveals that increasing the setpoint leads to a decrease in COP_{sys} . This phenomenon is attributed to the corresponding rise in tank temperature, which, according to Eq. (3.46) to (3.49), reduces the probability of the system remaining in scheme 2. The right image illustrates this effect, showing that higher setpoints result in more operational time in scheme 1, where the COP_{sys} is lower. Therefore, it can be concluded that by optimizing the DH temperature and setpoint levels to consistently meet the user setpoint, the system can be maintained in scheme 2 for longer durations. This optimization would allow the substation to operate more efficiently, as indicated by the higher COP_{sys} values in scheme 2.



Figure 4-4. A comprehensive analysis of the HP system's performance by displaying both the COP_{sys} and the HP_{ON} minutely categorized by scheme state.

Figure 4-5 illustrate the charging and discharging processes for different tank sizes (1 m³, 2 m³, and 3 m³) under various setpoint and DH temperature conditions. The plots with a pink background represent the charging periods, while the plots with a blue background depict the discharging periods. Each subplot shows the energy density distribution for a specific tank size and set of conditions, with medians indicated for each combination. In the charging periods (pink background), the energy density distributions reveal that larger tanks (e.g., 2 m³ and 3 m³) generally store more energy. For instance, the 1 m³ tank's energy density peaks around 12.89 kWh for the (55, 1, 30) combination, whereas the 2 m³ and 3 m³ tanks show peaks at 26.01 kWh and 39.34 kWh, respectively, for similar combinations. As the setpoint increases, the median energy stored also increases. For example, the median energy for the (65, 1, 30) combination in the 1 m³ tank reaches 20.11 kWh. This trend is consistent across all tank sizes, indicating that higher setpoints enhance the energy storage capacity of the system. During the discharging periods (blue background), the energy density distributions show that higher setpoints also lead to higher median energy utilization. For example, the 1 m³ tank discharges a median energy of 12.98 kWh for the (55, 1, 30) combination, while for the (65, 1, 30) combination, the median energy discharged is 19.99 kWh. This pattern is observed across all tank sizes, with the 2 m³ and 3 m³ tanks showing even higher medians. The distributions during the discharging periods are generally tighter than those during the charging periods, suggesting more consistent energy utilization. The key insights from these plots are that larger tanks and higher setpoints significantly improve the energy storage and discharge capacities of the TES. The charging periods exhibit greater variability in energy storage, while the discharging periods show more stable energy utilization. This consistency during discharging is crucial for maintaining a reliable energy supply to meet user demands. In conclusion, optimizing tank size and setpoints can significantly enhance the overall performance of the substation. Larger tanks provide greater storage capacity, while higher setpoints ensure that the system can efficiently store and utilize energy.



Figure 4-5. Charging and discharging processes for different tank sizes (1 m³, 2 m³, and 3 m³) under various setpoint and DH temperature conditions

Based on the extensive tests conducted across various important factors, several key insights have been gained regarding the performance and efficiency of the substation:

- **Tank Size Impact:** Larger tanks (e.g., 2 m³ and 3 m³) significantly enhance the system's ability to store and discharge energy efficiently. They provide higher median energy storage and more consistent energy utilization during discharge periods, indicating a clear benefit in scaling up tank sizes.
- **Setpoint Influence:** Higher setpoints contribute to increased energy storage capacity and improved system performance. However, they also introduce more variability during the charging periods and result in more frequent HP activation. Optimizing setpoints is crucial for balancing efficiency and stability.
- **Operational schemes:** The system's performance is highly dependent on the operational scheme. Scheme 1 tends to operate with lower COP_{sys} values (around 2 to 5), while scheme 2 demonstrates significantly higher COP_{sys} values, indicating better efficiency. Situation in which DH temperature is higher than return temperature from TES helps the system stay longer in scheme 2, further enhancing overall performance.
- **Charging and Discharging Consistency:** The discharging periods exhibit tighter distributions compared to charging periods, indicating more consistent energy utilization. This consistency is vital for reliable energy supply to meet user demands.
- **Effect of DH Temperature:** Lower DH temperatures require more frequent HP operations to maintain setpoints, reflecting higher energy demands. Higher DH temperatures reduce the frequency of HP operations, contributing to more stable and efficient system performance.

Therefore, our rule-based control (RBC) has been selected based on this system specification: tank size of 2 m³ and tank setpoint of 60°C. All the hysteresis settings are the same as those discussed above in section 3.5.

4.2 RBC vs. MPC

The objective of testing the MPC control described in this section is to compare its performance against a baseline, which involves a simulation under identical boundary conditions where the 5GDHC substation is managed using a rule-based control strategy.

The operating costs of the substation over the prediction horizon are minimized through an objective function, as represented by Eq. (4.1). These costs for a 5GDHC substation encompass the expenses for the electrical energy required to operate the heat pumps and hydraulic pumps, which are sourced from the grid.

$$J(t_j) = \sum_{j=k}^{k+N-1} C_{el}(t_j)W_{el,sys}(t_j) \quad 4.1)$$

In this equation, $C_{el}(t_j)$ represents the price of electrical energy [€/kWh] at time t_j . The cost of electricity can vary over time, so this function reflects the dynamic pricing of electricity during the prediction horizon. $W_{el,sys}$ is the total electrical consumption of substation [kWh] at time t_j . N is the length of the prediction horizon. This is the future time period over which the control actions are optimized. The controller predicts the system behavior and calculates the optimal control actions to minimize the objective function over this horizon. k denotes the present or current time step. The controller is at time t_k , and it is looking to optimize performance over the future time steps from k to $k + N - 1$.

The primary goal of the substation, controlled either by MPC or RBC, is to ensure that the user-side temperature remains at or above this threshold to ensure thermal comfort. Thermal discomfort occurs when the temperature on the user side of the system falls below a predefined threshold, in this case, 55°C. Mathematically, this can be expressed as Eq. (4.2).

$$Q_{th,disc} = \sum_{j=k}^{k+N-1} \max(0, Q_{required}(j) - Q_{supplied}(j)) \quad 4.2)$$

$Q_{required}(j)$ is the heating power required at time j to maintain 55°C. $Q_{supplied}(j)$ is the actual heating power supplied by the MPC at time j .

Note: As discussed in the previous section, the set point of the tank was initially considered to be 60°C. The primary reason for this choice was the hysteresis range of HA, which was set to [-5, 5]. Upon running the MPC, it was realized that this range was too broad, making it difficult for the

optimizer to properly optimize the substation. This issue is described in Appendix 1. Consequently, the decision was made to narrow this range to [0, 5]. As a result, the set point of the tank for RBC was adjusted to 55°C, aligning with the user temperature side which was also set to 55°C. This adjustment is crucial for accurately assessing the performance differences between MPC and RBC. For all tests, the setpoints considered in the search space of DP were 50, 55, 60, and 65°C.

Test 1: Performance assessment of MPC and RBC with constant electricity cost

In this test, the performance of MPC and RBC is compared while the cost of electricity is consistently maintained at a fixed rate of 0.3 €/kWh. To facilitate a controlled comparison of the two control strategies, this constant electricity cost is assumed for the entire duration of the test. The temperature of the district heating system is varied between 40°C and 55°C. The test is conducted over the first week of December.

Figure 4-6 displays the results of test 1. In the first subplot, the thermal load is illustrated, with the black line representing the actual measured values and the colorful crosses indicating predictions made every hour for the subsequent 24 hours. The overlapping prediction lines highlight the continuous nature of the forecasting process. The second subplot presents the chosen setpoints, with solid blue lines indicating RBC setpoints and solid red lines representing MPC optimal setpoints. The MPC setpoints are shown to be more dynamic compared to the RBC setpoints. This dynamism reflects MPC's ability to optimize setpoints in real-time, potentially leading to more efficient system performance. The dotted blue and red lines depict the temperature delivered to the user under RBC and MPC, respectively.

In the third subplot, the stored energy in the tank is depicted, with the blue line representing the performance of the RBC and the red line representing the performance of the MPC. The unit of measurement for the stored energy is kilowatt-hours (kWh).

The fourth subplot relates to the cumulative electricity cost of the substation. The cumulative cost under the RBC is shown by the blue line, while the cumulative cost under the MPC scheme is represented by the red line. The subplot demonstrates that the cumulative energy cost under MPC is generally lower than that under RBC, suggesting that MPC is more effective in minimizing energy consumption costs over time. This cost reduction is quantified at 7.44%.

Finally, the fifth subplot presents the temperature of the DH system, shown by the black line, and the COP of the system, represented by scatter points. The color of the scatter points indicates the

active control scheme, providing insights into the performance efficiency of the system under different control strategies.



Figure 4-6. Result of comparison the performance of MPC vs. RBC with constant electricity price (test 1)

Figure 4-7 represents the activation time of the HP under different schemes, providing a comparison between RBC and MPC. In this analysis, both the total HP_{ON} time and the number of ON/OFF cycles were evaluated to assess the performance and efficiency of each control. In RBC, the total activation time of the HP was recorded as 2495 minutes. Scheme 1 was predominantly utilized, accounting for 1753 minutes or 70.3% of the total HP_{ON} time. Scheme 2, in contrast, was active for 742 minutes, representing 29.7% of the total activation time. The number of ON/OFF cycles in the RBC was relatively low, with 38 cycles observed throughout the test period. In MPC, the total HP_{ON} time was slightly lower, at 2341 minutes. Scheme 1 was used, with an activation time of 1517 minutes, constituting 64.8% of the total HP_{ON} time. Scheme 2 also contributed significantly, with an activation time of 824 minutes, or 35.2% of the total. An increase in the frequency of ON/OFF cycles was observed in MPC, with 49 cycles recorded. It should also be noted that in the objective function, no constraints for ON/OFF cycles were considered.



Figure 4-7. Activation time of the HP in test 1

These results illustrate distinct operational characteristics between the RBC and MPC. In the RBC, HP operation was heavily concentrated in scheme 1, with fewer transitions to scheme 2. Conversely, the MPC exhibited a more balanced distribution of activation time between scheme 1 and scheme 2, coupled with a higher frequency of switching ON and OFF. Being more in scheme 2 provides the system with the opportunity to achieve greater efficiency.

Test 2: Performance assessment of MPC and RBC with time of use (TOU)

In Test 2, all conditions remain the same as in Test 1 except for the consideration of TOU pricing for electricity. A variable price is applied, with a rate of 0.15 €/kWh during off-peak hours (00:00 to 07:00) and 0.30 €/kWh for the rest of the day. Figure 4-8 shows the results of Test 2. As can be seen, in general, the MPC managed to reduce the total electricity cost by 6.7%.



Figure 4-8. Result of comparison the performance of MPC vs. RBC with TOU (test 2)

Figure 4-9. Activation time of the HP in test 2

Figure 4-9 illustrates the activation time of the HP across various schemes, facilitating a comparison between RBC and MPC. In the RBC, the HP was activated for a total of 2495 minutes. Scheme 1 dominated this period, being active for 1753 minutes, which accounts for 70.3% of the total HP_{ON} time. Scheme 2, on the other hand, was operational for 742 minutes, representing 29.7% of the total activation time. The number of ON/OFF cycles recorded in RBC was relatively low, with 38 cycles observed during the test period. In the MPC, the total HP_{ON} time was slightly reduced to 2372 minutes. Scheme 1 was again the primary scheme, with an activation time of 1413 minutes, constituting 59.6% of the total HP_{ON} time. Scheme 2 also contributed significantly, being active for 959 minutes or 40.4% of the total. There was an increase in the frequency of ON/OFF cycles in the MPC, with 50 cycles recorded.

When comparing the results of test 1 and test 2, it becomes evident that the total HP_{ON} time was not only reduced by the MPC, but it also had an increased likelihood of operating in scheme 2. The opportunity for MPC to spend more time in scheme 2 contributed to its enhanced efficiency. Besides, during the analysis, it was observed that the running time of the HP during the TOU period (from 00:00 to 07:00) increased by 9% in test 2 compared to test 1. This increase indicates that the MPC attempted to take advantage of the TOU incentives. The slight increase in the HP's operational time during the TOU period suggests that the MPC recognized and responded to the cost-saving opportunities presented by the TOU pricing. However, the marginal change also implies that the TOU pricing scheme may not have been sufficiently attractive to significantly influence the MPC's overall strategy. Despite this, it is noteworthy that the MPC did make an effort to optimize its performance based on the available incentives, demonstrating a level of responsiveness to dynamic pricing models. This responsiveness, even if limited, showcases the potential for further optimization and efficiency improvements under more compelling pricing schemes.

Test 3: Performance assessment of MPC and RBC with variable electricity price

In the evolving landscape of energy management, understanding how different control strategies perform under varying electricity prices is crucial. Test 3 aims to evaluate the performance of MPC and RBC when subjected to variable electricity pricing. In the previous tests, we considered constant electricity prices (Test 1) and TOU pricing (Test 2). However, real-world scenarios often

involve more dynamic pricing structures. Thus, it is essential to assess how these controllers adapt and perform when faced with fluctuating prices. Figure 4-10 illustrates the variable electricity price profile over a typical day, highlighting the complexity and challenges associated with managing energy costs effectively. It should be noted that the prices are hypothetical.



Figure 4-10. Electricity price in test 3

Figure 4-11 shows the results of the performance comparison between MPC and RBC under these variable pricing conditions. In general, MPC managed to reduce electricity costs by 21.7% compared to RBC, demonstrating its superior ability to optimize energy consumption in response to price fluctuations.



Figure 4-11. Result of comparison the performance of MPC vs. RBC with variable electricity price (test 3)

Figure 4-12 presents the activation time of the HP across different schemes, enabling a comparison between RBC and MPC. Under the RBC strategy, the total HP activation time amounted to 2495 minutes. The majority of this activation occurred under scheme 1, which was operational for 1753 minutes, accounting for 70.3% of the total HP_{ON} time. Scheme 2 was active for 742 minutes, representing 29.7% of the activation time. The RBC strategy exhibited a relatively low number of ON/OFF cycles, with 38 cycles recorded. In contrast, the MPC strategy demonstrated a different pattern. The total HP_{ON} time for MPC was 2374 minutes, showing a slight reduction compared to RBC. Scheme 1 was predominant, with an activation time of 1442 minutes, constituting 60.7% of the total HP_{ON} time. Scheme 2 contributed significantly with 932 minutes, making up 39.3% of the activation time. The MPC strategy resulted in a higher number of ON/OFF cycles, with 51 cycles observed during the test period.



Figure 4-12. Activation time of the HP in test 3

This comparison highlights that while the MPC strategy reduced the total HP activation time, it also increased the frequency of ON/OFF cycles. This indicates a more dynamic response to the variable electricity prices, potentially optimizing energy usage more effectively. The redistribution of activation times across different schemes in MPC, particularly the significant use of scheme 2, suggests a strategic adaptation to varying electricity prices to achieve cost efficiency. The analysis reveals that MPC not only managed to reduce the overall activation time by approximately 4.8%

compared to RBC but also exhibited a higher adaptability to fluctuating electricity prices. This adaptability is reflected in the increased number of cycles and the redistribution of activation times across different schemes, showcasing MPC's potential for dynamic pricing models.

Figure 4-13. HP operation distribution by hour with electricity prices and average of thermal load (test 3)

Figure 4-13 depicts the HP operation distribution by hour over the simulation horizon. The daily fluctuations in electricity price are indicated by the black line, and the green line represents the average thermal load throughout the simulation timeframe. During midnight hours, the MPC activates the HP more frequently than the RBC due to lower electricity prices. This pattern is also evident during other low-cost periods. During these times, MPC makes extensive use of the HP to maximize the charging of the TES, achieving its highest HP operation rates when electricity prices are at their lowest. In contrast, during peak electricity price periods, such as between 07:00 and 08:00 in the morning, RBC shows the highest levels of HP operation. The MPC effectively manages HP operation during off-peak hours (00:00 to 06:00, 13:00 to 17:00, and 22:00 to 23:00) for a total of 1355 minutes, compared to RBC's 879 minutes. This represents a 35% increase in off-peak HP's operation time by the MPC.

Besides, it is evident that the RBC operation bars tend to follow the load pattern more closely, whereas the MPC bars do not exhibit the same correlation. The MPC can predict future trends, including electricity prices and load peaks, enabling it to make optimal decisions. For instance, at 17:00, the MPC identifies an upcoming load peak and recognizes that the current electricity price is low. Consequently, it opts to run the HP extensively. Conversely, at 18:00, when the electricity price is high, the MPC strategically decides to minimize HP operation and instead discharges the TES.

Table 3-1 outlines the economic assessment of test 1, 2 and 3 conducted to compare the performance of RBC and MPC under various electricity pricing schemes.

Table 4-2. Economic assessment of test 1, 2 and 3

For the first test, a constant electricity price of 0.3 €/kWh was used for both off-peak and peak periods, with a thermal demand cost of 0.05 €/kWh. Under the RBC strategy, the total electricity cost was 71.28 €, the thermal cost was 71.84 €, and the total bill amounted to 143.12 €. When MPC was applied under the same pricing conditions, the total electricity cost decreased to 65.97

€, while the thermal cost slightly increased to 71.41 €, resulting in a total bill of 137.38 €. This represented a 7.44% reduction in electricity costs, a 0.5% decrease in thermal costs, and an overall decrease of 4% in the total bill.

In the second test, TOU pricing was considered, with off-peak electricity priced at 0.15 €/kWh and peak electricity remaining at 0.3 €/kWh. The thermal demand cost remained at 0.05 €/kWh. Under the RBC strategy, the total electricity cost was 65.64 €, the thermal cost was 71.84 €, and the total bill was 137.48 €. With MPC, the total electricity cost was reduced to 61.24 €, the thermal cost slightly increased to 73.85 €, and the total bill was 135.09 €. These results indicated a 6.7% reduction in electricity costs, a 2.7% increase in thermal costs, and an overall 1.73% reduction in the total bill.

Test 3 utilized variable electricity pricing, which more accurately reflects real-world conditions. Under RBC, the total electricity cost was 63.88 €, with a thermal cost of 71.84 €, leading to a total bill of 135.72 €. When MPC was applied, the total electricity cost significantly decreased to 50.01 €, while the thermal cost increased to 73.13 €, resulting in a total bill of 123.14 €. This test showed a substantial 21.7% reduction in electricity costs, a 1.76% increase in thermal costs, and an overall 9.26% decrease in the total bill.

Across all tests, the MPC strategy consistently outperformed RBC in terms of reducing total electricity costs. While the thermal costs slightly increased in some scenarios, the overall total bill was always lower with MPC, demonstrating its effectiveness in reducing costs under varying pricing schemes. The most significant savings were observed under variable electricity pricing, highlighting the potential of MPC to adapt to dynamic pricing environments and achieve substantial cost reductions.

Table 4-3 provides a comprehensive overview of various performance metrics under different control strategies and test conditions, highlighting key differences in operation and efficiency.

Table 4-3. A comprehensive overview of various performance metrics for test 1, 2 and 3



The analysis shows that the total HP operation time was consistently lower for MPC, indicating more optimized usage of the heat pump. The number of ON/OFF cycles increased with MPC, suggesting a more dynamic response to changing conditions. It is beneficial to include a term in the objective function to reduce these cycles.

The amount of power that the controller failed to cover (Qth, dis) was a bit higher in MPC controller. However, this value remains very low. Further investigation, incorporating a penalty in the objective function, could help in reducing this uncovered power.

Test 4: Performance assessment of MPC and RBC with constant electricity price and DH temperature following load profile

Test 4 was conducted to assess the performance of MPC and RBC under conditions of constant electricity price while ensuring the DH temperature follows a load profile and varies between 40°C to 55°C. In this scenario, the DH temperature was regulated to align with the load profile, presenting a more challenging operational environment for both control strategies. The objective was to observe how MPC would manage the situation compared to RBC under these specific conditions. MPC was expected to demonstrate its capability to predict future load variations and adjust the DH temperature proactively, thereby optimizing energy usage and maintaining the desired thermal comfort.

Figure 4-14 shows the result of Test 4. As can be observed, MPC managed to reduce the electricity cost by 6.83 % compared to RBC.



Figure 4-14. Result of comparison the performance of MPC vs. RBC with constant electricity price and DH temperature following load profile (test 4)



Figure 4-15. Activation time of the HP in test 4

Figure 4-15 illustrates the activation time of the HP across different schemes, allowing for a comparison between RBC and MPC. Under the RBC control strategy, the total activation time of the HP was 2072 minutes. Most of this activation time was dominated by scheme 2, which operated for 1056 minutes, representing 51% of the total HP_{ON} time. Scheme 1 accounted for 1016 minutes, or 49% of the activation period. The RBC approach recorded a low number of ON/OFF cycles, totaling 44 cycles. In contrast, the MPC control strategy showed a different pattern. The total activation time of the HP under MPC was 1941 minutes, indicating a reduction compared to RBC. Scheme 2 was the primary scheme, with an activation time of 1080 minutes, accounting for 55.6% of the total HP_{ON} time. Scheme 1 was active for 861 minutes, making up 44.4% of the activation period. The MPC strategy resulted in a higher number of ON/OFF cycles, with 51 cycles recorded during the test. This comparison reveals that while the MPC strategy managed to reduce the total HP activation time, it also led to an increase in the frequency of ON/OFF cycles.

Table 4-4 presents the economic assessment of test 4. For this test, a constant electricity price of 0.3 €/kWh was applied for both off-peak and peak periods, with a thermal demand cost of 0.05 €/kWh. Under the RBC strategy, the total electricity cost was 60.24 €, the thermal cost was 70.71 €, and the total bill amounted to 130.95 €. When MPC was applied under the same pricing conditions, the total electricity cost decreased to 56.12 €, while the thermal cost remained unchanged at 70.97 €, resulting in a total bill of 127.09 €. This represented a 6.83% reduction in electricity costs and an overall decrease of 2.94% in the total bill. The thermal costs did change only 0.3% between the control strategies, indicating that the savings achieved by MPC were mainly due to more efficient electricity usage.

Table 4-4. Economic assessment of test 4

Table 4-5 provides a comprehensive overview of various performance metrics for Test 4, conducted to compare the performance of RBC and MPC. The amount of power that the controller failed to cover was 0.07% under the RBC strategy. In contrast, this value increased to 0.17% under the MPC strategy.

Table 4-5. A comprehensive overview of various performance metrics for test 4

Test 5: Comparison of MPC and RBC with constant electricity price and inverse relationship between DH temperature and load

Test 5 was performed to assess the performance of MPC and RBC under a constant electricity price, with the DH temperature inversely related to the load. In this scenario, the DH temperature was regulated to be lower when the load was high and higher when the load was low, creating a more complex operational environment for both control strategies. DH temperature varied between 45°C to 55°C.

Figure 4-16 presents the results of Test 5. It can be observed that MPC managed to reduce the electricity cost to 67.34 euros, which represents a 4.08% decrease compared to the RBC cost of 70.21 euros.

Figure 4-16. Result of Comparison of MPC and RBC with constant electricity price and inverse relationship between DH temperature and load (test 5)

Figure 4-17 illustrates the activation time of the HP. Under the RBC control strategy, the total activation time of the HP was 2482 minutes. Most of this activation time was dominated by scheme 1, which operated for 1566 minutes, representing 63.1% of the total HP_{ON} time. Scheme 2 accounted for 916 minutes, or 36.9% of the activation period. The RBC approach recorded a low number of ON/OFF cycles, totaling 37 cycles. In contrast, the MPC control strategy showed a different pattern. The total activation time of the HP under MPC was 2400 minutes, indicating a reduction compared to RBC. Scheme 1 was the primary scheme, with an activation time of 1242 minutes, accounting for 51.7% of the total HP_{ON} time. Scheme 2 was active for 1158 minutes, making up 48.2% of the activation period. The MPC strategy resulted in a higher number of ON/OFF cycles, with 51 cycles recorded during the test.

Figure 4-17. Activation time of the HP in test 5

Table 4-6 presents the economic assessment of test 5. For this test, a constant electricity price of 0.3 €/kWh was applied for both off-peak and peak periods, with a thermal demand cost of 0.05 €/kWh. Under the RBC strategy, the total electricity cost was 70.21 €, the thermal cost was 70.18 €, and the total bill amounted to 140.39 €. When MPC was applied under the same pricing conditions, the total electricity cost decreased to 67.34 €, while the thermal cost slightly increased to 70.9 €, resulting in a total bill of 138.24 €. This represented a 4.08% reduction in electricity costs, a 1% increase in thermal costs, and an overall decrease of 1.53% in the total bill.

Table 4-6. Economic assessment of test 5

Table 4-7 provides a comprehensive overview of various performance metrics for test 5, conducted to compare the performance of RBC and MPC. Under the RBC strategy, the maximum COP_{sys} was 16.52, while the minimum was 4.85. The amount of power that the controller failed to cover was 0.06%. In contrast, the MPC strategy demonstrated an identical maximum COP_{sys} at 16.52, with the minimum 4.37. However, the amount of power that the controller failed to cover was higher for MPC at 0.21%. Although the Q_{th, disc} value increased with MPC, it remains relatively low, indicating that further optimization could reduce this discrepancy.

Table 4-7. A comprehensive overview of various performance metrics for test 5

Test 6: Comparison of MPC and RBC with variable electricity price and higher DH temperature

In Test 6, the performance of MPC and RBC was assessed under a variable electricity price, with the DH temperature which varies between 40°C to 60°C. In previous tests, as discussed in Table 3-8 and Table 3-10, the substation could only transition to schemes 1 and 2. However, in this test, it can also transition to scheme 3. The findings of this evaluation are depicted in Figure 4-18. It is evident from the results that the electricity cost was reduced to 47.11 euros using MPC, marking a 18.6% reduction compared to the RBC cost of 57.9 euros.

Figure 4-19 illustrates the activation time of the HP across different schemes for both RBC and MPC, as well as the number of ON/OFF cycles for each control strategy. Under the RBC strategy, the total activation time of the HP was recorded as 2167 minutes. This activation time was predominantly spent in Scheme 1, which accounted for 1410 minutes or 65.1% of the total HP_{ON} time. Scheme 2 saw the HP active for 274 minutes, representing 12.6% of the total activation period. Additionally, scheme 3 accounted for 483 minutes, making up 22.3% of the total activation time. The RBC strategy recorded 39 ON/OFF cycles, indicating a moderate frequency of activation and deactivation events. In contrast, the MPC strategy demonstrated a different pattern in HP activation time, with a total of 2104 minutes. The majority of this time, 1225 minutes or 58.2% of the total HP_{ON} time, was also spent in scheme 1. Scheme 2 had the HP active for 296 minutes, accounting for 14.1% of the total activation period. Scheme 3 was used for 583 minutes, representing 27.7% of the total activation time. The MPC strategy resulted in a higher number of ON/OFF cycles, with 53 cycles recorded.



Figure 4-18. Result of Comparison of MPC and RBC with constant electricity price and higher DH temperature (test 6)



Figure 4-19. Activation time of the HP in test 6

The substation has activated scheme 4, as depicted in Figure 4-19. The detailed conditions for this activation are provided in Table 3-6, which specifies that $T_{set,direct_DH}$ is set to 60°C. Notably, during this test, the district heating temperature does not exceed 60°C, prompting an investigation into the activation of scheme 4. Exceptions to the scheme transitions, described in Appendix 2, reveal that if the district heating temperature exceeds 55°C and the return temperature of the TES ($T_{ret,TES}$) is also above 55°C, the controller is restricted from switching to schemes 1, 2, or 3. This

restriction is due to the maximum allowable input temperature for the evaporator of the heat pump ($T_{in,Max,HP}$) being set to 55°C. This limit, set by the manufacturer, ensures the proper operation of the heat pump's evaporator.

Since the control signal is ON, only two possibilities exist. The first is to prevent the substation from bringing the heat pump into the circuit until district heating temperature or $T_{ret,TES}$ falls below $T_{in,Max,HP}$. In this scenario, schemes 1, 2, or 3 can be utilized.

However, the disadvantage of this approach is that the heat pump frequently turns on and off, potentially causing damage over time, which is not recommended. The second approach, which has been implemented, is to activate scheme 4. Although this ensures safe control, it also has drawbacks. If district heating temperature is lower than the temperature at the top of the tank, it will reduce the tank temperature, which is not ideal. Additionally, as long as the control signal is ON and scheme 4 is active, power must be purchased from DH, increasing costs as shown in Table 4-8. If the heat pump could be turned on, less money would be spent on DH power.

Table 4-8. Economic assessment of test 6

	$C_{el, off-peak}$ [€/kWh]	$C_{el, peak}$ [€/kWh]	$C_{th, dh}$ [€/kWh]	$C_{el, total}$ [€]	$C_{th, total}$ [€]	Total bill [€]
RBC	Variable		0.05
MPC-Test 6	Variable		0.05
Variation [%]			

Table 4-8 compares the costs associated with RBC and MPC in test 6. Similar to test 3, variable electricity pricing was employed to simulate real-world conditions, with district heating priced at (0.05 €/kWh). The total electricity cost for MPC is 18.6% lower than RBC, resulting in a savings of 10.79 €. The total district heating cost for MPC is 25.15% higher than RBC, leading to a spending more money for buying from DH. Consequently, the overall total bill for MPC is 10.1% higher than that of RBC, providing a total cost increment of 15.29 € for one week of simulation. As previously noted, this limitation pertains to special cases that may occur, but not often.

Table 4-9. A comprehensive overview of various performance metrics for test 6

Table 4-9 provides a detailed comparison of various performance metrics for RBC and MPC. Under the RBC strategy, the maximum COP_{sys} was 16.18, while the minimum was 4.28. The HP was operational for 2167 minutes, with 39 cycles of activation. Additionally, the $Q_{th, disc}$ was low at 0.1%. In contrast, the MPC strategy showed an identical maximum COP_{sys} at 16.18, with the minimum at 3.29. The HP was operational for a slightly shorter duration of 2104 minutes but had more frequent activations, with 53 cycles. The $Q_{th, disc}$ increased slightly to 0.75%.

Test 7: Comparison of MPC and RBC with constant electricity prices and realistic DH temperatures

In test 7, DH temperature varies between 43°C and 55°C to reflect realistic conditions. Realistic conditions in DH temperature refer to the typical fluctuations observed in DH systems, often influenced by daily and seasonal variations in demand. For instance, during colder periods or peak usage times in the morning and evening, DH temperatures might be higher to meet increased heating needs, while during milder periods or off-peak times, temperatures are lower. This dynamic range of temperatures, reflecting real-world operational patterns, ensures that the system can effectively respond to varying heat demands throughout the day.

The electricity price was considered constant to isolate the impact of DH temperature variations on system performance. The results, illustrated in Figure 4-20, show that MPC achieved a cost of 61.39 euros, significantly lower than the 67.09 euros incurred by RBC. This represents an 8.5% reduction in electricity cost.

Figure 4-21 displays the activation duration of the HP across various schemes for both RBC and MPC strategies, along with the number of ON/OFF cycles for each control method. For the RBC strategy, the total HP activation time was observed to be 2351 minutes. This time was mainly concentrated in scheme 1, which accounted for 1491 minutes or 63.4% of the total HP_{ON} time. scheme 2 had the HP active for 860 minutes, representing 36.6% of the total activation period. The RBC strategy exhibited 40 ON/OFF cycles, indicating a moderate frequency of switching events.



Figure 4-20. Comparison of MPC and RBC with constant electricity prices and realistic DH temperatures (test 7)



Figure 4-21. Activation time of the HP in test 7

Conversely, the MPC strategy showed a total HP activation time of 2144 minutes. In this strategy, scheme 1 was used for 1039 minutes, making up 48.5% of the total HP_{ON} time, while scheme 2

accounted for 1105 minutes or 51.5% of the activation time. The MPC strategy resulted in a higher number of ON/OFF cycles, with 48 cycles recorded, indicating a more frequent switching pattern compared to RBC.

Figure 4-22. HP operation distribution by hour with electricity prices, average of thermal load and DH temperature (test 7)

Figure 4-22 illustrates that the electricity price remains constant. The main incentive for the MPC in this scenario is the DH temperature. For instance, at 00:00, 01:00, 09:00, 10:00 and 21:00 when the DH temperature is elevated, the MPC decided to activate the HP to charge the tank because in this case the COP_{sys} is higher. Therefore, without considering price incentives, MPC find it hard to reduce the total cost of substation.

Table 4-10. Economic assessment of test 7

Table 4-10 presents the economic assessment of test 7. For this test, a constant electricity price of 0.3 €/kWh was applied for both off-peak and peak periods, with a thermal demand cost of 0.05 €/kWh. Under the RBC strategy, the total electricity cost was 67.09 €, the thermal cost was 71.19 €, and the total bill amounted to 138.28 €. When MPC was applied under the same pricing conditions, the total electricity cost decreased to 61.39 €, while the thermal cost slightly increased to 71.98 €, resulting in a total bill of 133.37 €. This represented an 8.5% reduction in electricity costs, a 1.09% increase in thermal costs, and an overall decrease of 3.55% in the total bill.

Table 4-11. A comprehensive overview of various performance metrics for test 7

Table 4-11 provides a comprehensive overview of various performance metrics for test 7, conducted to compare the performance of RBC and MPC. Under the RBC strategy, the maximum COP_{sys} was 14.25, while the minimum was 4.46. The amount of power that the controller failed to cover was 0.14%. In contrast, the MPC strategy demonstrated an identical maximum COP_{sys} at 14.25, with the minimum 4.01. However, the amount of power that the controller failed to cover was higher for MPC at 0.29%. Although the $Q_{th, disc}$ value increased with MPC, it remains low.

Test 8: Evaluation of MPC and RBC performance with realistic electricity pricing and DH temperatures

In Test 8, the performance of MPC and RBC was evaluated under realistic conditions, with the DH temperature ranging between 43°C and 55°C and realistic electricity pricing as shown in Figure 4-10. The results, illustrated in Figure 4-23, indicate that MPC achieved a cost of 45.61 euros, significantly lower than the 59.96 euros incurred by RBC. This represents a 23.9% reduction in electricity cost, highlighting the efficiency of MPC in managing both realistic electricity pricing and district heating temperatures.



Figure 4-23. Evaluation of MPC and RBC performance with realistic electricity pricing and DH temperatures (test 8)

Figure 4-24 depicts the activation duration of the HP across various schemes for both RBC and MPC strategies, along with the count of ON/OFF cycles for each control method. For the RBC strategy, the total HP activation time was measured at 2351 minutes. This period was predominantly occupied by scheme 1, which accounted for 1491 minutes or 63.4% of the total HP_{ON} time. Scheme 2 recorded the HP being active for 860 minutes, constituting 36.6% of the total activation time. The RBC strategy exhibited 40 ON/OFF cycles, indicating a moderate frequency of switching events. Conversely, the MPC strategy demonstrated a total HP activation time of 2128 minutes. Within this strategy, scheme 2 accounted for 1173 minutes, representing 55.1% of the total HP_{ON} time, while scheme 1 accounted for 955 minutes or 44.9% of the activation time. The MPC strategy resulted in a higher number of ON/OFF cycles, with 54 cycles recorded, indicating a more frequent switching pattern compared to RBC.



Figure 4-24. Activation time of the HP in test 8




Figure 4-25. HP operation distribution by hour with electricity prices and average of thermal load (test 8)

Figure 4-25 shows the HP operation distribution by hour over the simulation horizon. The electricity price, the average thermal load during the simulation period and DH temperature are presented.

MPC frequently operates the HP during periods of low electricity prices, such as midnight, 15:00 to 17:00, and 22:00 to midnight, to maximize the charging of the TES. In contrast, RBC shows the highest HP operation during peak electricity cost at 07:00 in the morning. RBC HP operation

follows the load profile closely, while MPC typically tries to predict future conditions and charges the tank at favorable times when the cost is low, and the DH temperature is high enough. Comparing MPC and RBC, it is evident that MPC effectively manages the thermal load by utilizing low-cost hours to charge the TES. MPC managed to turn on the HP for 1,295 minutes during off-peak times, while RBC did so for only 1,013 minutes, which is approximately 22% more. However, during peak thermal load hours, MPC operates the HP less often than RBC. Additionally, at 23:00, when the DH temperature was high and electricity costs were low, MPC decided to charge the tank as much as possible.

Table 4-12 compares the costs associated with RBC and MPC in test 8. Similar to test 3, variable electricity pricing was employed to simulate real-world conditions, with district heating priced at (0.05 €/kWh). The total electricity cost for MPC is 23.93% lower than RBC, resulting in a savings of 14.35€. The total district heating cost for MPC is 3.07% higher than RBC. Consequently, the overall total bill for MPC is 9.21% lower than that of RBC, providing a total cost reduction of 12.09€ for one week of simulation.

Table 4-12. Economic assessment of test 8

Table 4-13 provides a comprehensive overview of various performance metrics for test 8, conducted to compare the performance of RBC and MPC. Under the RBC strategy, the maximum COP_{sys} was 14.25, while the minimum was 4.46. The amount of power that the controller failed to cover was 0.14%. In contrast, the MPC strategy demonstrated an identical maximum COP_{sys} at 14.25, with the minimum 4. However, the amount of power that the controller failed to cover was a bit lower for MPC at 0.11%. Although the $Q_{th, disc}$ value increased with RBC, it remains low.

Table 4-13. A comprehensive overview of various performance metrics for test 8

4.2.1 Concluding remarks

In this chapter, the performance of MPC and RBC strategies for district heating systems was evaluated across various scenarios. The tests compared the effectiveness of both control methods under constant, TOU, and variable electricity pricing schemes. The results demonstrated that MPC consistently outperformed RBC in reducing electricity costs and optimizing energy consumption. MPC's advanced algorithm allows for dynamic adjustment of setpoints in real-time, effectively

responding to fluctuating electricity prices and varying thermal loads. This capability leads to significant cost savings and improved system efficiency, making MPC a more viable solution for modern district heating systems.

The study revealed that MPC's ability to predict future load variations and adjust operations proactively resulted in lower overall energy costs. Under constant electricity pricing, MPC achieved a cost reduction of 4% compared to RBC. In the TOU pricing scenario, MPC further optimized energy consumption by shifting usage to off-peak periods, resulting in a 1.73% total cost saving. The most notable performance was observed under variable electricity pricing, where MPC reduced total costs by a substantial 9.26%. In the most realistic scenario (Test 8), where both the electricity price and DH temperature exhibit realistic variations, the MPC demonstrated its efficiency by achieving a 23.93% reduction in electricity costs. Additionally, this optimization led to a 9.21% decrease in the total bill over the span of one week. This significant cost saving highlights the potential of MPC to manage energy consumption more effectively under real-world conditions.

The flexibility and adaptability of MPC were also demonstrated in its performance under different district heating temperature strategies. When the DH temperature followed the load profile, MPC optimized energy usage better than RBC, achieving a 6.83% reduction in electricity costs. In scenarios where the DH temperature was inversely related to the load, MPC still managed significant cost savings, showing its robustness in various operational contexts.

Furthermore, the study highlighted the operational advantages of MPC beyond cost savings. By considering higher temperatures for the district heating system, both RBC and MPC systems were able to transition through all operational schemes, including handling exception conditions that may arise. This comprehensive control over various schemes and potential exceptions underscores MPC's robustness and adaptability in maintaining efficient and reliable system performance.

Overall, the study illustrates that MPC is a superior control strategy for district heating systems, offering substantial economic and operational benefits over traditional RBC methods. The ability to dynamically adjust to real-time conditions makes MPC highly effective in reducing costs and improving system efficiency.

Chapter 5

5 Conclusions and recommendation for further work

This study provides an overview of the evolution and operational dynamics of DHCNs, particularly focusing on the transition from conventional systems to the advanced 5GDHCNs. These innovative systems represent a significant advancement in terms of effective energy management from a circular energy perspective, especially in application characterized by concurrent heating and cooling needs all over the year. Despite the benefits identified, the complex management of distributed energy source in 5GDHCNs requires sophisticated control strategies to be implemented at user substations, aimed to both the minimize the energy use and to shift energy use towards the most favorable hours of the day.

The research underscores the fundamental role of advanced controls (particularly the MPC) in enhancing the effective operation of these substations. MPC's predictive capabilities allow the system to make informed, efficient decisions based on forecasted data, significantly optimizing the performance of TES and HP systems.

The PhD research involved developing several models to implement MPC effectively:

- A flexible ROM to precisely forecast thermal load in residential buildings.
- A detailed TES model to optimize performance, improve energy efficiency, and ensure reliable energy supply, fulfilling three critical objectives: capturing fundamental dynamics, maintaining consistent energy balance, and ensuring uniform temperature distribution.
- A state-machine-based HP model (Provided by Eurac Research).
- An optimizer based on dynamic programming (Provided by Eurac Research).

All models were validated using monitored data, ensuring their accuracy and reliability under a variety of operating conditions.

The study's results demonstrate the superior performance of MPC over RBC strategies across various scenarios. MPC consistently reduced electricity costs and optimized energy consumption more effectively than RBC. Under different electricity pricing schemes—constant, TOU, and variable—MPC achieved significant cost savings, demonstrating its ability to dynamically adjust setpoints in real-time and respond to fluctuating prices and thermal loads. Notably, MPC reduced electricity prices by 7.44% under constant pricing, 6.7% under TOU pricing, and an impressive 21.7% under variable pricing. The flexibility and adaptability of MPC were further evidenced by its performance under different strategies assumed for district heating supply temperature management. With respect to the operating conditions analyzed, MPC optimizes energy use, achieving a 6.83% reduction in electricity costs when the district heating supply temperature followed the building load profile. Even with the supply temperature inversely related to the load, the MPC managed significant cost savings, proving its robustness across various operational contexts. Under realistic conditions, where both electricity prices and DH temperatures vary, MPC efficiently reduced electricity costs by 23.93%. This optimization also resulted in a 9.21% decrease in the total bill over the simulation horizon.

Beyond cost savings, MPC offers several operational advantages by effectively handling different district heating schemes and challenging conditions. One significant advantage is load shifting. MPC strategically operates the HP during periods of low electricity prices to maximize the charging of the TES. In contrast, traditional RBC often operates the HP during peak electricity cost periods. This demonstrates MPC's capability to manage the thermal load more efficiently by utilizing low-cost periods for energy storage, resulting in less HP operation during peak thermal load hours.

In conclusion, this study illustrates that MPC is a superior control strategy for 5GDHCNs substations, offering substantial economic and operational benefits over conventional RBC methods.

Several key areas will be the focus of future developments to enhance the performance and robustness of the current system, including:

- During testing, it was observed that MPC sometimes does not completely meet the load when compared to RBC. Although this unmet load is less than 1%, incorporating a penalty function for non-responded loads is recommended. This penalty function will help refine the control strategy by accounting for unmet thermal demands.
- MPC tends to cycle the HP ON/OFF more frequently than RBC, leading to higher maintenance costs and potentially reducing the lifespan of the HP over time. To address

this issue, reducing the number of HP's ON/OFF cycles will be included in the objective function. This optimization aims to balance operational efficiency with the longevity of the HP, ensuring both cost-effectiveness and sustainability in the long term.

- In this study, the HP was solely connected to the electricity grid, and the roles of PV systems and battery storage were not considered. By integrating PV systems and battery storage, significant benefits can be realized. TOU pricing can be leveraged to optimize the operation of the HP, allowing it to charge the TES during periods of low electricity prices. Additionally, the battery can be charged during these favorable times, and during peak electricity prices, the HP can be operated using the stored battery power. This approach can lead to enhanced cost savings. Ultimately, achieving these benefits requires a robust n-dimensional optimization framework to effectively manage the complex interactions and dependencies within the integrated system.
- Moreover, this research could act as a starting point for transitioning from the optimal control of a single substation to the optimal management of a pool of substations interconnected with electrical and thermal grids. By broadening the focus beyond a single substation, the opportunities for developing more efficient and cohesive control strategies across multiple substations can be investigated.

References

- [1] N. Kampelis *et al.*, “An Integrated Energy Simulation Model for Buildings,” *Energies*, 2020, doi: 10.3390/en13051170.
- [2] “Energy consumption in households - Statistics Explained.” https://ec.europa.eu/eurostat/statistics-explained/index.php?title=Energy_consumption_in_households (accessed Aug. 23, 2023).
- [3] S. Osorio, O. Tietjen, M. Pahle, R. C. Pietzcker, and O. Edenhofer, “Reviewing the Market Stability Reserve in light of more ambitious EU ETS emission targets,” *Energy Policy*, vol. 158, p. 112530, Nov. 2021, doi: 10.1016/j.enpol.2021.112530.
- [4] M. H. Fouladfar, A. Soppelsa, H. Nagpal, R. Fedrizzi, and G. Franchini, “Adaptive thermal load prediction in residential buildings using artificial neural networks,” *Journal of Building Engineering*, p. 107464, Jul. 2023, doi: 10.1016/j.job.2023.107464.
- [5] R. Wiltshire, *Advanced District Heating and Cooling (DHC) Systems*. Woodhead Publishing, 2015.
- [6] S. Buffa, M. Cozzini, M. D’Antoni, M. Baratieri, and R. Fedrizzi, “5th generation district heating and cooling systems: A review of existing cases in Europe,” *Renewable and Sustainable Energy Reviews*, vol. 104, pp. 504–522, Apr. 2019, doi: 10.1016/j.rser.2018.12.059.
- [7] J. Ling, N. Dai, J. Xing, and H. Tong, “An improved input variable selection method of the data-driven model for building heating load prediction,” *Journal of Building Engineering*, vol. 44, p. 103255, 2021.
- [8] H. Lund *et al.*, “4th Generation District Heating (4GDH): Integrating smart thermal grids into future sustainable energy systems,” *Energy*, vol. 68, pp. 1–11, Apr. 2014, doi: 10.1016/j.energy.2014.02.089.
- [9] S. Werner, “District Heating and Cooling,” Elsevier, 2013. Accessed: Jul. 26, 2023. [Online]. Available: <https://urn.kb.se/resolve?urn=urn:nbn:se:hh:diva-24115>
- [10] G. Schweiger, F. Kuttin, and A. Posch, “District Heating Systems: An Analysis of Strengths, Weaknesses, Opportunities, and Threats of the 4GDH,” *Energies*, vol. 12, no. 24, p. 4748, Dec. 2019, doi: 10.3390/en12244748.
- [11] H. Averfalk *et al.*, *Low-Temperature District Heating Implementation Guidebook: Final Report of IEA DHC Annex TS2. Implementation of Low-Temperature District Heating Systems*. Fraunhofer IRB Verlag, 2021.
- [12] S. Buffa, A. Soppelsa, M. Pipiciello, G. Henze, and R. Fedrizzi, “Fifth-generation district heating and cooling substations: Demand response with artificial neural network-based model predictive control,” *Energies*, vol. 13, no. 17, p. 4339, 2020.

- [13] B. Welsch, L. Göllner-Völker, D. O. Schulte, K. Bär, I. Sass, and L. Schebek, “Environmental and economic assessment of borehole thermal energy storage in district heating systems,” *Applied Energy*, vol. 216, pp. 73–90, Apr. 2018, doi: 10.1016/j.apenergy.2018.02.011.
- [14] M. Werner, S. Muschik, M. Ehrenwirth, C. Trinkl, and T. Schrag, “Sector Coupling Potential of a District Heating Network by Consideration of Residual Load and CO₂ Emissions,” *Energies*, vol. 15, no. 17, Art. no. 17, Jan. 2022, doi: 10.3390/en15176281.
- [15] I. Irena, “Renewable energy policies in a time of transition: Heating and cooling,” 2020.
- [16] U. Persson and S. Werner, *Quantifying the Heating and Cooling Demand in Europe : Work Package 2, Background Report 4*. 2015. Accessed: Jul. 28, 2023. [Online]. Available: <https://urn.kb.se/resolve?urn=urn:nbn:se:hh:diva-35236>
- [17] J. Thorsen, “District Heating & Cooling a VISION towards 2020–2030–2050,” presented at the 34th Euroheat & Power Congress, 2009, pp. 25–26.
- [18] I. Sarbu, M. Mirza, and D. Muntean, “Integration of Renewable Energy Sources into Low-Temperature District Heating Systems: A Review,” *Energies*, vol. 15, no. 18, Art. no. 18, Jan. 2022, doi: 10.3390/en15186523.
- [19] B. Sanner, “EGEC Deep Geothermal Market Report.,” *Journal of Sustainable Energy*, vol. 3, no. 2, 2012.
- [20] P. Dumas and L. Angelino, “GeoDH: promote geothermal district heating systems in Europe,” *Technika Poszukiwań Geologicznych*, vol. 54, no. 2, pp. 25–39, 2015.
- [21] “1 GW Solar District Heating in Denmark,” *PlanEnergi*, Jan. 02, 2017. <https://planenergi.eu/en/1-gw-sdh-in-dk/> (accessed Jul. 28, 2023).
- [22] Z. Tian *et al.*, “Large-scale solar district heating plants in Danish smart thermal grid: Developments and recent trends,” *Energy conversion and management*, vol. 189, pp. 67–80, 2019.
- [23] R. Marx, D. Bauer, and H. Drucek, “Energy efficient integration of heat pumps into solar district heating systems with seasonal thermal energy storage,” *Energy Procedia*, vol. 57, pp. 2706–2715, 2014.
- [24] Marco Cozzini, “Integration of substations into DHC networks.” <http://www.flexynets.eu/Download?id=file:54341800&s=7249709264999378256> (accessed Aug. 02, 2023).
- [25] “Advanced control strategies for district heating and cooling systems - -.” <https://bia.unibz.it/esploro/outputs/doctoral/Advanced-control-strategies-for-district-heating/991006127788101241> (accessed Aug. 02, 2023).
- [26] S. Buffa, M. H. Fouladfar, G. Franchini, I. Lozano Gabarre, and M. Andrés Chicote, “Advanced Control and Fault Detection Strategies for District Heating and Cooling Systems—A Review,” *Applied Sciences*, vol. 11, no. 1, Art. no. 1, Jan. 2021, doi: 10.3390/app11010455.

- [27] P. Leoni, A. Bres, I. Marini, and A. Capretti, “Lowering the operating temperatures in old-generation district heating systems: First results from the TEMPO demonstration project in Brescia (Italy),” presented at the 6th International Conference on Smart Energy Systems, 2020, pp. 1–12.
- [28] “Albertslund shunt - rewardheat.” <https://www.rewardheat.eu/en/Media/News-&-Events/Albertslund-shunt> (accessed Jul. 28, 2023).
- [29] S. Svendsen, D. S. Østergaard, and X. Yang, “Solutions for low temperature heating of rooms and domestic hot water in existing buildings,” presented at the 3rd International Conference on Smart Energy Systems and 4th Generation District Heating [Internet]. National Museum, Copenhagen: Department of Development and Planning, Aalborg University, 2017, p. 151.
- [30] N. Vetterli and M. Sulzer, “Dynamic analysis of the low-temperature district network" Suurstoffi" through monitoring,” presented at the Proceedings of International Conference CISBAT 2015 Future Buildings and Districts Sustainability from Nano to Urban Scale, LESO-PB, EPFL, 2015, pp. 517–522.
- [31] J. Stene and G. Eggen, “Heat pump system with distribution at intermediate temperature at the University of Bergen,” 1995.
- [32] T. Marella, G. Zarotti, and D. Bosco, “Riqualificare un immobile storico con pompa di calore VRV,” *AICARR J*, vol. 24, pp. 48–56, 2014.
- [33] M. Wirtz, L. Kivilip, P. Remmen, and D. Müller, “5th Generation District Heating: A novel design approach based on mathematical optimization,” *Applied Energy*, vol. 260, p. 114158, 2020.
- [34] S. Samsatli and N. J. Samsatli, “A general mixed integer linear programming model for the design and operation of integrated urban energy systems,” *Journal of Cleaner Production*, vol. 191, pp. 458–479, 2018.
- [35] D. Buoro, P. Pinamonti, and M. Reini, “Optimization of a Distributed Cogeneration System with solar district heating,” *Applied Energy*, vol. 124, pp. 298–308, 2014.
- [36] “low and high level controls - flexynets.” <https://w4u0es9f4.wimuu.com/en/Results/low-and-high-level-controls> (accessed Jul. 28, 2023).
- [37] J. Vivian, X. Jobard, I. B. Hassine, D. Pietrushka, and J. L. Hurink, “Smart control of a district heating network with high share of low temperature waste heat,” presented at the Proceedings of the 12th conference on sustainable development of energy, Water and Environmental Systems-SDEWES, Dubrovnik, Croatia, 2017, pp. 4–8.
- [38] T. Schütz, R. Streblow, and D. Müller, “A comparison of thermal energy storage models for building energy system optimization,” *Energy and Buildings*, vol. 93, pp. 23–31, 2015.
- [39] “Baviere: Optimal control of district heating systems... - Google Scholar.” https://scholar.google.com/scholar_lookup?title=Optimal+Control+of+District+Heating+Systems+using+Dynamic+Simulation+and+Mixed+Integer+Linear+Programming&conference=Proceedings+

- of+the+12th+International+Modelica+Conference&author=Giraud,+L.&author=Merabet,+M.&author=Baviere,+R.&author=Vall%C3%A9,+M.&publication_year=2017 (accessed Jul. 28, 2023).
- [40] L. Giraud, “A control method of DH systems based on production and distribution optimization,” 2016, [Online]. Available: https://www.lsta.lt/files/events/2016-04-18_EHPkonfer/Pranesimai/Sesija%20I/L.GIRAUD.pdf
- [41] T. Kohne, D. Piendl, and M. Weigold, *Optimizing Investment Planning For District Heating Coupling Of Industrial Energy Systems Using MILP*. Gottfried Wilhelm Leibniz Universität Hannover, 2023.
- [42] L. Merkert, A. A. Haime, and S. Hohmann, “Optimal Scheduling of Combined Heat and Power Generation Units Using the Thermal Inertia of the Connected District Heating Grid as Energy Storage,” *Energies*, vol. 12, no. 2, Art. no. 2, Jan. 2019, doi: 10.3390/en12020266.
- [43] P. Gabrielli, A. Acquilino, S. Siri, S. Bracco, G. Sansavini, and M. Mazzotti, “Optimization of low-carbon multi-energy systems with seasonal geothermal energy storage: The Anergy Grid of ETH Zurich,” *Energy Conversion and Management: X*, vol. 8, p. 100052, Dec. 2020, doi: 10.1016/j.ecmx.2020.100052.
- [44] “Survey on Lagrangian relaxation for MILP: importance, challenges, historical review, recent advancements, and opportunities | SpringerLink.” <https://link.springer.com/article/10.1007/s10479-023-05499-9> (accessed Aug. 23, 2023).
- [45] “MILP-based discrete sizing and topology optimization of truss structures: new formulation and benchmarking | Structural and Multidisciplinary Optimization.” <https://link.springer.com/article/10.1007/s00158-022-03325-7> (accessed Aug. 23, 2023).
- [46] L. Urbanucci, F. D’Ettorre, and D. Testi, “A Comprehensive Methodology for the Integrated Optimal Sizing and Operation of Cogeneration Systems with Thermal Energy Storage,” *Energies*, vol. 12, no. 5, Art. no. 5, Jan. 2019, doi: 10.3390/en12050875.
- [47] M. Casisi, S. Costanzo, P. Pinamonti, and M. Reini, “Two-Level Evolutionary Multi-objective Optimization of a District Heating System with Distributed Cogeneration,” *Energies*, vol. 12, no. 1, Art. no. 1, Jan. 2019, doi: 10.3390/en12010114.
- [48] T. Logenthiran and D. Srinivasan, “Multi-agent system for managing a power distribution system with Plug-in Hybrid Electrical vehicles in smart grid,” in *ISGT2011-India*, Dec. 2011, pp. 346–351. doi: 10.1109/ISET-India.2011.6145339.
- [49] F. Wemstedt and P. Davidsson, “An Agent-Based Approach to Monitoring and Control of District Heating Systems,” in *Developments in Applied Artificial Intelligence*, T. Hendtlass and M. Ali, Eds., in Lecture Notes in Computer Science. Berlin, Heidelberg: Springer, 2002, pp. 801–811. doi: 10.1007/3-540-48035-8_77.
- [50] C. Johansson, F. Wernstedt, and P. Davidsson, “Deployment of Agent Based Load Control in District Heating Systems”.

- [51] “Multi-Agent Control of Thermal Systems in Buildings.” https://scholar.googleusercontent.com/scholar?q=cache:GbjgMAJpHZIJ:scholar.google.com/&hl=en&as_sdt=0,5 (accessed Jul. 28, 2023).
- [52] Z. Wang, L. Wang, A. I. Dounis, and R. Yang, “Multi-agent control system with information fusion based comfort model for smart buildings,” *Applied Energy*, vol. 99, pp. 247–254, Nov. 2012, doi: 10.1016/j.apenergy.2012.05.020.
- [53] F. Bünning, M. Wetter, M. Fuchs, and D. Müller, “Bidirectional low temperature district energy systems with agent-based control: Performance comparison and operation optimization,” *Applied Energy*, vol. 209, pp. 502–515, Jan. 2018, doi: 10.1016/j.apenergy.2017.10.072.
- [54] J. A. Rossiter, *Model-based predictive control: a practical approach*. CRC press, 2017.
- [55] F. Borrelli, A. Bemporad, and M. Morari, *Predictive control for linear and hybrid systems*. Cambridge University Press, 2017.
- [56] J. Hou, H. Li, N. Nord, and G. Huang, “Model predictive control under weather forecast uncertainty for HVAC systems in university buildings,” *Energy and Buildings*, vol. 257, p. 111793, Feb. 2022, doi: 10.1016/j.enbuild.2021.111793.
- [57] D. Hering, M. E. Cansev, E. Tamassia, A. Xhonneux, and D. Müller, “Temperature control of a low-temperature district heating network with Model Predictive Control and Mixed-Integer Quadratically Constrained Programming,” *Energy*, vol. 224, p. 120140, Jun. 2021, doi: 10.1016/j.energy.2021.120140.
- [58] D. Blum *et al.*, “Field demonstration and implementation analysis of model predictive control in an office HVAC system,” *Applied Energy*, vol. 318, p. 119104, Jul. 2022, doi: 10.1016/j.apenergy.2022.119104.
- [59] J. Hou, H. Li, N. Nord, and G. Huang, “Model predictive control for a university heat prosumer with data centre waste heat and thermal energy storage,” *Energy*, vol. 267, p. 126579, Mar. 2023, doi: 10.1016/j.energy.2022.126579.
- [60] B. Lyons, E. O’Dwyer, and N. Shah, “Model reduction for Model Predictive Control of district and communal heating systems within cooperative energy systems,” *Energy*, vol. 197, p. 117178, Apr. 2020, doi: 10.1016/j.energy.2020.117178.
- [61] J. Zhao, J. Li, and Y. Shan, “Research on a forecasted load-and time delay-based model predictive control (MPC) district energy system model,” *Energy and Buildings*, vol. 231, p. 110631, Jan. 2021, doi: 10.1016/j.enbuild.2020.110631.
- [62] J. Jansen, F. Jorissen, and L. Helsen, “Optimal control of a fourth generation district heating network using an integrated non-linear model predictive controller,” *Applied Thermal Engineering*, vol. 223, p. 120030, Mar. 2023, doi: 10.1016/j.applthermaleng.2023.120030.

- [63] Z. Li, J. Liu, L. Jia, and Y. Wang, "Improving room temperature stability and operation efficiency using a model predictive control method for a district heating station," *Energy and Buildings*, vol. 287, p. 112990, May 2023, doi: 10.1016/j.enbuild.2023.112990.
- [64] A. La Bella and A. Del Corno, "Optimal management and data-based predictive control of district heating systems: The Novate Milanese experimental case-study," *Control Engineering Practice*, vol. 132, p. 105429, Mar. 2023, doi: 10.1016/j.conengprac.2022.105429.
- [65] E. Saloux and J. A. Candanedo, "Model-based predictive control to minimize primary energy use in a solar district heating system with seasonal thermal energy storage," *Applied Energy*, vol. 291, p. 116840, Jun. 2021, doi: 10.1016/j.apenergy.2021.116840.
- [66] M. Descamps, M. Vallée, and N. Lamaison, "Operational control of a multi-energy district heating system: comparison of model-predictive control and rule-based control," *Proceedings of ECOS*, pp. 2079–2089, 2019.
- [67] M. Taylor, S. Long, O. Marjanovic, and A. Parisio, "Model Predictive Control of Smart Districts With Fifth Generation Heating and Cooling Networks," *IEEE Transactions on Energy Conversion*, vol. 36, no. 4, pp. 2659–2669, Dec. 2021, doi: 10.1109/TEC.2021.3082405.
- [68] I. Adilkhanova, J. Ngarambe, and G. Y. Yun, "Recent advances in black box and white-box models for urban heat island prediction: Implications of fusing the two methods," *Renewable and Sustainable Energy Reviews*, vol. 165, p. 112520, Sep. 2022, doi: 10.1016/j.rser.2022.112520.
- [69] X. Li and J. Wen, "Review of building energy modeling for control and operation," *Renewable and Sustainable Energy Reviews*, vol. 37, pp. 517–537, 2014.
- [70] D. Dehestani, S. Su, H. Nguyen, and Y. Guo, "Robust fault tolerant application for HVAC system based on combination of online SVM and ANN black box model," in *2013 European Control Conference (ECC)*, Jul. 2013, pp. 2976–2981. doi: 10.23919/ECC.2013.6669140.
- [71] M. Emami Javanmard, S. F. Ghaderi, and M. Hoseinzadeh, "Data mining with 12 machine learning algorithms for predict costs and carbon dioxide emission in integrated energy-water optimization model in buildings," *Energy Conversion and Management*, vol. 238, p. 114153, Jun. 2021, doi: 10.1016/j.enconman.2021.114153.
- [72] Y. Chen, M. Guo, Z. Chen, Z. Chen, and Y. Ji, "Physical energy and data-driven models in building energy prediction: A review," *Energy Reports*, vol. 8, pp. 2656–2671, Nov. 2022, doi: 10.1016/j.egy.2022.01.162.
- [73] H. Nagpal, I.-I. Avramidis, F. Capitanescu, and P. Heiselberg, "Optimal energy management in smart sustainable buildings – A chance-constrained model predictive control approach," *Energy and Buildings*, vol. 248, p. 111163, Oct. 2021, doi: 10.1016/j.enbuild.2021.111163.
- [74] Y. Li, Z. O'Neill, L. Zhang, J. Chen, P. Im, and J. DeGraw, "Grey-box modeling and application for building energy simulations-A critical review," *Renewable and Sustainable Energy Reviews*, vol. 146, p. 111174, 2021.

- [75] N. Asprion *et al.*, “Gray-Box Modeling for the Optimization of Chemical Processes,” *Chemie Ingenieur Technik*, vol. 91, no. 3, pp. 305–313, 2019, doi: 10.1002/cite.201800086.
- [76] R. Lv, Z. Yuan, B. Lei, J. Zheng, and X. Luo, “Building thermal load prediction using deep learning method considering time-shifting correlation in feature variables,” *Journal of Building Engineering*, vol. 61, p. 105316, 2022.
- [77] F. Bünning *et al.*, “Physics-informed linear regression is competitive with two Machine Learning methods in residential building MPC,” *Applied Energy*, vol. 310, p. 118491, Mar. 2022, doi: 10.1016/j.apenergy.2021.118491.
- [78] M. Elnour *et al.*, “Neural network-based model predictive control system for optimizing building automation and management systems of sports facilities,” *Applied Energy*, vol. 318, p. 119153, 2022.
- [79] S. J. Cox, D. Kim, H. Cho, and P. Mago, “Real time optimal control of district cooling system with thermal energy storage using neural networks,” *Applied Energy*, vol. 238, pp. 466–480, Mar. 2019, doi: 10.1016/j.apenergy.2019.01.093.
- [80] A. Maiorino, M. G. Del Duca, and C. Aprea, “ART.I.CO. (ARTificial Intelligence for COoling): An innovative method for optimizing the control of refrigeration systems based on Artificial Neural Networks,” *Applied Energy*, vol. 306, p. 118072, Jan. 2022, doi: 10.1016/j.apenergy.2021.118072.
- [81] W. Gang and J. Wang, “Predictive ANN models of ground heat exchanger for the control of hybrid ground source heat pump systems,” *Applied Energy*, vol. 112, pp. 1146–1153, Dec. 2013, doi: 10.1016/j.apenergy.2012.12.031.
- [82] W. Gang, J. Wang, and S. Wang, “Performance analysis of hybrid ground source heat pump systems based on ANN predictive control,” *Applied Energy*, vol. 136, pp. 1138–1144, Dec. 2014, doi: 10.1016/j.apenergy.2014.04.005.
- [83] C. Vering, L. Maier, K. Breuer, H. Krützfeldt, R. Streblov, and D. Müller, “Evaluating heat pump system design methods towards a sustainable heat supply in residential buildings,” *Applied Energy*, vol. 308, p. 118204, Feb. 2022, doi: 10.1016/j.apenergy.2021.118204.
- [84] L. Jia, J. Liu, A. Chong, and X. Dai, “Deep learning and physics-based modeling for the optimization of ice-based thermal energy systems in cooling plants,” *Applied Energy*, vol. 322, p. 119443, Sep. 2022, doi: 10.1016/j.apenergy.2022.119443.
- [85] J. Lange and M. Kaltschmitt, “Probabilistic day-ahead forecast of available thermal storage capacities in residential households,” *Applied Energy*, vol. 306, p. 117957, Jan. 2022, doi: 10.1016/j.apenergy.2021.117957.
- [86] L. Scapino, H. A. Zondag, J. Diriken, C. C. M. Rindt, J. Van Bael, and A. Sciacovelli, “Modeling the performance of a sorption thermal energy storage reactor using artificial neural networks,” *Applied Energy*, vol. 253, p. 113525, Nov. 2019, doi: 10.1016/j.apenergy.2019.113525.

- [87] “Why modelling and model use matter: Journal of the Operational Research Society: Vol 61, No 1.” <https://www.tandfonline.com/doi/abs/10.1057/jors.2009.141?journalCode=tjor20> (accessed Nov. 16, 2022).
- [88] C. Green and S. Garimella, “Residential microgrid optimization using grey-box and black-box modeling methods,” *Energy and Buildings*, vol. 235, 2021, doi: 10.1016/J.ENBUILD.2020.110705.
- [89] B. Cui *et al.*, “A hybrid building thermal modeling approach for predicting temperatures in typical, detached, two-story houses,” *Applied Energy*, 2019, doi: 10.1016/J.APENERGY.2018.11.077.
- [90] M. Emami Javanmard and S. F. Ghaderi, “Energy demand forecasting in seven sectors by an optimization model based on machine learning algorithms,” *Sustainable Cities and Society*, vol. 95, p. 104623, Aug. 2023, doi: 10.1016/j.scs.2023.104623.
- [91] M. Emami Javanmard, Y. Tang, Z. Wang, and P. Tontiwachwuthikul, “Forecast energy demand, CO2 emissions and energy resource impacts for the transportation sector,” *Applied Energy*, vol. 338, p. 120830, May 2023, doi: 10.1016/j.apenergy.2023.120830.
- [92] Z. Wang, T. Hong, and M. A. Piette, “Building thermal load prediction through shallow machine learning and deep learning,” *Applied Energy*, vol. 263, p. 114683, Apr. 2020, doi: 10.1016/j.apenergy.2020.114683.
- [93] G. Ciulla and A. D’Amico, “Building energy performance forecasting: A multiple linear regression approach,” *Applied Energy*, vol. 253, p. 113500, Nov. 2019, doi: 10.1016/j.apenergy.2019.113500.
- [94] Z. Ma, J. Wang, F. Dong, R. Wang, H. Deng, and Y. Feng, “A decomposition-ensemble prediction method of building thermal load with enhanced electrical load information,” *Journal of Building Engineering*, vol. 61, p. 105330, Dec. 2022, doi: 10.1016/j.job.2022.105330.
- [95] R. Sarwar, H. Cho, S. J. Cox, P. J. Mago, and R. Luck, “Field validation study of a time and temperature indexed autoregressive with exogenous (ARX) model for building thermal load prediction,” *Energy*, vol. 119, pp. 483–496, Jan. 2017, doi: 10.1016/j.energy.2016.12.083.
- [96] A. Sandberg, F. Wallin, H. Li, and M. Azaza, “An Analyze of Long-term Hourly District Heat Demand Forecasting of a Commercial Building Using Neural Networks,” *Energy Procedia*, vol. 105, pp. 3784–3790, May 2017, doi: 10.1016/j.egypro.2017.03.884.
- [97] Y. Guo, E. Nazarian, J. Ko, and K. Rajurkar, “Hourly cooling load forecasting using time-indexed ARX models with two-stage weighted least squares regression,” *Energy Conversion and Management*, vol. 80, pp. 46–53, Apr. 2014, doi: 10.1016/j.enconman.2013.12.060.
- [98] K. M. Powell, A. Sriprasad, W. J. Cole, and T. F. Edgar, “Heating, cooling, and electrical load forecasting for a large-scale district energy system,” *Energy*, vol. 74, pp. 877–885, Sep. 2014, doi: 10.1016/j.energy.2014.07.064.
- [99] P. Lusi, K. R. Khalilpour, L. Andrew, and A. Liebman, “Short-term residential load forecasting: Impact of calendar effects and forecast granularity,” *Applied Energy*, vol. 205, pp. 654–669, Nov. 2017, doi: 10.1016/j.apenergy.2017.07.114.

- [100] D. Koschwitz, J. Frisch, and C. van Treeck, "Data-driven heating and cooling load predictions for non-residential buildings based on support vector machine regression and NARX Recurrent Neural Network: A comparative study on district scale," *Energy*, vol. 165, pp. 134–142, Dec. 2018, doi: 10.1016/j.energy.2018.09.068.
- [101] K. Liu, T. Liu, P. Fang, and J. Zhao, "Thermal Load Prediction by Various Hybrid Models Based on Different Artificial Intelligence Techniques," in *2016 8th International Conference on Intelligent Human-Machine Systems and Cybernetics (IHMSC)*, Aug. 2016, pp. 464–467. doi: 10.1109/IHMSC.2016.60.
- [102] H. Yan, K. Yan, and G. Ji, "Optimization and prediction in the early design stage of office buildings using genetic and XGBoost algorithms," *Building and Environment*, vol. 218, p. 109081, Jun. 2022, doi: 10.1016/j.buildenv.2022.109081.
- [103] Z. Wei *et al.*, "Prediction of residential district heating load based on machine learning: A case study," *Energy*, vol. 231, p. 120950, Sep. 2021, doi: 10.1016/j.energy.2021.120950.
- [104] P. Xue, Y. Jiang, Z. Zhou, X. Chen, X. Fang, and J. Liu, "Multi-step ahead forecasting of heat load in district heating systems using machine learning algorithms," *Energy*, vol. 188, p. 116085, Dec. 2019, doi: 10.1016/j.energy.2019.116085.
- [105] S. Seyedzadeh, F. Pour Rahimian, P. Rastogi, and I. Glesk, "Tuning machine learning models for prediction of building energy loads," *Sustainable Cities and Society*, vol. 47, p. 101484, May 2019, doi: 10.1016/j.scs.2019.101484.
- [106] K. ArunKumar, D. V. Kalaga, C. M. S. Kumar, M. Kawaji, and T. M. Brenza, "Forecasting of COVID-19 using deep layer recurrent neural networks (RNNs) with gated recurrent units (GRUs) and long short-term memory (LSTM) cells," *Chaos, Solitons & Fractals*, vol. 146, p. 110861, 2021.
- [107] W. Wang, T. Hong, X. Xu, J. Chen, Z. Liu, and N. Xu, "Forecasting district-scale energy dynamics through integrating building network and long short-term memory learning algorithm," *Applied Energy*, vol. 248, pp. 217–230, Aug. 2019, doi: 10.1016/j.apenergy.2019.04.085.
- [108] Y. Xu, F. Li, and A. Asgari, "Prediction and optimization of heating and cooling loads in a residential building based on multi-layer perceptron neural network and different optimization algorithms," *Energy*, vol. 240, p. 122692, 2022.
- [109] Z. Yan *et al.*, "A multi-energy load prediction of a building using the multi-layer perceptron neural network method with different optimization algorithms," *Energy Exploration & Exploitation*, vol. 41, no. 1, pp. 273–305, 2023.
- [110] G. Suryanarayana, J. Lago, D. Geysen, P. Aleksiejuk, and C. Johansson, "Thermal load forecasting in district heating networks using deep learning and advanced feature selection methods," *Energy*, vol. 157, pp. 141–149, Aug. 2018, doi: 10.1016/j.energy.2018.05.111.

- [111] J. Sun, G. Liu, B. Sun, and G. Xiao, "Light-stacking strengthened fusion based building energy consumption prediction framework via variable weight feature selection," *Applied Energy*, vol. 303, p. 117694, 2021.
- [112] C. Fan, F. Xiao, and Y. Zhao, "A short-term building cooling load prediction method using deep learning algorithms," *Applied energy*, vol. 195, pp. 222–233, 2017.
- [113] D.-S. Kapetanakis, E. Mangina, and D. P. Finn, "Input variable selection for thermal load predictive models of commercial buildings," *Energy and Buildings*, vol. 137, pp. 13–26, 2017.
- [114] Y. P. Raykov, E. Ozer, G. Dasika, A. Boukouvalas, and M. A. Little, "Predicting room occupancy with a single passive infrared (PIR) sensor through behavior extraction," in *Proceedings of the 2016 ACM International Joint Conference on Pervasive and Ubiquitous Computing*, in UbiComp '16. New York, NY, USA: Association for Computing Machinery, Sep. 2016, pp. 1016–1027. doi: 10.1145/2971648.2971746.
- [115] M. S. Zuraimi, A. Pantazaras, K. A. Chaturvedi, J. J. Yang, K. W. Tham, and S. E. Lee, "Predicting occupancy counts using physical and statistical Co₂-based modeling methodologies," *Building and Environment*, vol. 123, pp. 517–528, Oct. 2017, doi: 10.1016/j.buildenv.2017.07.027.
- [116] L. M. Candanedo and V. Feldheim, "Accurate occupancy detection of an office room from light, temperature, humidity and CO₂ measurements using statistical learning models," *Energy and Buildings*, vol. 112, pp. 28–39, Jan. 2016, doi: 10.1016/j.enbuild.2015.11.071.
- [117] I. B. Arief-Ang, M. Hamilton, and F. D. Salim, "A Scalable Room Occupancy Prediction with Transferable Time Series Decomposition of CO₂ Sensor Data," *ACM Trans. Sen. Netw.*, vol. 14, no. 3–4, p. 21:1-21:28, Nov. 2018, doi: 10.1145/3217214.
- [118] Paolo Bonato, Anton Soppelsa, Marta Avantaggiato, and Roberto Fedrizzi, "Assessment of Demand-Side Management on the Performance of a Single-Dwelling Mechanical Ventilation Plus Radiant Floor System," presented at the Building Simulation Applications BSA 2022, Bolzano, Italy: bu,press, 2022, pp. 281–288. doi: 10.13124/9788860461919.
- [119] H. Taud and J. F. Mas, "Multilayer Perceptron (MLP)," in *Geomatic Approaches for Modeling Land Change Scenarios*, M. T. Camacho Olmedo, M. Paegelow, J.-F. Mas, and F. Escobar, Eds., in Lecture Notes in Geoinformation and Cartography. Cham: Springer International Publishing, 2018, pp. 451–455. doi: 10.1007/978-3-319-60801-3_27.
- [120] S. S. Mousavi, M. Schukat, and E. Howley, "Deep Reinforcement Learning: An Overview," in *Proceedings of SAI Intelligent Systems Conference (IntelliSys) 2016*, Y. Bi, S. Kapoor, and R. Bhatia, Eds., in Lecture Notes in Networks and Systems. Cham: Springer International Publishing, 2018, pp. 426–440. doi: 10.1007/978-3-319-56991-8_32.
- [121] J. Brownlee, "Why Initialize a Neural Network with Random Weights?," *Machine Learning Mastery*, Aug. 13, 2022. <https://machinelearningmastery.com/why-initialize-a-neural-network-with-random-weights/> (accessed Oct. 05, 2022).

- [122] X. Glorot and Y. Bengio, “Understanding the difficulty of training deep feedforward neural networks,” in *Proceedings of the Thirteenth International Conference on Artificial Intelligence and Statistics*, JMLR Workshop and Conference Proceedings, Mar. 2010, pp. 249–256. Accessed: Feb. 16, 2023. [Online]. Available: <https://proceedings.mlr.press/v9/glorot10a.html>
- [123] K. He, X. Zhang, S. Ren, and J. Sun, “Delving Deep into Rectifiers: Surpassing Human-Level Performance on ImageNet Classification.” arXiv, Feb. 06, 2015. doi: 10.48550/arXiv.1502.01852.
- [124] X. Wen, M. Jaxa-Rozen, and E. Trutnevyte, “Accuracy indicators for evaluating retrospective performance of energy system models,” *Applied Energy*, vol. 325, p. 119906, 2022.
- [125] C. Jacovides and H. Kontoyiannis, “Statistical procedures for the evaluation of evapotranspiration computing models,” *Agricultural water management*, vol. 27, no. 3–4, pp. 365–371, 1995.
- [126] G. R. Ruiz and C. F. Bandera, “Validation of Calibrated Energy Models: Common Errors,” *Energies*, vol. 10, no. 10, Art. no. 10, Oct. 2017, doi: 10.3390/en10101587.
- [127] A. Sohani, M. H. Shahverdian, S. Hoseinzadeh, and M. E. H. Assad, “Thermal energy storage systems,” *Emerging trends in energy storage systems and industrial applications*, pp. 189–222, 2023.
- [128] I. Sarbu and I. Sarbu, “Thermal energy storage,” *Advances in Building Services Engineering: Studies, Researches and Applications*, pp. 559–627, 2021.
- [129] J. Brownlee, “Recommendations for Deep Learning Neural Network Practitioners,” *MachineLearningMastery.com*, Feb. 24, 2019. <https://machinelearningmastery.com/recommendations-for-deep-learning-neural-network-practitioners/> (accessed Aug. 25, 2023).
- [130] R. Aris, “Mathematical modeling : a chemical engineer’s perspective,” 1999, doi: 10.1016/s1874-5970(99)x8001-5.
- [131] “Overview Article - Integrating Heat Pumps in Existing Residential Buildings | BUILD UP.” <https://build-up.ec.europa.eu/en/resources-and-tools/articles/overview-article-integrating-heat-pumps-existing-residential-buildings> (accessed Sep. 06, 2023).
- [132] “Decarbonizing heat in the European buildings sector: options, progress and challenges - Issue 135,” *Oxford Institute for Energy Studies*. <https://www.oxfordenergy.org/publications/decarbonizing-heat-in-the-european-buildings-sector-options-progress-and-challenges-issue-135/> (accessed Sep. 06, 2023).
- [133] Y. V. Lun and S. D. Tung, *Heat pumps for sustainable heating and cooling*. Springer, 2019.
- [134] J. Seiffertt, “State Machine Theory and Optimization,” in *Digital Logic for Computing*, J. Seiffertt, Ed., Cham: Springer International Publishing, 2017, pp. 289–302. doi: 10.1007/978-3-319-56839-3_19.
- [135] “A two-state hysteresis model for bolted joints, with minor loops from partial unloading - ScienceDirect.”

- <https://www.sciencedirect.com/science/article/pii/S0020740317320775?via%3Dihub> (accessed Sep. 06, 2023).
- [136] G. Fiore, E. D. Santis, and M. D. Di Benedetto, “Predictability for Finite State Machines: a set-membership approach,” *IFAC-PapersOnLine*, vol. 51, no. 7, pp. 355–360, Jan. 2018, doi: 10.1016/j.ifacol.2018.06.325.
- [137] A. Mitrevski and P. G. Plöger, “Reusable Specification of State Machines for Rapid Robot Functionality Prototyping,” in *RoboCup 2019: Robot World Cup XXIII*, S. Chalup, T. Niemueller, J. Suthakorn, and M.-A. Williams, Eds., in Lecture Notes in Computer Science. Cham: Springer International Publishing, 2019, pp. 408–417. doi: 10.1007/978-3-030-35699-6_32.
- [138] D. Pršić and A. Vičovac, “Modelling of Control Logic for Start-Up and Shut-Down Sequences of the Heat Pump”.
- [139] J. Pakanen and S. Karjalainen, “A state machine approach in modelling the heating process of a building,” *Energy and Buildings*, vol. 41, no. 5, pp. 528–533, May 2009, doi: 10.1016/j.enbuild.2008.11.020.
- [140] “Practical Design and Application of Model Predictive Control - 1st Edition.” <https://shop.elsevier.com/books/practical-design-and-application-of-model-predictive-control/khaled/978-0-12-813918-9> (accessed Sep. 10, 2023).
- [141] M. Bujarbaruah, X. Zhang, M. Tanaskovic, and F. Borrelli, “Adaptive MPC under Time Varying Uncertainty: Robust and Stochastic.” arXiv, Apr. 11, 2021. doi: 10.48550/arXiv.1909.13473.
- [142] E. S. Meadows, “Dynamic programming and model predictive control,” presented at the Proceedings of the 1997 American Control Conference (Cat. No. 97CH36041), IEEE, 1997, pp. 1635–1639.
- [143] J. C. Salazar, P. Weber, F. Nejari, D. Theilliol, and R. Sarrate, “MPC Framework for System Reliability Optimization,” in *Advanced and Intelligent Computations in Diagnosis and Control*, Z. Kowalczyk, Ed., in Advances in Intelligent Systems and Computing. Cham: Springer International Publishing, 2016, pp. 161–177. doi: 10.1007/978-3-319-23180-8_12.
- [144] “Dynamic Programming | Princeton University Press.” <https://press.princeton.edu/books/paperback/9780691146683/dynamic-programming> (accessed Sep. 10, 2023).
- [145] P. Prabhu, S. R. Beard, S. Apostolakis, A. Zaks, and D. I. August, “MemoDyn: Exploiting Weakly consistent data structures for dynamic parallel memoization,” in *Proceedings - 27th International Conference on Parallel Architectures and Compilation Techniques, PACT 2018*, Institute of Electrical and Electronics Engineers Inc., Nov. 2018, p. a15. doi: 10.1145/3243176.3243193.
- [146] H. Qin, Z. Yu, T. Li, X. Liu, and L. Li, “Heating Control Strategy Based on Dynamic Programming for Building Energy Saving and Emission Reduction,” *International Journal of Environmental Research and Public Health*, vol. 19, no. 21, Art. no. 21, Jan. 2022, doi: 10.3390/ijerph192114137.

- [147] H. Pombeiro, M. J. Machado, and C. Silva, “Dynamic programming and genetic algorithms to control an HVAC system: Maximizing thermal comfort and minimizing cost with PV production and storage,” *Sustainable Cities and Society*, vol. 34, pp. 228–238, Oct. 2017, doi: 10.1016/j.scs.2017.05.021.
- [148] G. P. Henze, B. Biffar, D. Kohn, and M. P. Becker, “Optimal design and operation of a thermal storage system for a chilled water plant serving pharmaceutical buildings,” *Energy and Buildings*, vol. 40, no. 6, pp. 1004–1019, Jan. 2008, doi: 10.1016/j.enbuild.2007.08.006.

Appendix 1

The wide range for hysteresis HA, set as [-5, 5], allows the tank to be used for long charging and discharging cycles. For example, if the set point is 60°C, once the temperature at the top sensor drops below 55°C, the HP will be activated to charge the tank until the bottom sensor reaches 65°C. This process is illustrated in Figure 3-50.

Upon implementing MPC, it was observed that the extended charge cycle length significantly hindered the MPC's ability to capitalize on available incentives. This limitation is due to the strict loyalty required to the hysteresis settings, which prevents the HP from being turned ON or OFF in response to incentive opportunities. As a result, the potential for optimizing HP operation is limited.

A shallower hysteresis range, such as [0, 5], could offer increased flexibility for the MPC, allowing it to better adjust the HP operation in response to incentives. By narrowing the hysteresis range, the system could react more dynamically to changes in energy prices or availability of DH temperature, thereby enhancing overall efficiency and cost-effectiveness.

Appendix 2

This appendix provides a detailed enumeration of all possible cases arising from the combination of five different hysteresis mechanisms. Each case represents a unique state of the substation, determined by the activation (1) or deactivation (0) of each mechanism. The mechanisms considered are HA, HMa, HMb, HMc, and HMd. Notably, when HA is 0, the HP is ON, and when HA is 1, the HP is OFF. Table 0-1 summarizes all 32 combinations of hysteresis mechanisms, providing a comprehensive overview of the conditions under which each mechanism is active or inactive.

Table 0-1: Comprehensive list of hysteresis mechanism cases for schemes' transition

Case	Hysteresis combinations	Scheme
1	HA * HMa * HMb * HMc * HMd	HP OFF
2	HA * HMa * HMb * HMc * NOT(HMd)	HP OFF
3	HA * HMa * HMb * NOT(HMc) * HMd	HP OFF
4	HA * HMa * HMb * NOT(HMc) * NOT(HMd)	HP OFF
5	HA * HMa * NOT(HMb) * HMc * HMd	HP OFF
6	HA * HMa * NOT(HMb) * HMc * NOT(HMd)	HP OFF
7	HA * HMa * NOT(HMb) * NOT(HMc) * HMd	HP OFF
8	HA * HMa * NOT(HMb) * NOT(HMc) * NOT(HMd)	HP OFF
9	HA * NOT(HMa) * HMb * HMc * HMd	HP OFF
10	HA * NOT(HMa) * HMb * HMc * NOT(HMd)	HP OFF
11	HA * NOT(HMa) * HMb * NOT(HMc) * HMd	HP OFF
12	HA * NOT(HMa) * HMb * NOT(HMc) * NOT(HMd)	HP OFF
13	HA * NOT(HMa) * NOT(HMb) * HMc * HMd	HP OFF
14	HA * NOT(HMa) * NOT(HMb) * HMc * NOT(HMd)	HP OFF
15	HA * NOT(HMa) * NOT(HMb) * NOT(HMc) * HMd	HP OFF
16	HA * NOT(HMa) * NOT(HMb) * NOT(HMc) * NOT(HMd)	HP OFF
17	NOT(HA) * HMa * HMb * HMc * HMd	Scheme 4
18	NOT(HA) * HMa * HMb * HMc * NOT(HMd)	Scheme 4
19	NOT(HA) * HMa * HMb * NOT(HMc) * HMd	Scheme 4
20	NOT(HA) * HMa * HMb * NOT(HMc) * NOT(HMd)	Scheme 4
21	NOT(HA) * HMa * NOT(HMb) * HMc * HMd	Scheme 4
22	NOT(HA) * HMa * NOT(HMb) * HMc * NOT(HMd)	Scheme 4
23	NOT(HA) * HMa * NOT(HMb) * NOT(HMc) * HMd	Scheme 4
24	NOT(HA) * HMa * NOT(HMb) * NOT(HMc) * NOT(HMd)	Scheme 4
25	NOT(HA) * NOT(HMa) * HMb * HMc * HMd	Special case 1
26	NOT(HA) * NOT(HMa) * HMb * HMc * NOT(HMd)	Special case 2
27	NOT(HA) * NOT(HMa) * HMb * NOT(HMc) * HMd	Scheme 1
28	NOT(HA) * NOT(HMa) * HMb * NOT(HMc) * NOT(HMd)	Scheme 1

29	NOT(HA) * NOT(HMa) * NOT(HMb) * HMc * HMd	Special case 3
30	NOT(HA) * NOT(HMa) * NOT(HMb) * HMc * NOT(HMd)	Scheme 3
31	NOT(HA) * NOT(HMa) * NOT(HMb) * NOT(HMc) * HMd	Scheme 2
32	NOT(HA) * NOT(HMa) * NOT(HMb) * NOT(HMc) * NOT(HMd)	Scheme 2

Special case 1: NOT(HA) * NOT(HMa) * HMb * HMc * HMd

In this scenario, $T_{ret, TES} > T_{DH} > T_{in, Max, HP}$. Due to the evaporator's maximum inlet temperature limitation, transitioning to schemes 1, 2, or 3 is not feasible. Thus, even though T_{DH} is below $T_{set, direct, DH}$, the safest course of action is to proceed with scheme 4.

Special case 2: NOT(HA) * NOT(HMa) * HMb * HMc * NOT(HMd)

This scenario presents a mathematical impossibility due to conflicting temperature conditions. In this case, $T_{ret, TES} > T_{DH}$, $T_{DH} > T_{in, Max, HP}$ and $T_{in, Max, HP} > T_{ret, TES}$. These conditions cannot coexist because they create a logical contradiction. this case is deemed impossible to occur in practice.

Special case 3: NOT(HA) * NOT(HMa) * NOT(HMb) * HMc * HMd

This scenario presents a mathematical impossibility due to conflicting temperature conditions. In this case, $T_{DH} > T_{ret, TES}$, $T_{DH} > T_{in, Max, HP}$ and $T_{ret, TES} > T_{in, Max, HP}$. These conditions cannot coexist because they create a logical contradiction. this case is deemed impossible to occur in practice.